Check for updates

Asymmetrically tailored catalysts towards electrochemical energy conversion with non-precious materials

Lei Zhang, [ID] [a] Qiaoling Xu,[a] Lu Xia, [ID] [c] Wulyu Jiang, [ID] [c] Kaiwen Wang,[c] Pengfei Cao,[d] Qiang Chen,[e] Ming Huang, [ID] [f] F. Pelayo García de Arquer [ID] *[c] and Yingtang Zhou [ID] *[b]

Electrocatalytic technologies, such as water electrolysis and metal–air batteries, enable a path to sustainable energy storage and conversion into high-value chemicals. These systems rely on electrocatalysts to drive redox reactions that define key performance metrics such as activity and selectivity. However, conventional electrocatalysts face inherent trade-offs between activity, stability, and scalability particularly due to the reliance on noble metals. Asymmetrically tailored electrocatalysts (ATEs) – systems that are being exploited for non-symmetric designs in composition, size, shape, and coordination environments – offer a path to overcome these barriers. Here, we summarize recent developments in ATEs, focusing on asymmetric coupling strategies employed in designing these systems with non-precious transition metal catalysts (TMCs). We explore tailored asymmetries in composition, size, and coordination environments, highlighting their impact on catalytic performance. We analyze the electrocatalytic mechanisms underlying ATEs with an emphasis on their roles in water-splitting and metal–air batteries. Finally, we discuss the challenges and opportunities in advancing the performance of these technologies through rational ATE designs.

1. Introduction

The demand for renewable energy accelerates the need to develop cost-effective and environmentally friendly energy conversion and storage technologies.[1–3] Some strategies to this end involve batteries, fuel cells, and water electrolyzers.[4–6] This work focuses on water electrolysis and rechargeable metal–air batteries, highlighting how advances in catalyst design could overcome existing technology bottlenecks.

Both water electrolysis and rechargeable metal–air batteries face limitations related to their three critical supporting reactions: the hydrogen evolution reaction (HER), the oxygen evolution

reaction (OER), and the oxygen reduction reaction (ORR) (Fig. 1).[7–9] The HER and the OER are crucial in water electrolysis and extended electrosynthesis systems,[10] which may combine alternative anodic oxidation reactions (*e.g.*, alcohol and biomass valorization), or direct cathodic conversion reactions such as CO_2 and N_2 reduction.[11–13]

The OER and the ORR are the primary polarization processes in rechargeable metal–air batteries, fuel cells, and electrochemical carbon capture technologies based on electrocatalysis.[14–18] These half reactions involve multi-electron transfer processes and exhibit sluggish kinetics.[19–21] Therefore, designing electrocatalysts to speed up and improve energy conversion efficiency in these processes is important.[22–25]

Noble metal catalysts are widely used to support these reactions due to their activity and stability. However, their high cost and scarcity pose barriers to large-scale deployment.[26–30] In contrast, non-precious TMCs offer a promising alternative, as they can be structurally modified through techniques such as size control, heteroatom introduction, defect engineering, and substrate effects.[31–36] These modifications enhance the conductivity and electronic states of TMCs, improving their catalytic performance and positioning them as potential alternatives for noble metal materials.[37–39]

Asymmetricity is a common feature in natural systems, offering functional advantages.[40,41] For instance, asymmetrical

[a] *School of Materials Science and Engineering, Anhui Province Key Laboratory of Specialty Polymers, Anhui University of Science and Technology, Huaian, Anhui 232001, P. R. China*

[b] *Zhejiang Key Laboratory of Petrochemical Environmental Pollution Control, Marine Science and Technology College, Zhejiang Ocean University, Zhoushan, Zhejiang Province 316004, P. R. China. E-mail: zhouyingtang@zjou.edu.cn*

[c] *ICFO-Institut de Ciències Fotòniques, The Barcelona Institute of Science and Technology, Castelldefels (Barcelona), 08860, Spain. E-mail: pelayo.garciadearquer@icfo.eu*

[d] *Forschungszentrum Jülich GmbH, ER-C, 52425 Jülich, Germany*

[e] *Institute of Functional Nano & Soft Materials (FUNSOM), Soochow University, Suzhou 215123, P. R. China*

[f] *Institute of Fundamental and Frontier Sciences, University of Electronic Science and Technology of China, Chengdu 611731, P. R. China*

5108 | *Chem. Soc. Rev.*, 2025, **54**, 5108–5145

This journal is © The Royal Society of Chemistry 2025

leaf arrangements in plants optimize sunlight absorption, while the asymmetric shells of mollusks enhance self-protection and buoyancy regulation. Inspired by these principles, introducing asymmetry into material structures presents an attractive approach to improving catalytic activity.[42] Achieving this requires precise control over component selection, size, coordination environments, and the design of catalyst assembly units.[43]

Several works have provided evidence regarding the potential of asymmetric coupling designs in electrocatalysts.[44,45] Examples include the use of single-atom (SA) electrocatalysts featuring asymmetric coordination,[46] the use of metal–nitrogen–carbon (M–N–C) supported SAs with asymmetric coordination,[47] and the use of axially coordinated SAs.[48] These works have focused on particular aspects of individual asymmetric coupling strategies. The present work bridges the gaps between these individual views, providing an in-depth overview of the entire field of asymmetric coupling engineering.[49–51]

First, we present an overview of the broader development of asymmetric catalyst design strategies, categorizing them into compositional, size, coordination, and multiple asymmetric coupling approaches (Fig. 2). Next, we discuss their impact on physicochemical properties and electronic structure, focusing on how these factors regulate the adsorption–desorption processes of intermediates and enhance catalytic performance. Finally, we identify key challenges and outline perspectives for advancing ATEs toward improved functionality and scalability.

2. Development of asymmetric coupling design strategies

Asymmetric coupling strategies provide versatile approaches to enhancing electrocatalyst performance.[52–55] Compositional-asymmetric engineering involves integrating heterostructures with distinct components to modulate the resulting electronic structure.[56] This, in turn, facilitates introducing novel functionalities and optimizing catalytic intermediates, thereby boosting their catalytic performance. One important advance in recent years is the introduction of asymmetry in SA catalysts, which are characterized by a planar symmetry metal (M)–nitrogen (N_4) sites where the metal center is tetra-coordinated with nitrogen atoms.[57] Breaking the coordination symmetry of M-N_4 sites disrupts their charge distribution, offering an efficient method to boost catalytic activity.[58,59]

In catalytic systems featuring size asymmetry, integrating clusters (particles) to regulate the electronic structure of SAs/

Lei Zhang received his PhD from Nanjing University in 2011. From 2016 to 2017, he conducted postdoctoral research at Tsinghua University. He is currently a full professor at the School of Materials Science and Engineering, Anhui University of Science and Technology, P. R. China. His research interests focus on the design and preparation of functional micro- and nanomaterials for novel energy conversion and storage applications.

Lei Zhang

Qiaoling Xu received her BS degree from Anhui University of Science and Technology, China, in 2019. Since 2022, she has been pursuing her doctoral studies under the supervision of Prof. Zhang at the School of Materials Science and Engineering, Anhui University of Science and Technology. Her current research focuses on the design, synthesis, and performance optimization of highly efficient electrocatalytic materials.

Qiaoling Xu

F. Pelayo García de Arquer has been a Professor and group leader at ICFO since 2021. His research spans the design and implementation of materials for energy and optoelectronic applications, including the development of decarbonizing technologies such as CO_2 capture and solar fuels.

F. Pelayo García de Arquer

Yingtang Zhou is a senior professor in Zhejiang Ocean University, China. He obtained his PhD Degree in Biology Engineering from KU. Leuven in 2008. Currently he has interests in theoretical study, computational design and experimental synthesis of novel light-thermal materials as catalysts for light irradiation thermal treatment, renewable clean energy and environmental protection applications.
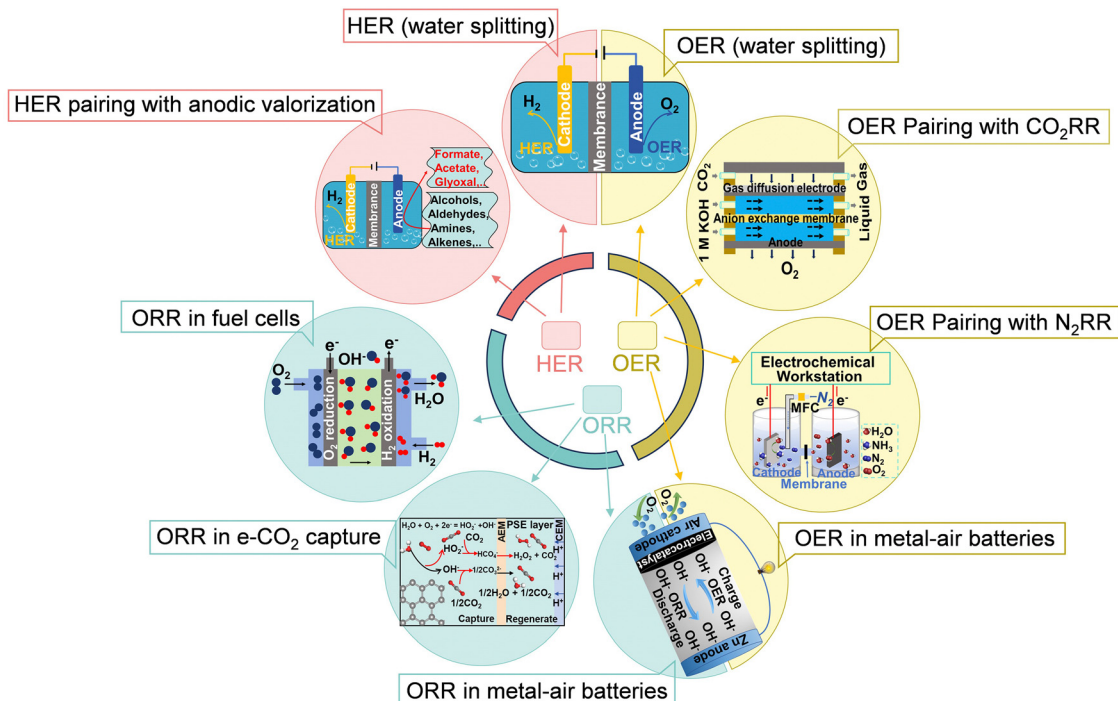
Yingtang Zhou

Fig. 1 Overview of HER, OER, and ORR applications in electrochemical energy systems. The illustration highlights critical reaction pairings, like anodic oxidation paired with the HER and cathodic CO_2 and N_2 reduction with the OER, showcasing their importance in diverse applications. These processes usually rely on noble metals to achieve high performance, posing a major challenge for their large-scale deployment due to high cost and resource scarcity.

clusters presents a promising strategy to optimize electrochemical performance.[60] This approach utilizes inherent disparities in electronic states among SAs, clusters, and nanoparticles, resulting in multiscale nano-hybrids with size-asymmetric coupling.[61] Another example involves material systems with coexisting forms of asymmetric couplings,[62] such as size asymmetry combined with coordination asymmetry, size asymmetry coupled with composition asymmetry, or a tripartite integration of size asymmetry, coordination asymmetry, and composition asymmetry. These synergistic interactions between multiple asymmetry mechanisms enhance catalytic performance.[63,64] Fig. 3 overviews the evolution and recent advancements in ATEs, highlighting key milestones and offering a roadmap for future research and innovation.

3. Regulation strategies of asymmetric coupling

3.1 Compositional-asymmetric coupling

Materials are typically classified into conductors, semiconductors, and insulators based on electrical conductivity.[77,78] When different materials are coupled, they form diverse heterogeneous interfaces with unique physicochemical properties arising from variations in electronic structures, band gaps, and other inherent characteristics among constituent units.[79–83] These interfaces enable precise control over atomic configurations, allowing catalytic reaction pathways to be fine-tuned, thereby enhancing efficiency and selectivity.[84–86] Here, we categorize heterointerfaces

into three main types: metal–metal heterojunctions, metal–semiconductor heterojunctions, and semiconductor–semiconductor heterojunctions. Building on the assembly strategies discussed earlier, we have organized and summarized recent advances and their key performance metrics in these heterojunctions (Fig. 4).

The structural advantages of compositional-asymmetric coupling electrocatalysts can be summarized as follows. (i) Tailored material properties: the integration of diverse materials enables precise modulation of properties such as conductivity, hydrophilicity, chemical stability, and active site density, collectively enhancing catalytic performance; (ii) lattice strain engineering: distinct chemical compositions and crystal structures induce lattice strain, which modifies the intermediate adsorption energies at active sites, leading to improved catalytic selectivity; (iii) enhanced charge transfer: variations in band alignments across different phases facilitate efficient charge transfer at interfaces, enabling precise modulation of surface electronic states within heterogeneous structures; and (iv) material versatility: the broad range of material types provides extensive opportunities for optimizing and assembling catalytic building units, fostering the design of advanced ATEs, and enriching the "gene library" of electrocatalysts.

3.1.1 The coupling of a metal and a metal. Metal–metal asymmetric coupling involves the integration of two or more chemically distinct metal elements within a shared nanoscale or atomic-scale framework. This deliberate symmetry breaking contrasts with homonuclear systems, where identical metal atoms define the active site. By introducing asymmetry in valence states, coordination environments, and spatial configurations,

5110 | Chem. Soc. Rev., 2025, 54, 5108–5145

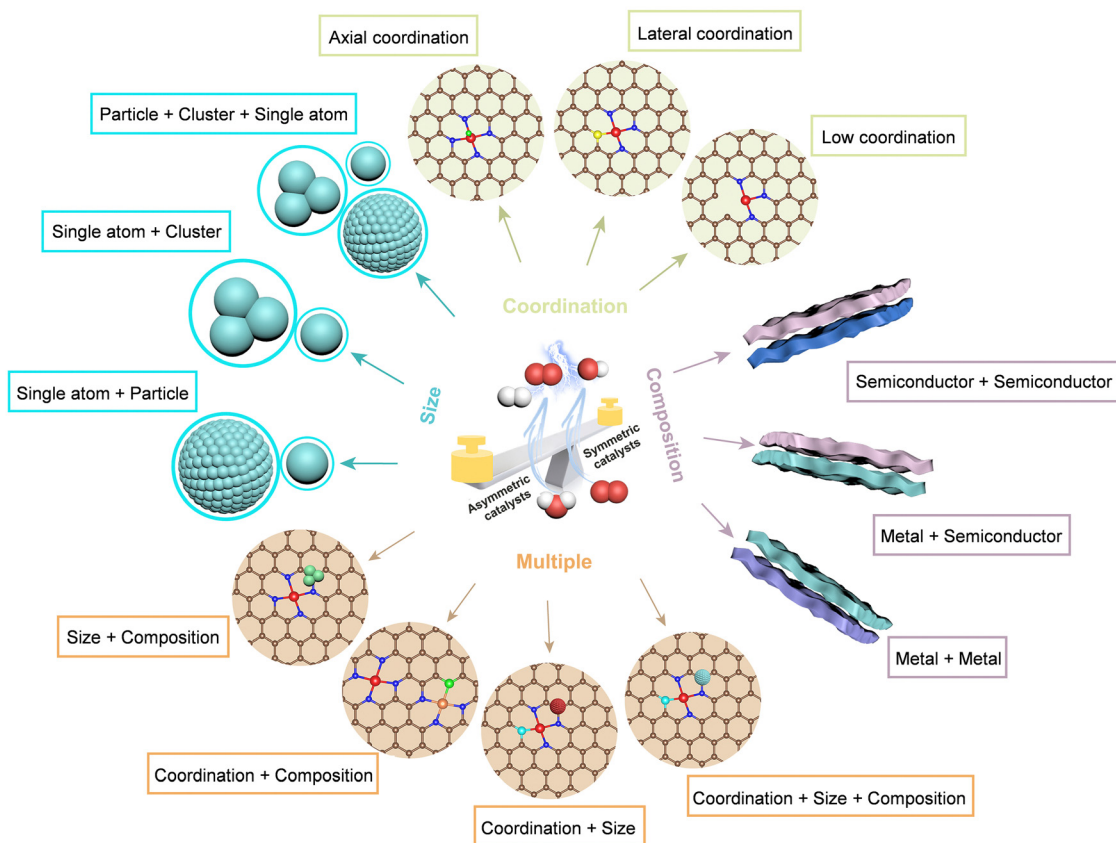This journal is © The Royal Society of Chemistry 2025

Fig. 2 Asymmetric coupling design strategies for non-precious TMCs. Illustration of asymmetric coupling design strategies for non-precious TMCs: size-asymmetric coupling among SAs, clusters, and particles, coordination-asymmetric coupling highlighting low-, lateral-, and axial-coordination, compositional-asymmetric coupling achieved through heterojunction design, and multiple asymmetric couplings combining these.

metal–metal asymmetric coupling disrupts conventional bonding symmetry, leading to emergent catalytic properties that are inaccessible in single-metal systems.

A compelling realization of this concept is heteronuclear dual-metal atom catalysts (DMACs), where two different metal atoms form a dimer structure on a support material.[62,104] Homonuclear DMACs do not merely amplify intrinsic activity through ensemble effects but also disrupt the local environment, leading to distinct electronic structures. Asymmetric DMACs may induce localized atomic orbital distortions, which impact π-orbital interactions and back-donation effects.[105] This can disrupt traditional linear scaling relationships, which often impose fundamental activity–stability trade-offs in homogeneous catalytic systems.[106] DMACs may impact selectivity and kinetics in multielectron transfer reactions, beyond SACs,[107] making these sites effective in activating small molecules like N_2, CO_2, and H_2O.[108]

For instance, atomically dispersed Cu and Co bimetallic sites anchored on a porous nitrogen-doped carbon (NC) framework exhibit exceptional bifunctional oxygen catalytic activity due to their optimal geometry and electronic structure (Fig. 5a and b).[87] Both experimental and theoretical findings indicated that the synergistic effects between the metal–N_4 coordination structures of Cu–Co bimetallic centers induced a charge asymmetry distribution, contributing to moderate the adsorption–

desorption ability of the catalytic centers with oxygen intermediates. Under alkaline conditions, the electrocatalyst yielded remarkable ORR/OER catalytic activities, with an ORR half-wave potential of 0.920 V and an overpotential of just 0.335 V at 10 mA cm^{-2} (Fig. 5c and d). It also delivered outstanding ORR activities under acidic (0.850 V) and neutral (0.740 V) conditions. When applied in Zn–air batteries, this catalyst yielded excellent performance and durability, with a longevity of 510 hours and 1000 cycles. Following this, a "pre-constrained metal twins" approach was introduced, effectively incorporating Fe and Co into the NC skeleton.[88] This approach led to the construction of a bifunctional catalyst with high-quality Fe–Co heteronuclear pairs, facilitating efficient oxygen electrocatalysis (Fig. 5e and f). Specifically, the Fe- and Co-containing binuclear phthalocyanine was initially introduced into the ZIF-8 matrix. Subsequently, through high-temperature carbonization, Zn species in ZIF-8 were volatilized, and ligands were transformed into NC materials. The adjacent Fe and Co atoms form proximal active sites known as Fe–N_4 and Co–N_4 complexes within this material. Electrochemical investigations demonstrated the exceptional catalytic performance of these heteronuclear pairs in both the OER/ORR. Theoretical simulations indicated that the collaborative effects of neighboring Fe and Co metals optimized the d-band center of metallic sites, equilibrating the free energy of *O species and consequently boosting the electrocatalytic performance towards oxygen.

This journal is © The Royal Society of Chemistry 2025
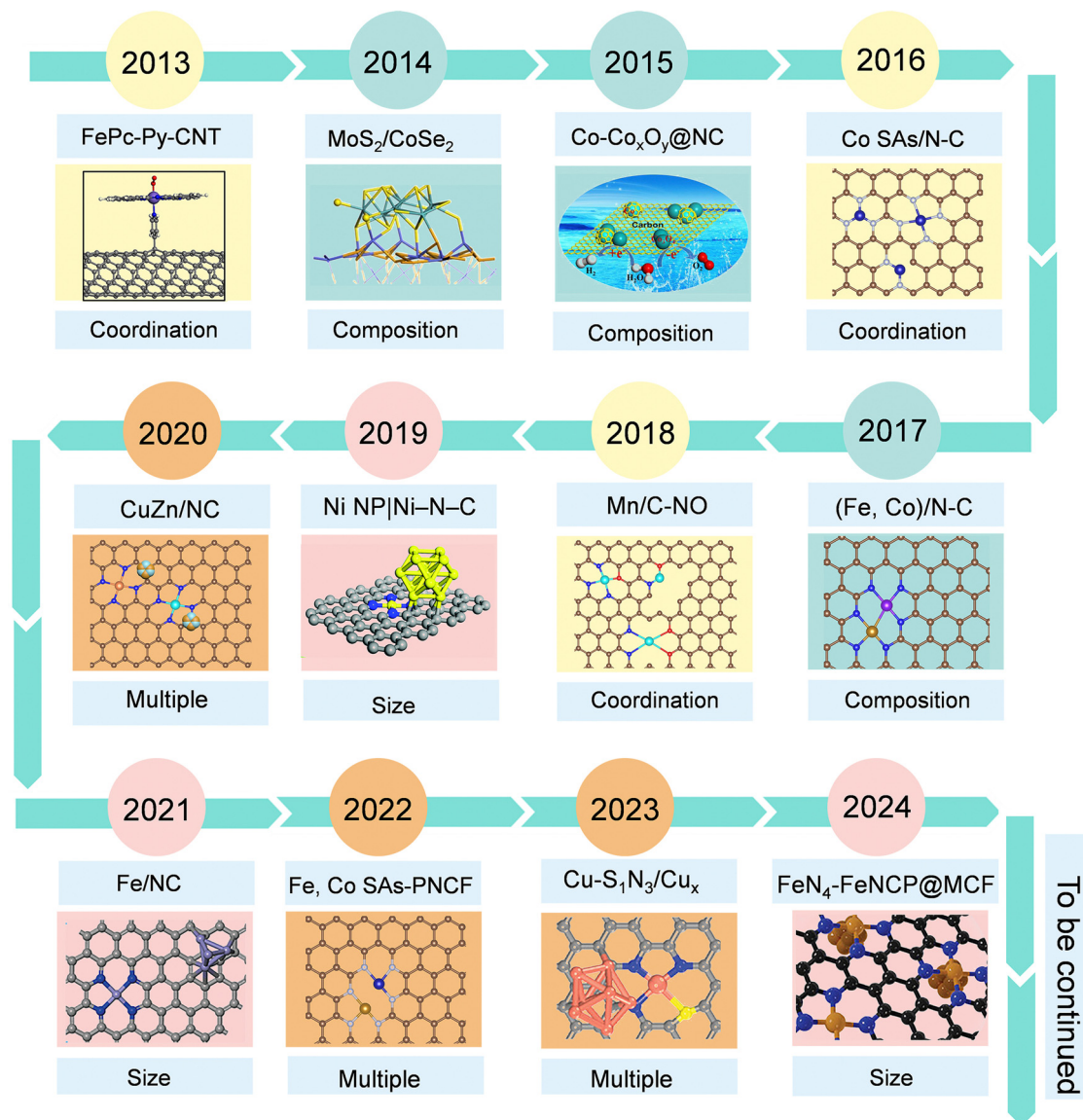
Chem. Soc. Rev., 2025, 54, 5108–5145 | 5111

Fig. 3 Timeline of evolution and breakthroughs in asymmetric coupling strategies for electrocatalysts. An overview of key milestones from 2013 to 2024 in the development of asymmetric coupling strategies, including coordination, composition, size, and multiple asymmetric designs. Examples showcase advancements such as FePc-Py-CNT (2013), MoS$_2$/CoSe$_2$ (2014), Co-Co$_3$O$_4$@NC (2015), Co SAs/N-C (2016), and Cu-S$_1$N$_3$/Cu$_x$ (2023). Each entry highlights pivotal innovations driving the progression of asymmetric tailored electrocatalysts (ATEs), offering insights into the field's evolution and future directions. Copyright 2013,[65] 2014.[66] Reproduced with permission. Copyright 2013 and 2014, Springer Nature. 2015,[67] 2017.[68] Reproduced with permission. Copyright 2015 and 2017, American Chemical Society. 2016,[69] 2018,[70] 2020,[71] 2021,[72] 2023,[73] 2024.[74] Reproduced with permission. Copyright 2016, 2018, 2020, 2021, 2023 and 2024, John Wiley and Sons. 2019.[75] Reproduced with permission. Copyright 2019, Royal Society of Chemistry. 2022.[76] Reproduced with permission. Copyright 2022, Elsevier.

As for water-splitting, compositional asymmetry through the coupling of different metals offers substantial advantages. For instance, a pioneering multistep templating method involving atomic migration and capture processes was developed, leveraging atomic migration and capture processes to synthesize atomically dispersed Ni and Co sites confined within a nitrogen-doped carbon (NC) hollow prism (Fig. 5g–i).[89] Theoretical calculations substantiated the enhanced electrocatalytic activity resulting from the synergistic catalytic effects between dual-nuclear sites (Fig. 5j). Through a similar synthesis approach, nanoscale asymmetric ATEs can also be constructed. For example, a spatial

segregation strategy was employed to produce an N/S doped carbon nanobox hosting Fe–Co pair-sites with compositional asymmetric coupling.[43] This unique nanostructure displayed outstanding electrocatalytic characteristics, delivering a half-wave potential of 0.903 V for the ORR and an overpotential of 0.296 V at 10 mA cm^{-2} for the OER. In summary, metal–metal asymmetric coupling leverages the electronic and geometric disparity between distinct metal centers to modulate adsorption energies and intermediate stabilization beyond conventional SACs.

3.1.2 The coupling of a metal and a semiconductor. The coupling of metals and semiconductors with distinct work

5112 | Chem. Soc. Rev., 2025, 54, 5108–5145
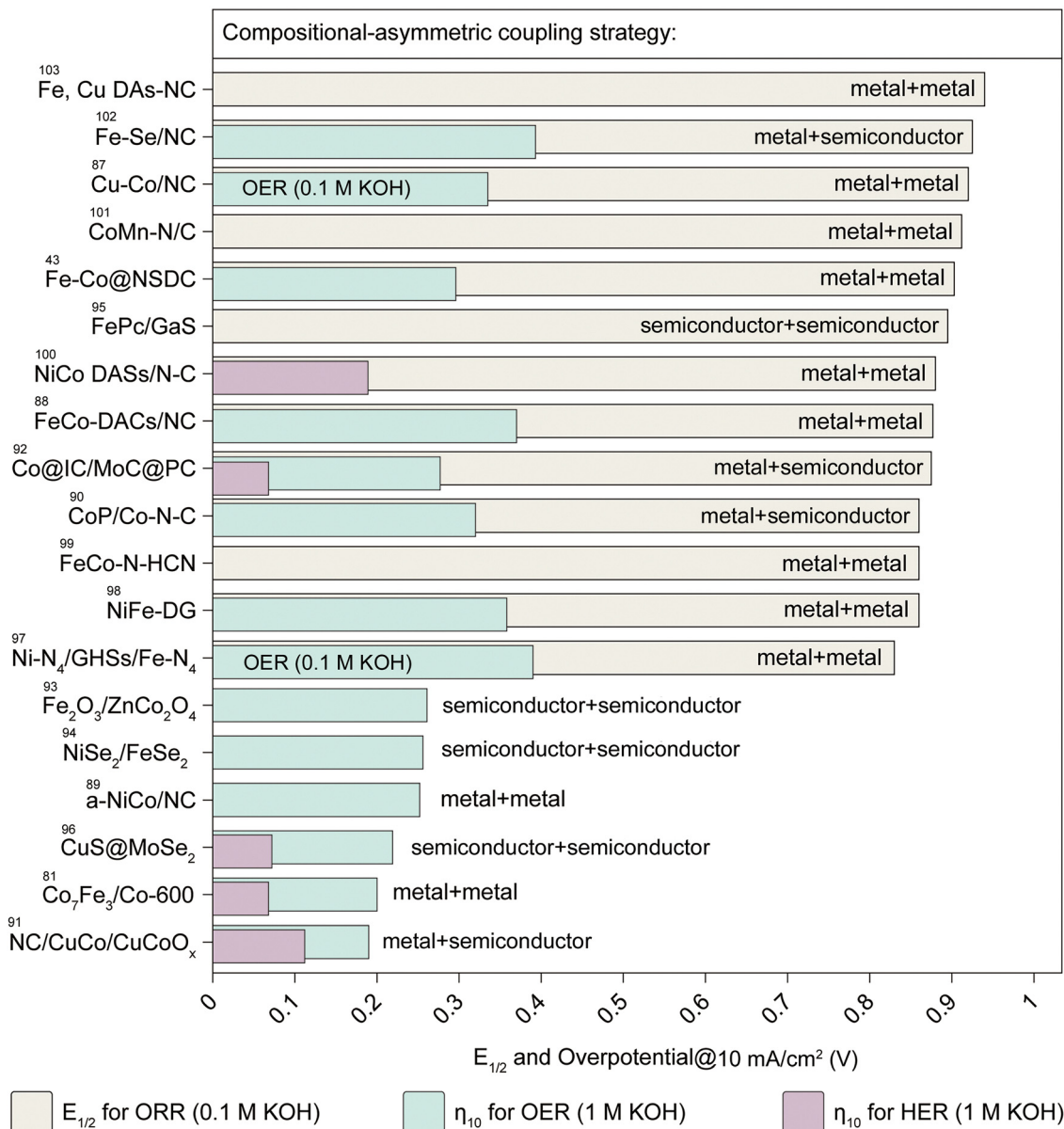
This journal is © The Royal Society of Chemistry 2025

Fig. 4 Summary of the performances for the designed catalysts based on the compositional-asymmetric coupling strategy. The plot categorizes catalysts into metal–metal, metal–semiconductor, and semiconductor–semiconductor heterojunctions, highlighting their respective catalytic performance indicators for the ORR, OER, and HER under alkaline conditions (0.1 M KOH or 1 M KOH). The figure emphasizes the half-wave potential ($E_{1/2}$) for the ORR and overpotential at 10 mA cm^{-2} (η_{10}) for the OER and HER as key benchmarks. This diagram provides a summary of the performance metrics reported in ref. 43, 81 and 87–103.

functions (WFs) enables electron transfer across their interface, inducing band bending and creating unique interfacial properties.[109,110] These heterojunctions possess unique mechanical, physical, and chemical properties compared to single-component materials attributed to electronic interactions, crystal defects, and lattice strain at the interface.[111,112] The electron density near the Fermi level of the interface plays a positive role in regulating electrical conductivity.[113] By systematically tuning the electronic and structural properties of such heterojunctions, researchers can unlock their potential to dramatically enhance electrochemical performance in energy conversion and storage applications.[114]

For example, a Mott–Schottky heterojunction composed of a porous cobalt–nitrogen–carbon (Co–N–C) polyhedron and abundant CoP nanoparticles was successfully designed (Fig. 6a and b).[90] For the ORR, the half-wave potential of CoP/Co–N–C was 0.860 V, along with an overpotential of 0.320 V at 10 mA cm^{-2} for the OER. Density functional theory (DFT) calculations indicated that the Mott–Schottky heterojunction formed an intrinsic electric field to facilitate interface charge transfer. This led to the movement of the d-band, thereby regulating the adsorption/desorption behavior of oxygen intermediates and achieving enhanced dual functionality for reversible oxygen electrocatalysis. Another metal–semiconductor
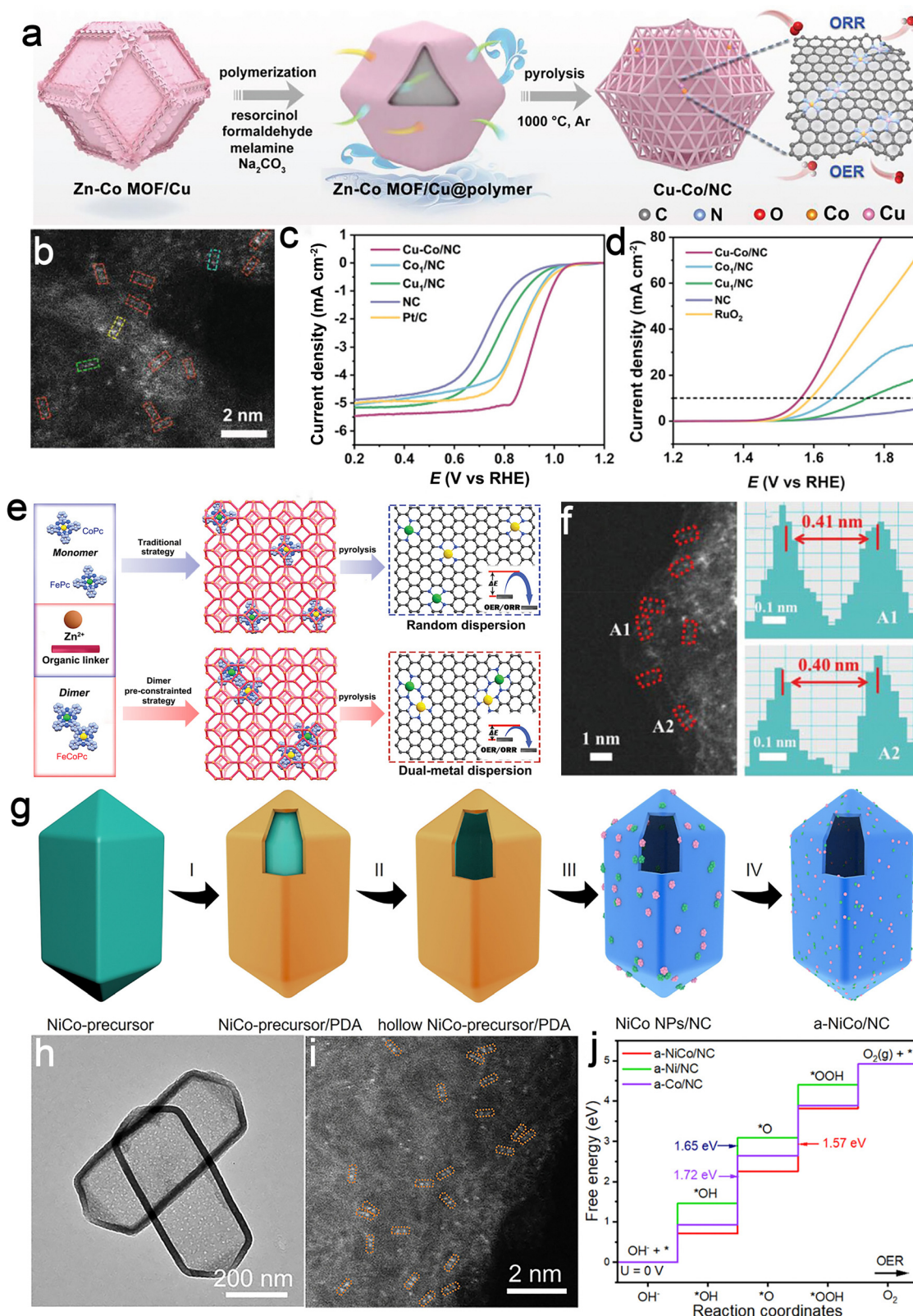
This journal is © The Royal Society of Chemistry 2025

Chem. Soc. Rev., 2025, **54**, 5108–5145 | **5113**

Fig. 5 Examples of metal–metal coupled catalysts. Cu-Co@NC catalyst: (a) synthetic scheme; (b) high-angle annular dark field scanning transmission electron microscopy (HAADF-STEM) image showcasing atomic dispersion; and (c) ORR and (d) OER polarization curves. Reproduced with permission from ref. 87. Copyright 2023, John Wiley and Sons. Fe–Co heteronuclear pairs catalyst: (e) schematic illustration comparing the traditional strategy and "pre-constrained metal twins" strategy; (f) HAADF-STEM image and intensity profiles for metal pairs. Reproduced with permission from ref. 88. Copyright 2022, John Wiley and Sons. Ni–Co dual sites catalyst: (g) Schematic illustration of the synthesis route; (h) transmission electron microscopy (TEM) image illustrating structural features and (i) HAADF-STEM image indicating dual-site dispersion; (j) free energy diagram of OER. Reproduced with permission from ref. 89. Copyright 2022, John Wiley and Sons.
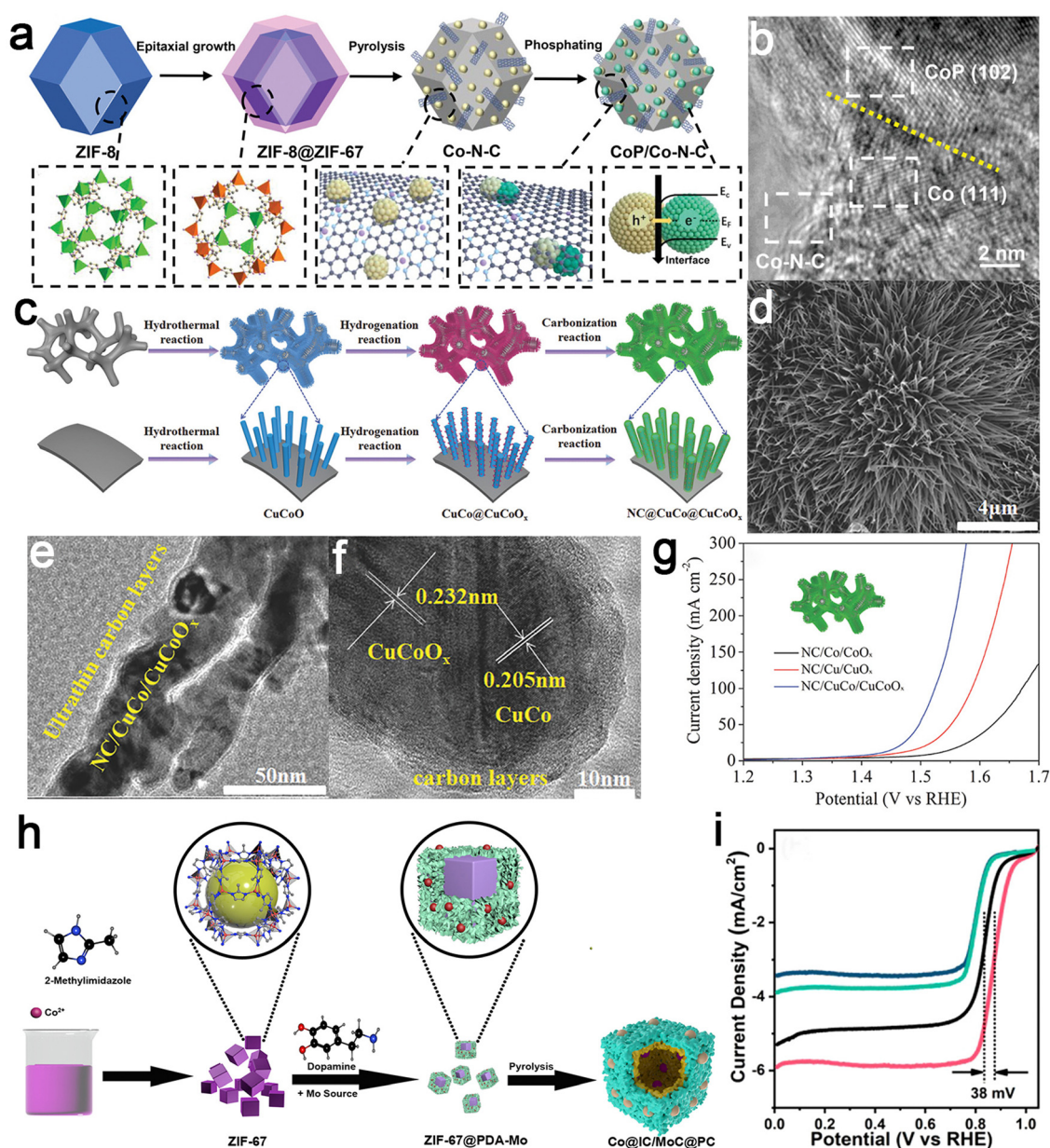
5114 | *Chem. Soc. Rev.*, 2025, **54**, 5108–5145

This journal is © The Royal Society of Chemistry 2025

Fig. 6 Examples of metal–semiconductor coupled catalysts. CoP/Co–N–C catalyst: (a) schematic illustration of the synthesis process and (b) high-resolution TEM (HRTEM) images of the sample highlighting lattice fringes of CoP and Co. Reproduced with permission from ref. 90. Copyright 2023, John Wiley and Sons. NC/CuCo/CuCoO$_x$ catalyst: (c) schematic illustration of the fabrication procedure; (d) scanning electron microscopy (SEM) and (e and f) TEM images showing the structural details; (g) OER polarization curves. Reproduced with permission from ref. 91. Copyright 2018, John Wiley and Sons. Co@IC/MoC@PC catalyst: and (h) design idea and preparation path, as well as (i) linear sweep voltammetry (LSV) plots. Reproduced with permission from ref. 92. Copyright 2021, American Chemical Society.

Mott–Schottky hybrid, featuring CuCo nanoalloys on arrays of defective CuCoO$_x$ semiconductor nanowires, was also recently fabricated.[91] To establish an uninterrupted electron transport route between a metal and a semiconductor, an NC matrix has been incorporated into the nanowire array of the metal–semiconductor, forming an integrated core–shell architecture (Fig. 6c–f). This innovative NC/CuCo/CuCoO$_x$ core–shell array demonstrated exceptional electrocatalytic OER–HER performances in a 1 M KOH medium (Fig. 6g). It achieved a noteworthy oxygen evolution current density of 10 mA cm^{-2} with a

mere 0.190 V overpotential and a hydrogen evolution current density of 10 mA cm^{-2} with a 0.112 V overpotential. When employed as both an anode and cathode for the overall water splitting, the core–shell composite array electrodes exhibited a remarkable current density of 10 mA cm^{-2} at an impressively low voltage of only 1.53 V, demonstrating their exceptional electrochemical performance. These electrodes demonstrated excellent stability during continuous operation for 100 hours under high current density conditions. Experimental findings indicated that the three-dimensional hierarchical structure

provided an extensive electrochemical active surface area, abundant active sites, and rapid gas transport. The *in situ* formation of metal–semiconductor Mott–Schottky catalysts generated rich oxygen vacancies, enhancing conductivity and promoting electron transfer. The NC skeleton promoted the adsorption of intermediates and constructed optimized pathways for electron transfer between the semiconductor, metal, and carbon layers by redistributing electron density. Recently, an ORR/OER/HER tri-functional electrocatalyst, comprising distinct Co nanoparticles and MoC components on hollow carbon structure inner and outer layers, has been reported (Fig. 6h).[92] Due to the electronic polarization interface between these two components, charge redistribution at the interface was facilitated. Subsequent investigations demonstrated that Zn–air batteries and water splitting assembled with this catalyst exhibited outstanding catalytic performance and stability (Fig. 6i). Therefore, the coupling strategy between a metal and a semiconductor affords a feasible avenue for designing and developing multifunctional catalysts for the next generation of reversible energy conversion systems.

3.1.3 The coupling of a semiconductor and a semiconductor. In solid-state physics, semiconductor–semiconductor junctions are categorized into homo-type (p–p and n–n types) and hetero-type (n–p type).[115] In homo-type heterojunctions, charge carriers – electrons (n–n type) or holes (p–p type) – flow unidirectionally from lower WF to higher WF components until Fermi levels equilibrate.[116] The connection of p-type and n-type semiconductors results in electron flow from the n-type to p-type, creating positive charge regions near n-type semiconductor junctions. Conversely, carrier holes move from p-type to n-type semiconductors, forming hostile space charge regions near p-type semiconductor junctions.[117] Consequently, a strong electric field develops at the interface, inducing band bending through Fermi-level rearrangement.[118] This band bending facilitates electronic structure redistribution, impacting local coordination and the electronic density of states. This can be engineered to lower the activation energy of reactants and reaction intermediates, thus enhancing electrocatalytic activity.

An n–n heterojunction was successfully fabricated at the biphasic interface by coupling oxygen-vacancy-rich Fe_2O_3 and $ZnCo_2O_4$ using a cation-exchange method as an example (Fig. 7a and b).[93] This heterojunction exhibited exceptional performance with a minimal overpotential of 0.261 V to achieve a current density of 10 mA cm^{-2}. It displayed remarkable stability at high current densities, exceeding that of the majority of Co/Fe-based OER catalysts reported to date (50 hours). DFT calculations validated that the formation of the nanojunction fine-tuned the d-band center, improving the adsorption of oxygen intermediates at the active sites and consequently optimizing the Gibbs free energy of the OER reaction (Fig. 7c). Another illustrative example involves the construction of a $NiSe_2/FeSe_2$ p–p junction prepared through a solid-state selenization method (Fig. 7d–g).[94] The intrinsic electric field formed at the $NiSe_2/FeSe_2$ heterointerface enhanced charge transfer, leading to localized charge redistribution. This increased the conductivity and facilitated the adsorption of

relevant reactants driven by electrostatic interactions. Integrating hetero-type semiconductors with p–n heterojunctions can provide highly efficient catalytic active sites, thereby accelerating the kinetics of electrochemical reaction processes. Taking the FePc/GaS p–n junction as a model, atomic geometric characterization revealed a distortion of the Fe–N$_4$ moiety, thus disrupting the Fe–N coordination configuration and modulating the local charge density and spin configuration of the Fe center (Fig. 7h–k).[95] As a result, the p–n junction catalyst exhibited a comparative ORR activity at 0.850 V, more than twofold that of the original FePc and over twelvefold that of commercial Pt/C catalysts. This strategy could be extended to other n-type sulfide carriers with different WFs, revealing a linear relationship between the ORR activity of loaded Fe–N$_4$ and the rectification degree. This suggested the continuous tunability of SACs by altering n-type carriers.

3.2 Coordination-asymmetric coupling

Asymmetric coordination offers a promising approach to enhance catalytic activity, distinct from the traditional metal–N$_4$ active site model.[119] Incorporating asymmetric ligands or varied coordination environments provides a novel means to precisely regulate the electronic structure and charge distribution of active sites.[120] Based on the coordination attributes, asymmetrical atomic sites can be categorized into three types: low coordination, lateral coordination, and axial coordination.[121] These classifications clearly demonstrate the diverse structural arrangements inherent in coordination-asymmetric coupling. Fig. 8 presents recent research findings using these strategies, offering a concise visual summary of advancements in the field. The advantages of asymmetric coordination structures over conventional M–N$_4$ sites in electrocatalysis primarily include lower overpotential, higher selectivity, and more excellent catalytic performance. SA centers with low coordination display enhanced intrinsic electrocatalytic activity attributed to the optimized electron structure, which lowers the adsorption of oxygen intermediates, consequently improving the activity of metal sites.[47] Structural distortions can induce charge transfer and asymmetric charge distribution in lateral coordination SA systems, optimizing adsorption and desorption behaviors towards oxygen intermediates and reducing energy barriers for the ORR and OER.[48] Axial coordination can also disrupt the symmetry of catalytic centers, optimizing the local coordination environment of active metals, boosting the charge polarization effects, and facilitating charge transfer between metal centers and adsorbed intermediates, thus decreasing the Gibbs free energy of the rate-limiting steps in catalytic reactions.

3.2.1 Low coordination of metal–N$_x$ sites. The coordination environment of the central metal site in SACs influences electrocatalytic performance. By carefully controlling experimental parameters during catalyst synthesis, diverse coordination numbers in M–N$_x$C$_y$ (x, y = 1–4) catalysts can be achieved.[46] This strategy offers precise control over the local structures of the catalyst, thus promoting catalytic efficiency and selectivity.[140] As a demonstration, a surfactant-assisted method was introduced for synthesizing Ni SACs immobilized on a porous NC support (Ni–SA/
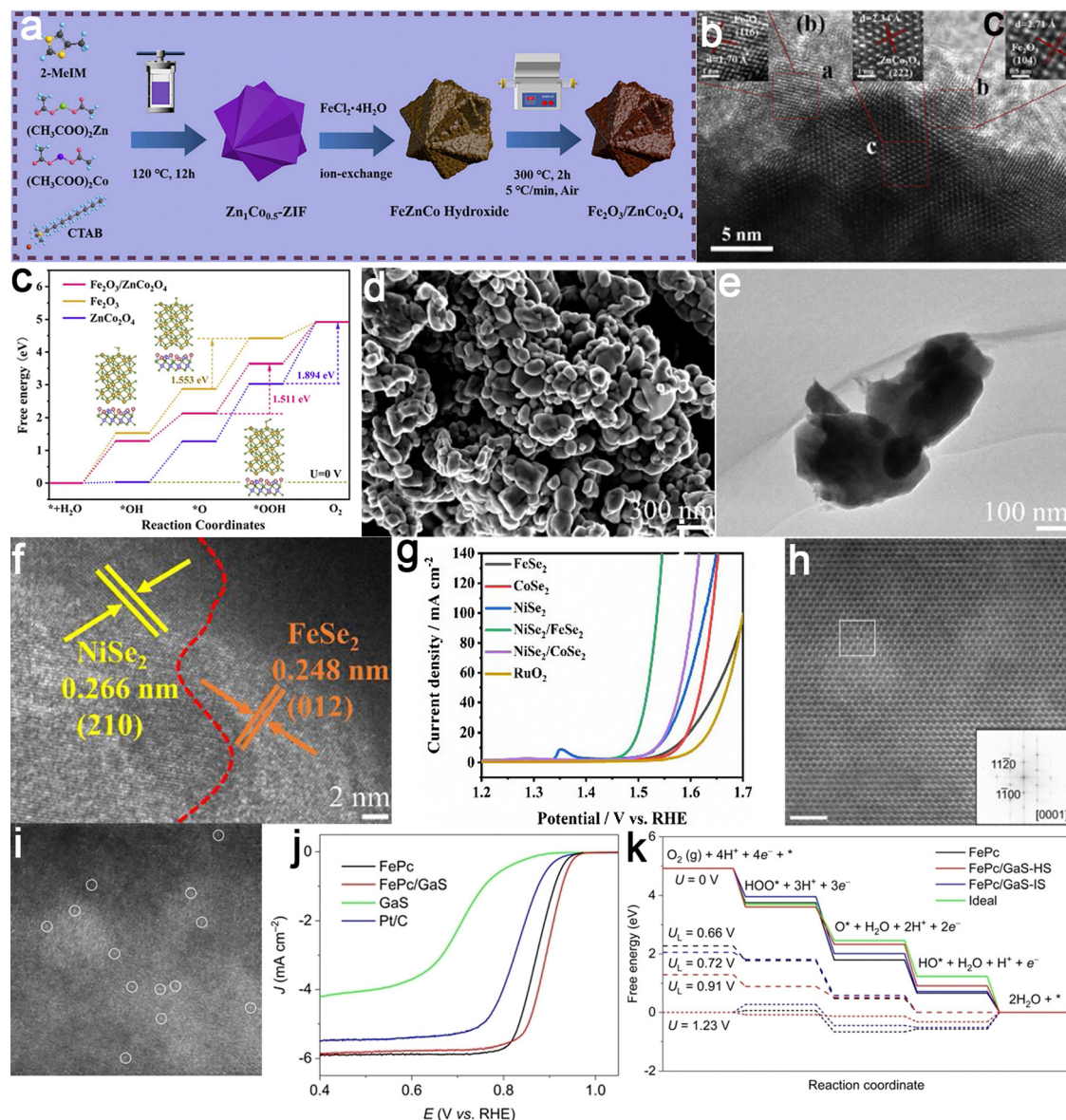
5116 | *Chem. Soc. Rev.*, 2025, **54**, 5108–5145

This journal is © The Royal Society of Chemistry 2025

Fig. 7 Examples of semiconductor–semiconductor coupled electrocatalysts. $Fe_2O_3/ZnCo_2O_4$ catalyst: (a) schematic illustration for the synthetic process; (b) HRTEM images showing the well-defined heterojunction interface; (c) the energetic pathway of the OER, highlighting the reduced energy barriers enabled by the heterojunction design. Reproduced with permission from ref. 93. Copyright 2023, Elsevier. $NiSe_2/FeSe_2$ heterojunction catalyst: (d) SEM, (e) TEM, and (f) HRTEM images showing distinct lattice planes of $NiSe_2$ (210) and $FeSe_2$ (012); (g) LSV curves comparing the electrocatalytic performance of $NiSe_2/FeSe_2$ against benchmark catalysts for the OER. Reproduced with permission from ref. 94. Copyright 2021, Elsevier. FePc/GaS catalyst: (hand i) HAADF-STEM image; and (j) LSV curves illustrating the enhanced ORR performance of FePc/GaS over individual components and (k) free energy diagrams for ORR showing optimized intermediate adsorption energies, confirming the role of electronic coupling in boosting catalytic efficiency. Reproduced with permission from ref. 95. Copyright 2023, John Wiley and Sons.

NC) with $Ni–N_3$ and $Ni–N_4$ coordination (Fig. 9a–c).[122] The HER catalytic performance of these catalysts was investigated using alkaline solution and seawater electrolytes. These findings showed that Ni-SA/NC, featuring a tri-nitrogen coordination structure (Ni–N_3), displayed efficient HER activity (Fig. 9d). X-ray absorption fine structure (XAFS) characterization analysis and DFT calculations demonstrated that the $Ni–N_3$ coordination, characterized by a reduced coordination number compared to the $Ni–N_4$ site, facilitated water dissociation and hydrogen adsorption, thus boosting HER activity (Fig. 9e).

In recent years, attention has been directed towards the rational design of Fe SACs with asymmetrical coordination. Taking the $Fe–N_2$ active site as an example, it was observed that the interaction of OH species occurred with Fe atoms characterized by unsaturated coordination structures (Fig. 9f and g).[123] This led to the creation of the $OH–Fe–N_2$ site, which facilitated O_2 adsorption, promoted the rapid formation of *OOH species at low operating potentials, and contributed to the cleavage of the O–O bond with a lower barrier, thus enhancing the kinetics of the multi-electron transfer reaction. As a result, the resulting
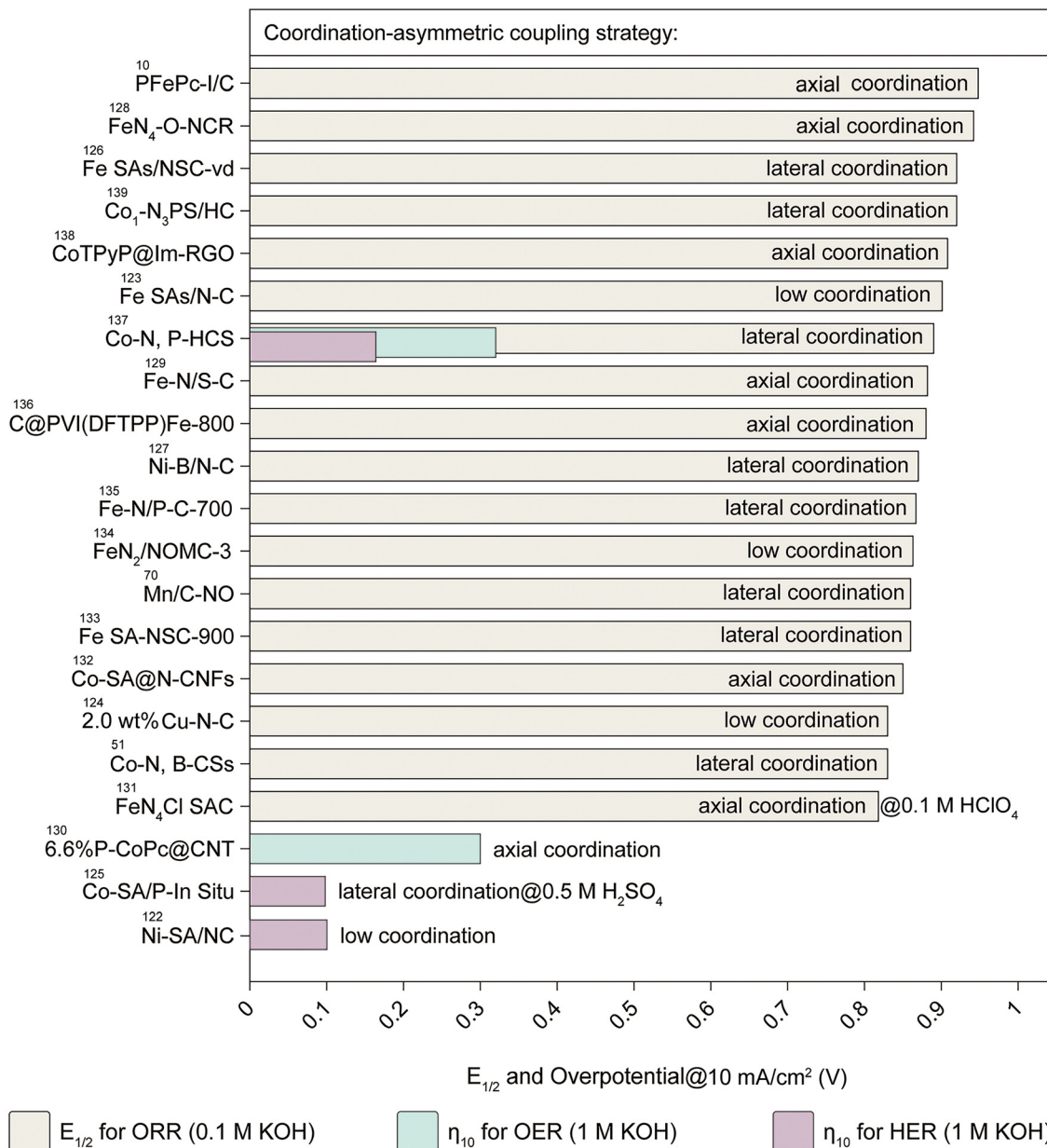
This journal is © The Royal Society of Chemistry 2025

Chem. Soc. Rev., 2025, 54, 5108–5145 | 5117

Fig. 8 Summary of catalytic performances using coordination-asymmetric coupling strategies. The chart categorizes catalysts based on coordination types, including axial coordination, lateral coordination, and low coordination. The performance metrics include the half-wave potential ($E_{1/2}$) for the ORR (0.1 M KOH), the overpotential at 10 mA cm^{-2} (η_{10}) for the OER (1 M KOH), and η_{10} for the HER (1 M KOH). Catalysts with unique coordination environments, such as FePcP/C-I/C with axial coordination or Co–N, B-CSs with lateral coordination, exhibit notable catalytic efficiencies. These findings emphasize the influence of coordination asymmetry in optimizing catalytic sites for specific reactions. Data points also highlight catalysts such as Ni–B/N–C and Co-SAs@N-CNFs for their remarkable activity across multiple coordination designs. This diagram provides a summary of the performance metrics reported in ref. 10, 51, 70 and 122–139.

catalyst demonstrated excellent ORR activity, exhibiting a high kinetic current density (J_k) of 81.3 mA cm^{-2} and an elevated high turnover frequency (TOF) value of 5804 h^{-1} (Fig. 9h). In addition to Fe and Ni, Cu-based SAC has also shown remarkable ORR activity (Fig. 9i–k).[124] Extended X-ray absorption fine structure (EXAFS) and electron energy loss spectra (EELS) verified that Cu SA closely resembled Cu–N$_4$. Electrochemical *in situ* XANES identified the unsaturated Cu$^+$–N$_3$ as the active site for the ORR, with Cu^{2+}–N$_4$ functioning primarily as its precursor. Under

reducing potential, water dissociated into OH$^-$ and protons, facilitating the hydrogenation of pyridinic nitrogen, which in turn drove the transition from Cu^{2+}–N$_4$ to Cu$^+$–N$_3$. These Cu$^+$–N$_3$ SA sites activated O$_2$ by donating electrons to its antibonding orbitals, thereby weakening the O–O bond and promoting its cleavage, ultimately leading to the formation of OH$^-$. During the ORR, Cu–N$_3$ further evolved into Cu–N$_2$, likely due to ligand reorganization under reducing conditions. However, upon removal of the applied potential, the system reverted to its stable
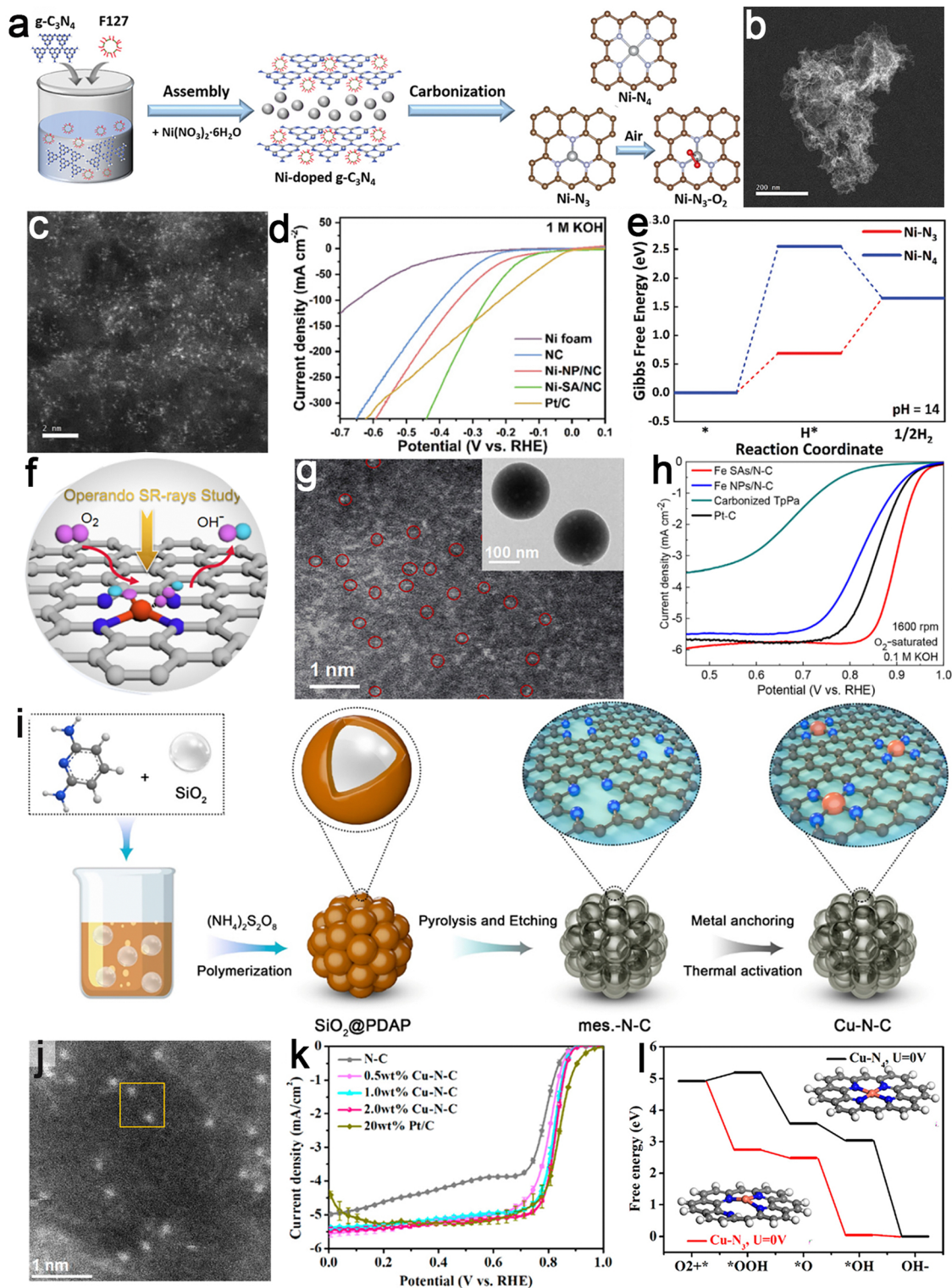
5118 | *Chem. Soc. Rev.*, 2025, **54**, 5108–5145

This journal is © The Royal Society of Chemistry 2025

Fig. 9 Examples of metal–N$_x$ sites with low coordination. Ni-SA/NC catalyst: (a) schematic illustration of the fabrication process; (b and c) HAADF-STEM images showcasing atomic dispersion; (d) HER polarization curves illustrating catalytic performance and (e) the Gibbs free energy diagram highlighting the thermodynamic favorability of HER. Reproduced with permission from ref. 122. Copyright 2021, John Wiley and Sons. Fe SAs/NC catalyst: (f) schematic drawing of the operando synchrotron radiation characterizations; (g) HAADF-STEM image capturing isolated Fe sites and (h) LSV curves demonstrating excellent catalytic activity. Reproduced with permission from ref. 123. Copyright 2021, American Chemical Society. Cu–N–C SAC catalyst: (i) Schematic illustration of the two-step synthesis strategy; (j) HAADF-STEM image; (k) ORR polarization curves showing enhanced catalytic behavior and (l) free energy diagram for the ORR indicating reduced reaction barriers. Reproduced with permission from ref. 124. Copyright 2021, American Chemical Society.

This journal is © The Royal Society of Chemistry 2025

Chem. Soc. Rev., 2025, **54**, 5108–5145 | 5119

$Cu–N_4$ configuration, suggesting a reversible structural evolution (Fig. 9l). Therefore, the SACs with low coordination configuration have demonstrated their potential for practical applications in electrochemical systems.

3.2.2 Lateral coordination of metal–N_xA_y sites. Integrating non-metallic constituents into NC frameworks to enhance the performance of SA catalysts has emerged as an efficient approach.[141] Various dopants have been examined, including S, P, B, I, Cl, and others, resulting in metal–N_xA_y (where A = N, S, P, B, I, and Cl) sites, characterized by a distinctive lateral coordination configuration.[142] Incorporating a metal–P bond, established through the coordination of phosphorus atoms, can alter the electronic configuration of the metal core, thereby improving catalytic efficiency by facilitating electron transfer between the central metal and the carbon substrate.[143] Motivated by this concept, an atomic $Co–P_1N_3$ structure was designed, stabilizing the Co SA with one P atom and three N atoms (Fig. 10a and b).[125] In acidic environments, the resulted catalyst, featuring the $Co–P_1N_3$ structure, exhibited outstanding activity and durability for the HER, with a low overpotential of 0.098 V at 10 mA cm^{-2} and a slight Tafel slope of 47 mV dec^{-1}, outperforming electrocatalysts with the $Co–N_4$ site. The extended
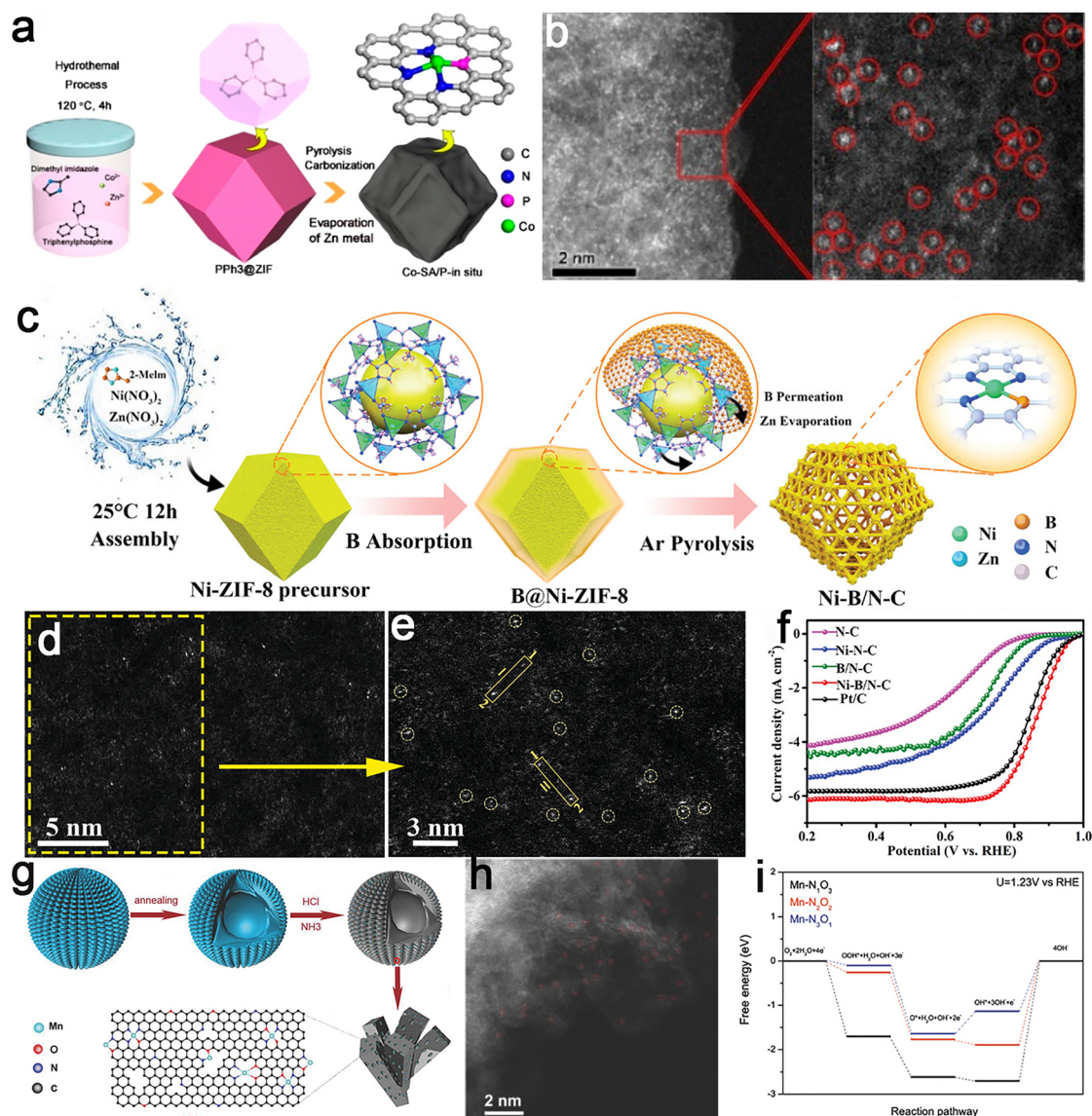

Fig. 10 Examples of metal–N_xA_y sites with lateral coordination. Co-SA/P-*in situ* catalyst: (a) scheme of the formation and (b) HAADF-STEM images of the sample showing atomic dispersion of Co sites. Reproduced with permission from ref. 125. Copyright 2020, American Chemical Society. Ni–B/N–C catalyst: (c) schematic diagram of the preparation process, (d and e) HAADF-STEM images confirming the presence of Ni–B sites, and (f) ORR polarization curves highlighting catalytic performance improvements due to lateral coordination. Reproduced with permission from ref. 127. Copyright 2023, John Wiley and Sons. Mn/C–NO catalyst: (g) schematic illustration of the synthetic process for Mn Sas and (h) HAADF-STEM images of Mn SAs visualizing Mn atomic sites; and (i) free-energy diagram of the ORR on Mn–N_1O_3, Mn–N_2O_2, and Mn–N_3O_1 surfaces demonstrating their catalytic advantages. Reproduced with permission from ref. 65. Copyright 2018, John Wiley and Sons.

5120 | *Chem. Soc. Rev.*, 2025, **54**, 5108–5145

This journal is © The Royal Society of Chemistry 2025

bond length in the high-valence $Co_1–P_1N_3$ atomic structure was identified as a critical factor in enhancing the HER performance. Many investigations have indicated that introducing S atoms into the $M–N_x$ configuration can also enhance the charge delocalization surrounding carbon atoms, improving the ORR performance. As an illustration, a supramolecular self-assembly pyrolysis method was utilized to fabricate an N/S/Fe co-doped carbon material.[126] These asymmetrically coordinated $Fe–N_3S_1$ SA sites demonstrated high TOF values of 18.5 and 2.87 s^{-1} and mass activities of 56.2 and 15.9 A mg^{-1} at 0.87 and 0.74 V in 0.1 M KOH and 0.5 M H_2SO_4, respectively. Experimental results revealed that $Fe–N_3S_1$ sites favored the production of OH^- species, exhibiting distinct kinetic mechanisms in acidic and alkaline solutions. The ORR activity of this catalyst in different electrolytes could be ascribed to the expected coordination structure. In 0.1 M KOH, the coordinated Fe–N functioned as the primary site for activating O_2 adsorption, whereas in 0.5 M H_2SO_4, Fe–S coordination emerged as the primary center for the ORR. DFT calculations further verified that the upward adjustment of the d-band center of $Fe–N_3S_1$ active sites facilitated O_2 adsorption, expediting the kinetic process of reducing *OH. The vacancy defects surrounding the $Fe–N_3S_1$ sites balanced the generation of *OOH and the reduction of *OH, thus collaboratively enhancing the ORR process.

Apart from S and P, incorporating B into the carbon skeleton decreases the d-band center of the metal atom and the adjacent position of the initial peak concerning the Fermi level.[142] This alteration improves the adsorption and desorption of intermediates, thereby promoting the catalytic reaction. Inspired by this, a B-doped Ni–N–C catalyst was developed for efficient ORR (Fig. 10c–e).[127] This catalyst featured atomically dispersed Ni atoms anchored on a carbon support, coordinated with one B atom and three N atoms, forming a $Ni–B_1N_3$ configuration. The prepared Ni–B/N–C catalyst demonstrated enhanced ORR performance (Fig. 10f), with a half-wave potential ($E_{1/2}$) of 0.870 V, surpassing that of the original Ni–N–C (0.760 V). Even after 30 000 cycles, $E_{1/2}$ only degraded by 21 mV, outperforming most reported Fe–N–C and Co–N–C catalysts, indicating remarkable stability. DFT calculations verified that, compared to $Ni–N_4$, the $Ni–B_1N_3$ configuration increased the electron density at the Ni site, improving the adsorption of ORR intermediates and lowering the thermodynamic barrier, thus expediting ORR kinetics. As an illustrative example, O and N atoms were coordinated with Mn sites to fabricate a metal–N_3O_1 configuration, employing conductive 3D graphene frameworks as the substrate.[76] Inspired by enzyme coordination effects, Mn d-electron energy levels were adjusted optimally (Fig. 10g and h). Computational results revealed that $Mn–N_1O_3$, $Mn–N_2O_2$, and $Mn–N_3O_1$ emerged as active sites for the ORR (Fig. 10i). The deliberate downward shift of the d-band center and the proximity of the initial peak to the Fermi level within the $Mn–N_3O_1$ site promoted the desorption of reaction intermediates. This, in turn, optimized the kinetics for the ORR.

The above discussion focused on the lateral coordination of single metal centers. However, the efficiency of these strategies is often constrained by limited electron transfer pathways,

particularly in multi-electron transfer processes, where a single-site configuration may struggle to efficiently accommodate reaction intermediates with varying electronic structures and binding affinities. While homonuclear dual-atom catalysts have been proposed to enhance multi-electron reactions, such as the ORR and OER, they still face similar limitations—two identical metal atoms may not fundamentally overcome the constraints of single-site configurations. Instead, alternative approaches involving out-of-plane architectures or DMACs may provide a more effective means to modulate electronic structures, facilitate charge delocalization, and optimize intermediate stabilization, ultimately improving catalytic activity and stability.

For example, a high-density asymmetric dual-iron atom catalyst, $A–Fe_2S_1N_5@N/S$ co-doped carbon, was synthesized using a multilayer stabilization strategy involving defect capture and coordination riveting.[144] The asymmetric nitrogen–sulfur coordination around the dual-iron sites modulated the electronic structure, leading to enhanced adsorption and activation of oxygen intermediates. Specifically, this asymmetric coordination strengthened Fe–O interactions, promoting more efficient reactant conversion, lowering energy barriers, and accelerating reaction kinetics. These findings highlight the potential of asymmetric coupling strategies to further advance single-atom and dual-atom catalysts, offering new pathways for designing efficient electrocatalysts.

Coordination asymmetry strategies also play a crucial role in the design of molecular ORR catalysts. For example, metal porphyrins consist of a central metal ion coordinated to a ring of four nitrogen atoms.[145,146] This coordination enables strong catalytic activity for oxygen reduction. Specifically, iron and cobalt porphyrins promote oxygen molecule adsorption and reduction, demonstrating catalytic activity comparable to that of platinum-based catalysts.[147] However, the catalytic performance and stability of metal porphyrins are highly sensitive to the electronic structure of the metal center, the ligand environment, and interactions with reactants. Optimizing their coordination structure is thus important to enhance ORR activity. For instance, introducing substituents at the side coordination sites of the porphyrin structure can tune the electronic properties of the catalyst, improving both its activity and selectivity.[148] Notably, the asymmetric Pacman-type dinuclear cobalt porphyrin catalyst exhibited higher activity compared to its symmetric counterpart,[149,150] highlighting the advantages of asymmetric design in promoting the ORR and further underscored the potential of asymmetric structures in molecular catalysis. This research provides valuable insights for the future development of small-molecule activation catalysts, particularly in improving catalytic performance, selectivity, and stability.

3.2.3 Axial heteroatom coordination. Over the past two years, considerable attention has been directed towards Fe–N_5-C SACs, characterized by their distinctive penta-coordinated configuration.[151] The axial placement of the fifth nitrogen ligand plays a crucial role, causing an electron pull–push effect and imposing steric effects on individual atom sites. This interaction influences the binding affinity between active sites and reaction intermediates, enhancing activity for the axially

This journal is © The Royal Society of Chemistry 2025

Chem. Soc. Rev., 2025, **54**, 5108–5145 | 5121

modified SACs.[152] In contrast to conventional metal–N_4 SACs, the strategic introduction of one or multiple additional ligands in the axial position, either perpendicular or non-coplanar to the planar metal–N_4 sites in SACs, is expected to disrupt electron distribution symmetry.[153] This alteration in the electronic structure of the central SA active sites optimizes adsorption behavior and reduces energy barriers for intermediate adsorption. The axial ligand incorporated over the central SA sites serves as an additional adsorption site, synergizing with the metal–N_4 site for electrocatalysis, ultimately reshaping reaction pathways to be more energetically favorable.[154]

Typically, a porous FeN_4–O–NCR electrocatalyst, rich in catalytically accessible FeN_4–O sites (wherein the Fe SAs are coordinated to four in-plane N atoms and one subsurface axial O atom), supported on N-doped carbon nanorods (NCR), has been reported (Fig. 11a and b).[128] The resulting FeN_4–O–NCR electrocatalyst exhibited a hierarchically porous architecture, featuring a substantial specific surface area (1159 m^2 g^{-1}) and an abundance of FeN_4–O active sites conducive to optimal oxygen adsorption and activation. In Fig. 11c, the FeN_4–O–NCR catalyst displayed remarkable ORR activity and stability in alkaline media ($E_{1/2}$ = 0.942 V). DFT calculations unveiled a precise tailoring of the d-orbital electronic structure of Fe cations, effectively reducing the thermodynamic barrier for the ORR (Fig. 11d). Considering the impact of OH doping on axial coordination and electron transfer, a self-sacrificial strategy was proposed for synthesizing asymmetrically N and S-coordinated Fe_{SA} sites.[129] This strategy embeds an axial fifth hydroxy (OH) coordination (Fe–N_3S_1OH) within N, S co-doped porous carbon nanospheres (Fe–N/S–C) (Fig. 11e). The distinctive structure of Fe-N_3S_1OH, characterized by inherent high activity and a large specific surface area (2539 m^2 g^{-1}), ensured sufficient exposure to active sites. Coupled with an interconnected layered porous structure facilitating rapid ion/mass transfer, the fabricated Fe–N/S–C exhibited outstanding ORR catalytic activity.

In a recent study, metal phthalocyanine (M-Pc) was used as a model for M–N_4 electrocatalysts to explore the positive impact of axial ligands on catalytic activity. M–Pc complexes consist of metal ions coordinated with phthalocyanine ligands, forming distinct M–N_4 active centers that exhibit unique electronic structures and stability, making them valuable molecular catalysts for the ORR.[155] However, their planar, symmetric structure weakens O_2 adsorption and activation, resulting in low ORR catalytic efficiency. Breaking this symmetry is an effective strategy to enhance performance. For example, modifying the axial direction of the metal center by coordinating it with a single metal atom on graphene via a bridging oxygen atom induces symmetry-breaking, promoting out-of-plane polarization, and facilitating O_2 adsorption, thereby improving ORR catalytic efficiency.[156] In parallel, axial PO_4 coordination was introduced at the Co_1N_4 site in CoPc@CNT (CNT stands for carbon nanotube, Fig. 11f–h).[130] This regulation of reaction pathways demonstrated the capability to enhance intrinsic OER activity (Fig. 11i). A similar phenomenon has been observed in metal porphyrin systems. By introducing imidazole groups

axially to the metal center, the original square-planar coordination was disrupted. This axial ligand induced a "push-electron effect", which increased the electron density at the metal site, thereby facilitating the binding and activation of O_2 at the metal center.[157] Comparable to heteroatoms coordinated laterally, axially coordinated heteroatoms impact the catalytic efficacy of central metal sites via the regulation of the electronic structure. The axial coordination of heteroatoms may also initiate the displacement of metal atoms along the axial direction, consequently altering the length of coordination bonds and influencing the behavior of adsorption/desorption for intermediates.

3.3 Size-asymmetric coupling

Electrocatalysts are classified into three groups based on size: SA-type (0.1–0.2 nm), cluster-type (0.2–1 nm), and particle-type (>1 nm).[158] Earlier research on hydrogen and oxygen electrocatalysis focused on particle-type TMCs as alternatives to precious metal benchmarks.[159] However, clusters and SAs have recently gained attention due to their unique physicochemical properties. Size reduction can enhance the electrocatalyst surface area and atomic utilization efficiency. Smaller particles will alter the electronic structure, surface morphology, and metal–support interactions, impacting catalytic selectivity. Reduced cluster size can increase coordinatively unsaturated atoms, enhancing reactivity, while sub-nanometer catalysts generate diverse crystal facets and defects.[54] Despite recent progress, SAs and clusters exhibit limitations in providing multiple active sites for complex multi-step catalytic reactions, impeding their practical application. Recent studies highlight the synergistic interaction among SAs, clusters, and particles in interface regulation to enhance electrocatalytic performance.[55] Incorporating metal clusters or particles near SA centers can modify the rate-determining step of catalytic reactions, lowering the energy barrier associated with these steps. Simultaneously, the non-coherent vibrations induced by these clusters or particles can reduce the bond length of the SA, thereby boosting its stability (Fig. 12).[56]

For example, a Fe–N–C electrocatalyst exhibiting size asymmetry was developed. N-coordinated Fe clusters were positioned adjacent to closely surrounding Fe–N_4 sites, utilizing two-dimensional N-doped porous carbon as a substrate (2DNPC) (Fig. 13a–f).[160] The rapid electron transfer pathway and short interaction distance facilitated robust electronic interactions between the Fe clusters and adjacent Fe–N_4 moieties (Fig. 13g and h). The incorporation of Fe clusters serves a dual purpose: restructuring rate-determining steps and fortifying stability in SAs through reduced bond lengths. Consequently, this composite catalyst exhibited strong adsorption of OH, leading to the permanent grafting of the OH ligand onto the Fe–N_4 site. This OH ligand optimized the binding strength of the Fe–N_4 site with the ORR intermediates on the opposite side, lowering the limiting energy barrier. In contrast, nanoparticles also play a pivotal role in adjusting the local structures of SA sites, refining intermediate adsorption/activation, and enhancing electrocatalytic performance. For example, a
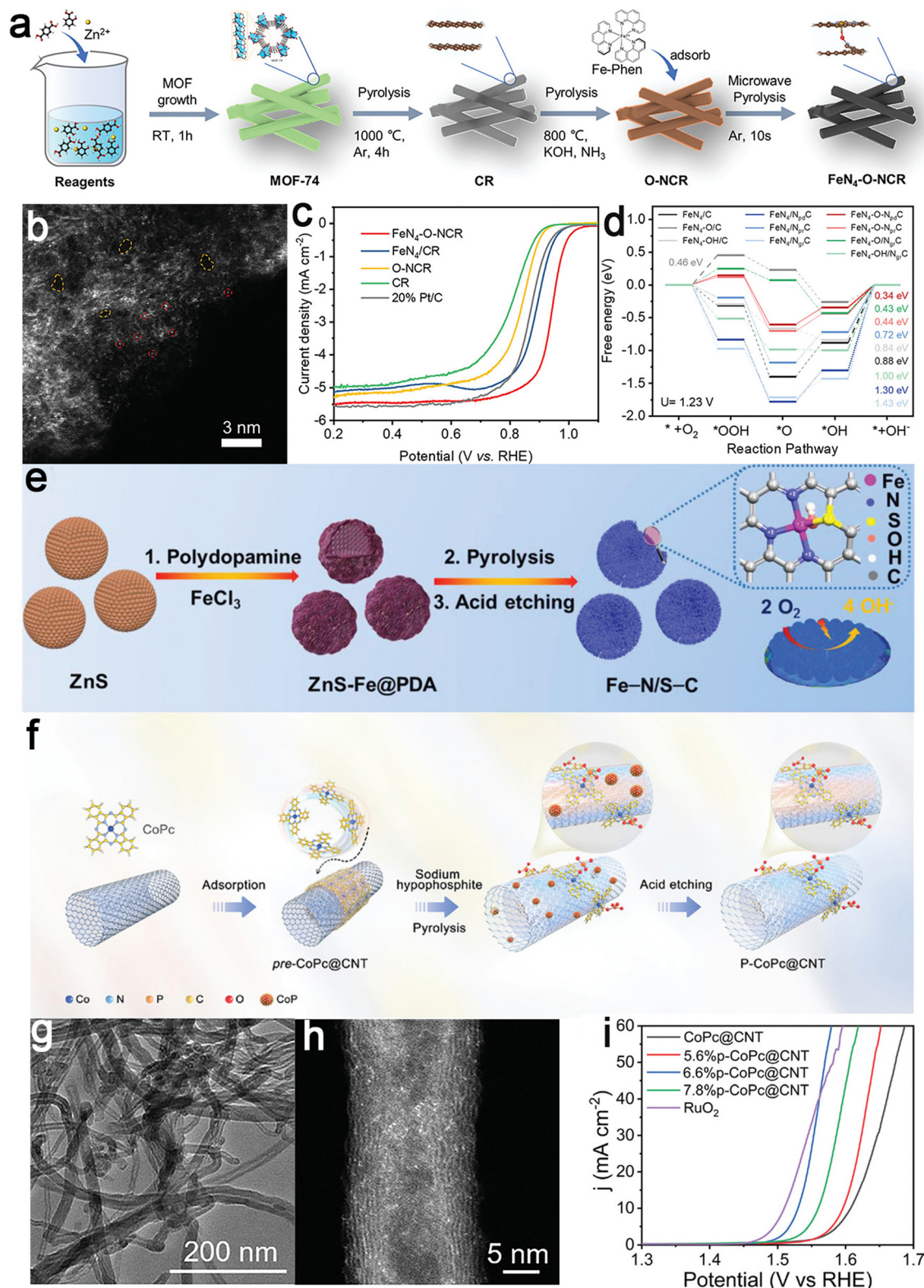
5122 | Chem. Soc. Rev., 2025, 54, 5108–5145

This journal is © The Royal Society of Chemistry 2025

Fig. 11 Examples of axial heteroatom coordination catalysts. FeN$_4$–O–NCR catalyst: (a) schematic synthesis illustration and (b) HAADF-STEM image showing atomic dispersion; (c) LSV curves in 0.1 M KOH highlighting catalytic activity and (d) free energy diagram comparing various FeN$_4$-based models. Reproduced with permission from ref. 128. Copyright 2022, John Wiley and Sons. Fe–N/S–C catalyst: (e) Schematic illustration of the synthetic procedure of the Fe–N/S–C catalyst. Reproduced with permission from ref. 129. Copyright 2022, John Wiley and Sons. 6.6%P–CoPc@CNT catalyst: (f) the schematic illustration of the preparation process and (g) the TEM image depicting the overall structure; (h) the HAADF-STEM image showing atomic resolution of active sites; and (i) polarization curves of various catalysts in 0.1 M KOH, demonstrating performance enhancement through axial coordination. Reproduced with permission from ref. 130. Copyright 2023, John Wiley and Sons.
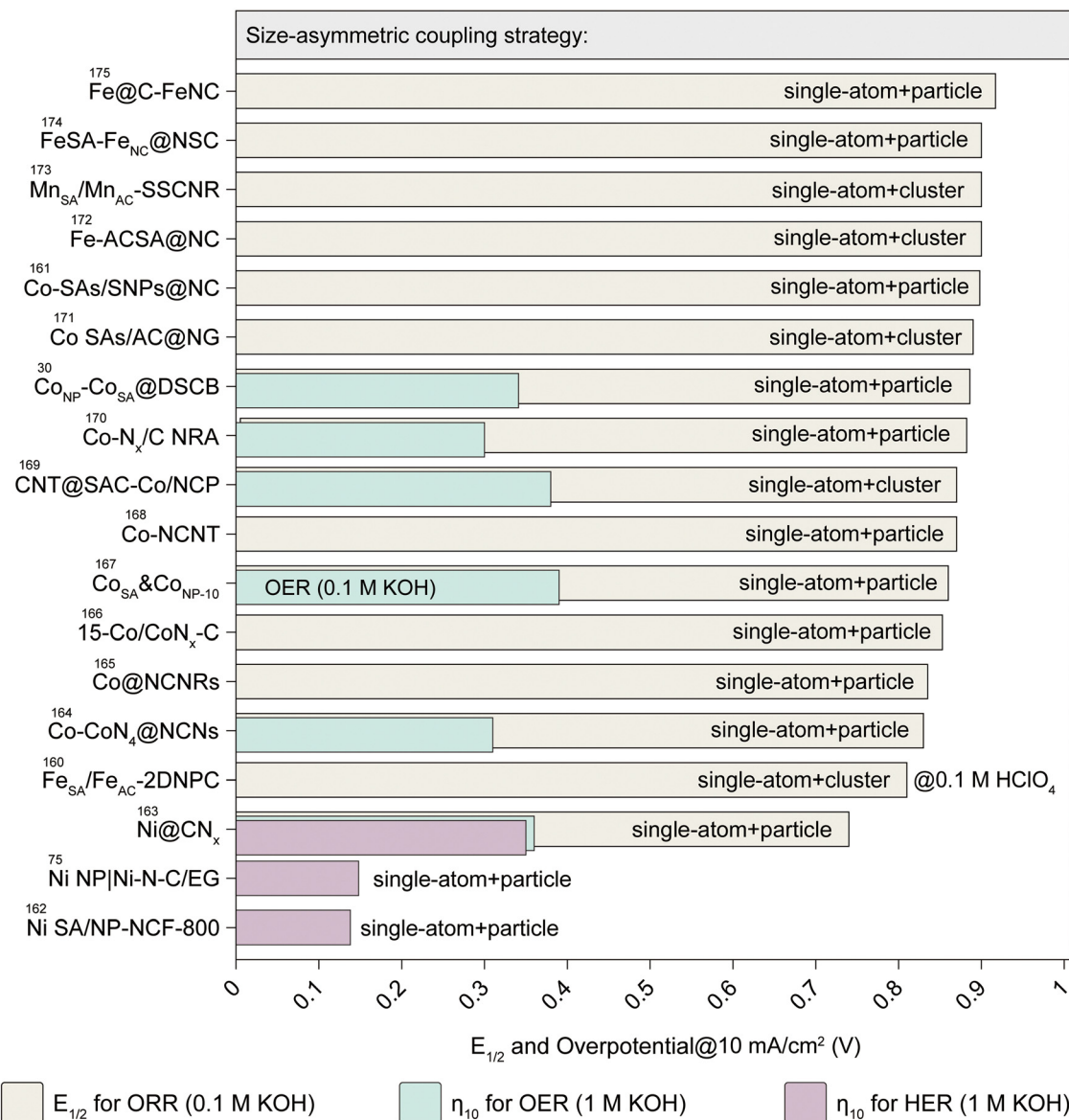
Fig. 12 Performance summary of catalysts designed with size-asymmetric coupling strategies. The figure categorizes catalysts based on coupling configurations such as single-atom + particle and single-atom + cluster. Performance metrics include half-wave potential ($E_{1/2}$) for the ORR in 0.1 M KOH, overpotential (η_{10}) at 10 mA cm^{-2} for the OER in 1 M KOH, and the HER in 1 M KOH. It highlights the impact of size-asymmetric coupling on catalytic activity and efficiency across various reaction types. This diagram provides a summary of the performance metrics reported in ref. 30, 75 and 160–175.

binuclear site consisting of Co SAs in the configuration of Co–N$_4$ moieties and Co nanoparticles (SNPs) was co-anchored on a porous NC nanocage (denoted as Co-SAs/SNPs@NC, Fig. 13i–k).[161] Taking advantage of the combined effects of Co SAs and Co particles, along with the improved anti-corrosion ability of the carbon matrix, this product exhibited remarkable ORR activity ($E_{1/2}$ = 0.898 V) and exceptional stability in alkaline environments, as illustrated in Fig. 13l. DFT calculations revealed that the strong interaction between Co particles and Co–N$_4$ sites increased the valence state of active Co atoms and mitigated the adsorption-free energy of intermediates in the ORR, thereby promoting the reduction of O$_2$ (Fig. 13m and n). The assembled Zn–air battery showed a maximum power

density of 223.5 mW cm^{-2}, a substantial specific capacity of 742 W h kg^{-1} at 50 mA cm^{-2}, and great cycling stability.

In another illustration, a facile synthetic strategy was presented to co-anchor FeN$_4$, and Fe-nanoclusters/nanoparticles on a multichannel carbon nanofiber (FeN$_4$–Fe$_{NCP}$@MCF).[74] This configuration led to the development of a highly efficient and robust ORR catalyst. The exceptional ORR activity and stability demonstrated by the synthesized FeN$_4$–Fe$_{NCP}$@MCF catalyst could be ascribed to the synergistic effects between the FeN$_4$ sites and Fe nanoclusters/nanoparticles, along with the high-porosity structure of the carbon substrate. Indeed, employing the size-asymmetric coupling strategy to integrate individual atoms and clusters/nanoparticles within a unified
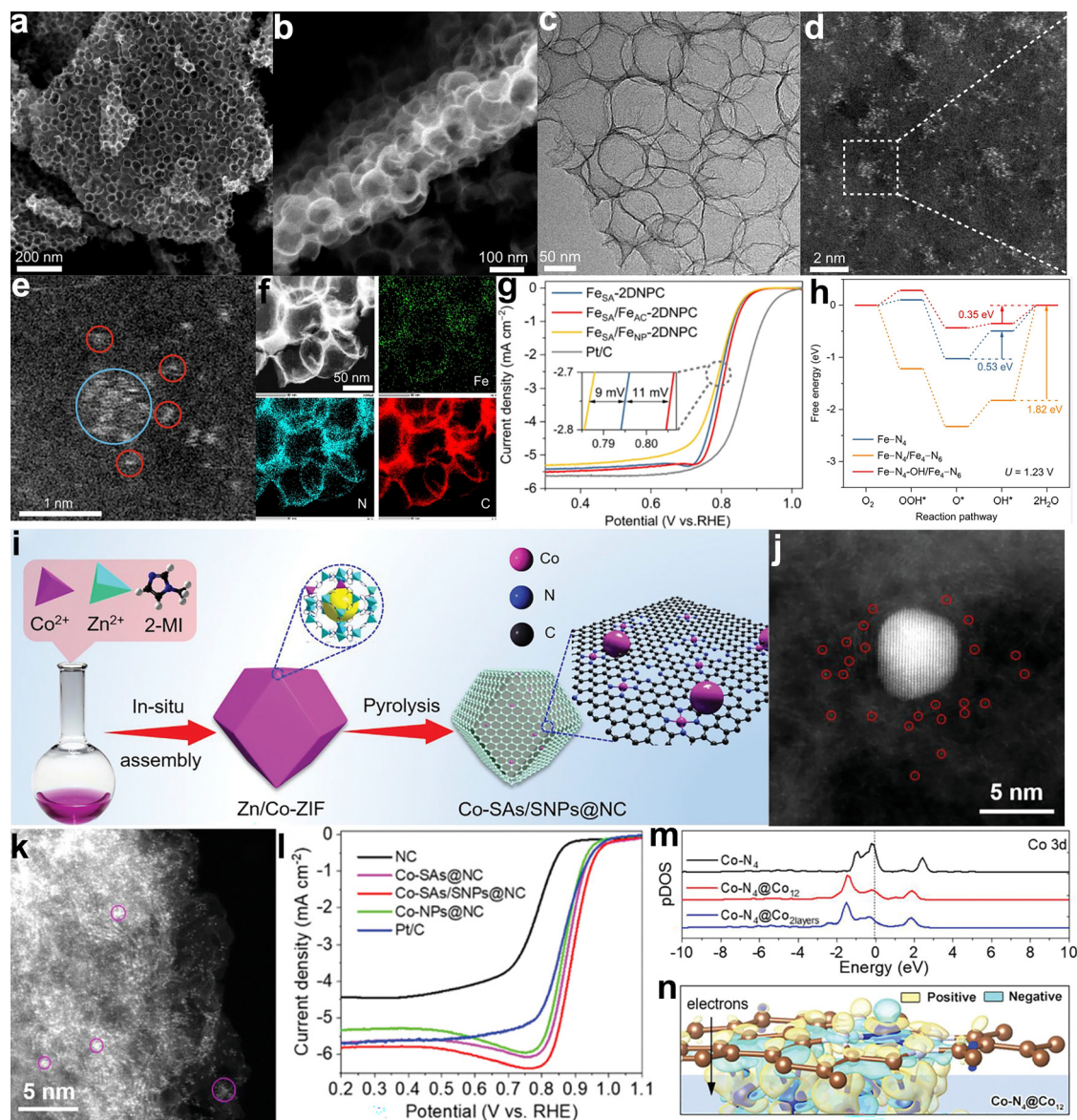
5124 | *Chem. Soc. Rev.*, 2025, **54**, 5108–5145

This journal is © The Royal Society of Chemistry 2025

Fig. 13 Examples of size-asymmetric coupling catalysts. Fe_{SA}/Fe_{AC}−2DNPC catalyst: (a) SEM and (b and c) TEM images; (d and e) HAADF-STEM images with zoom-in image showing an iron cluster (cyan circle) and its satellite iron atoms (red circles); (f) energy-dispersive spectroscopy mapping image illustrating elemental distribution; (g) ORR polarization curves comparing catalytic performance and (h) free energy diagrams over three types of active sites. Reproduced with permission from ref. 160. Copyright 2022, Springer Nature. Co-SAs/SNPs@NC catalyst: (i) schematic illustration of the synthetic process, (j and k) HAADF-STEM images displaying cobalt single atoms and nanoparticles and (l) ORR polarization curves highlighting enhanced activity; (m) calculated projected density of states of Co d band in Co−N_4, Co−N_4@Co_{12}, and Co−N_4@Co_2 layers; and (n) the charge density difference for Co−N_4@Co_{12}, where yellow and blue regions represent electron accumulation and depletion, respectively. Reproduced with permission from ref. 161. Copyright 2021, John Wiley and Sons.

system affords a promising avenue for achieving synergistic coupling. This approach optimizes the electronic structure and enriches oxygen catalytic sites, thus enhancing catalytic performance.

3.4 Multiple asymmetric coupling

Multiple asymmetric coupling refers to two or more asymmetric configurations within material structures, offering a versatile approach for fabricating highly efficient electrocatalytic materials.[176] The recent development described in Fig. 14 shows the performance summary of this strategy in catalyst design, as

evidenced by its enhanced performance. The utilization of this multiple asymmetric coupling can enhance both the activity and stability of catalysts. By applying this method to the design of bifunctional catalysts, active sites with different compositions and catalytic functionalities can be initially coupled. Moreover, introducing concepts of size or coordination asymmetry can further optimize the local electronic structure of active metals, thereby promoting charge delocalization. This optimization provides operational space for accelerating the kinetics of electrocatalytic reactions.
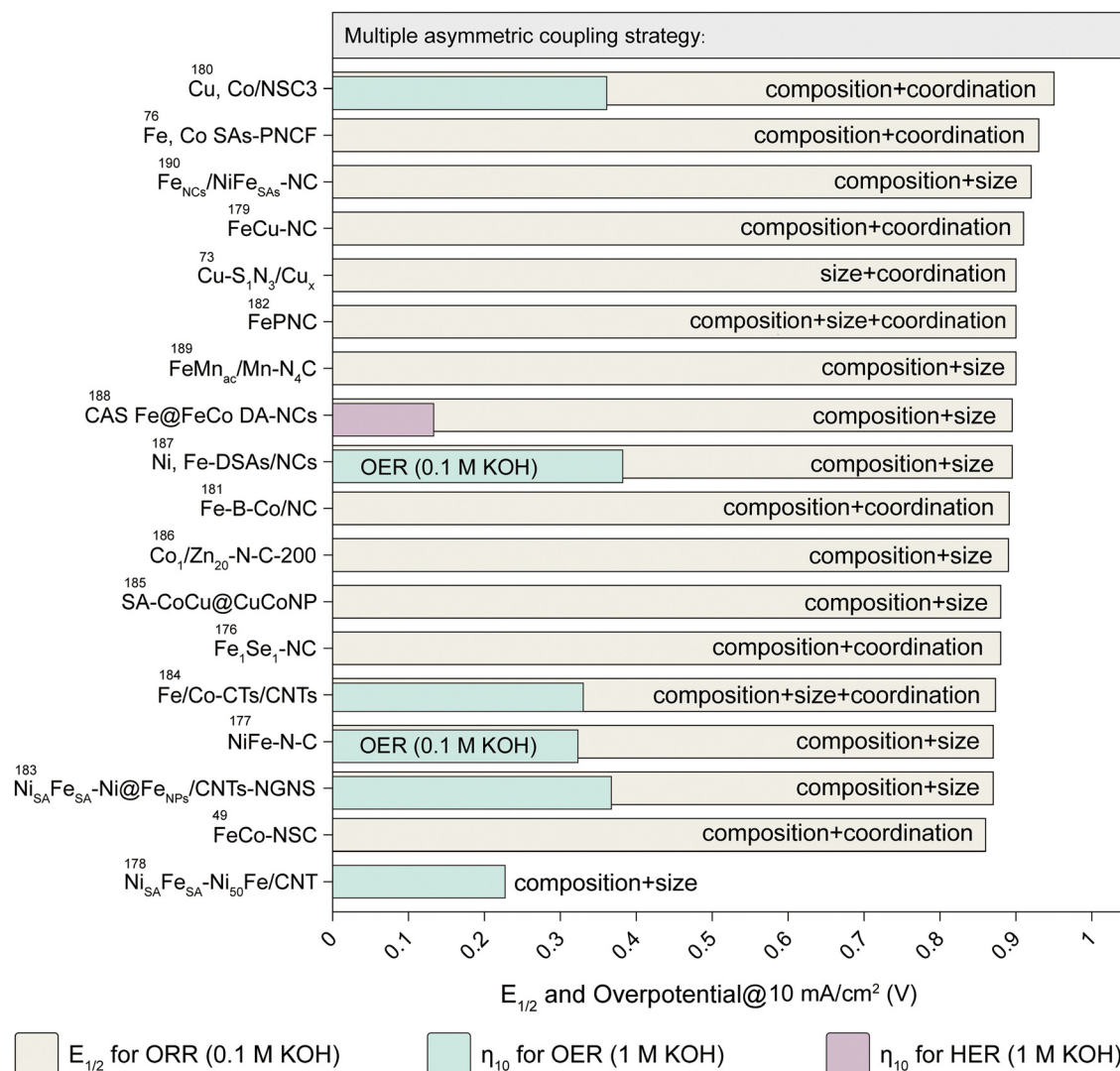
This journal is © The Royal Society of Chemistry 2025

Chem. Soc. Rev., 2025, **54**, 5108–5145 | **5125**

Fig. 14 Performance summary of catalysts designed using multiple asymmetric coupling strategies. The chart categorizes catalysts based on combinations of composition, size, and coordination asymmetries, illustrating their electrocatalytic performance. The metrics include half-wave potential ($E_{1/2}$) for the ORR in 0.1 M KOH and overpotentials (η_{10}) for the OER and the HER at 10 mA cm^{-2} in 1 M KOH, highlighting the enhanced activity achieved through strategic coupling approaches. This diagram provides a summary of the performance metrics reported in ref. 49, 73, 76 and 176–190.

For instance, a dual-metal NiFe–N–C SA catalyst coupling with Fe nanoclusters was prepared by simply pyrolyzing metal phthalocyanine and NC precursors (Fig. 15a and b).[177] This catalyst demonstrated size asymmetry, featuring Fe nanoclusters and Fe SAs and heteroatomic coupling involving Ni SAs. As a result, NiFe–N–C delivered notable ORR/OER catalytic activity and durability (Fig. 15c and d). After 50 000 and 90 000 potential cycles, minimal ΔE was merely 0.680 V, with negligible degradation observed for $E_{1/2}$ and E_{j10}. In-depth characterization and DFT calculations suggest the presence of Ni–N$_4$ and Fe–N$_4$ coordination structures, along with electron synergistic effects from adjacent Fe nanoclusters (Fig. 15e). The key active sites were Fe–N$_4$, Ni–N$_4$, and Fe nanoclusters, with Fe$_4$ at the Ni–N$_4$ site exhibiting the lowest overpotential. The synergy between Fe–N$_4$ and Ni–N$_4$ optimized the electronic structure, improving oxygen intermediate adsorption/desorption and enhancing

OER/ORR activity. Fe nanoclusters further accelerated reaction kinetics, while spin-state modulation refined the reaction pathway. This synergy efficiently optimized oxygen intermediate formation and dissociation, boosting catalytic efficiency. Employing this dual asymmetry in the component and size, analogous electrocatalytic materials, such as Fe$_2$O$_3$/Fe$_{SA}$@NC, Ni$_{SA}$Fe$_{SA}$–Ni$_{50}$Fe@carbon nanotube, and W$_{SA}$–W$_3$N$_4$@NC, have been successively synthesized and applied in electrolysis for water electrolysis and Zn–air batteries.[178,191,192] Similarly, the simultaneous exploitation of asymmetry in both component and coordination emerges as a viable strategy for developing robust electrocatalysts. For example, a two-dimensional metal–organic framework (MOF) nanosheet containing Fe and Cu components was initially prepared, followed by calcination to produce a distinctive asymmetric FeN$_3$O–CuN$_4$ dual-atomic coordination configuration (Fig. 15f and g).[179] Introducing

5126 | *Chem. Soc. Rev.*, 2025, **54**, 5108–5145

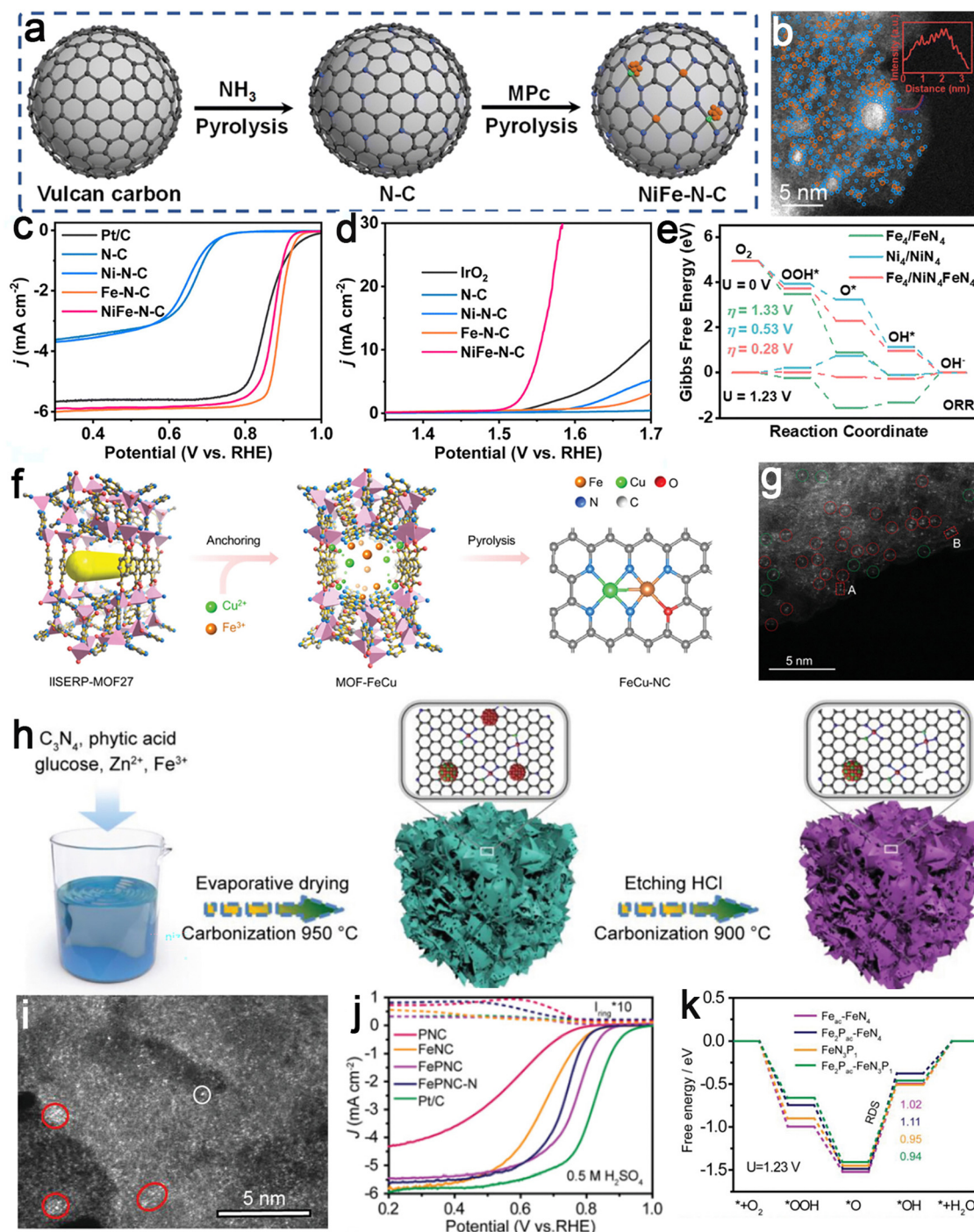This journal is © The Royal Society of Chemistry 2025

Fig. 15 Examples of multiple asymmetric coupling catalysts. NiFe−N−C catalyst: (a) preparation strategy and (b) HAADF-STEM images (the inset in (b) shows the interplanar spacing of the metal nanoclusters); (c) ORR polarization curves and (d) OER polarization curves of various catalysts; and (e) Gibbs free energy diagrams of the ORR on $Fe_4@Fe-N_4$, $Ni_4@Ni-N_4$ and $Fe_4@Ni/Fe-N_4$ (Fe_4 on the $Ni-N_4$ site). Reproduced with permission from ref. 177. Copyright 2023, Royal Society of Chemistry. FeCu−NC catalyst: (f) synthetic procedure and (g) HAADF-STEM image highlighting SAs (green dashed circles) and dual atoms (red dashed circles). Reproduced with permission from ref. 179. Copyright 2023, John Wiley and Sons. $FeN_3P_1–Fe_2P@NC$ catalyst: (h) schematic of the preparation and (i) HAADF-STEM image; (j) ORR polarization curves of various catalysts and (k) free energy diagram for $Fe_{ac}–FeN_4$, $Fe_2P_{ac}–FeN_4$, FeN_3P_1, and $Fe_2P_{ac}–FeN_3P_1$ at 1.23 V. Reproduced with permission from ref. 182. Copyright 2023, John Wiley and Sons.

non-metallic oxygen atoms into the carbon substrate disrupted the electronic/geometric symmetry of M–N$_4$, inducing charge distribution polarization. This enabled the adjustment of the d-band centers of the catalyst, thereby lowering the binding energy of the ORR intermediates. Cu–N$_4$ disrupted the localization of Fe-3d orbital electrons, speeding up electron transfer and optimizing the adsorption of OH* intermediates, thus promoting the ORR process. Similar operative mechanisms

This journal is © The Royal Society of Chemistry 2025

Chem. Soc. Rev., 2025, **54**, 5108–5145 | 5127

have also been validated at asymmetric Cu–N–S/Co–N–S and Fe–B–Co/NC sites.[180,181]

Using the synergistic coordination of asymmetry- and size-asymmetric coupling, the local microenvironment of catalysts can also be precisely modulated in two dimensions. For example, an atomic catalyst with adjustable coordination environments, featuring single copper sites (CuN_4 or CuS_1N_3) and adaptable copper clusters (Cu_x), was developed for efficient electrocatalytic ORR.[73] Theoretical analyses indicated that the asymmetric coordination environment and charge redistribution induced by Cu_x effectively enhanced the *OOH intermediate adsorption. The regulation of intermediate adsorption rendered CuS_1N_3/Cu_x great in the ORR process compared to catalysts lacking S atoms or Cu_x. The adsorption energy of *OOH on the single Cu site, regulated by the coordination environment and interface interactions, exhibited a linear relationship with the d-band center. This suggests that intermediate adsorption strength and d-band center are robust indicators of catalytic performance. This study provides a comprehensive regulatory strategy for electron configuration and intermediate adsorption behavior, potentially applicable to other proton-coupled electron transfer reactions.

The multiple asymmetric coupling strategy was recently employed to fabricate a FeN_3P_1–Fe_2P@NC nanohybrid.[182] This material comprised Fe_2P nanoclusters, nanoparticles, and an NC substrate for accommodating the asymmetric N, P coordination of Fe_{SA} centers, thus exhibiting a tripartite asymmetric coupling structure in component, size, and coordination environment (Fig. 15h and i). Owing to its unique asymmetric electronic/geometric configuration, the synthesized catalyst demonstrated outstanding ORR activity, with decent $E_{1/2}$ values of 0.76 V (0.5 M H_2SO_4) and 0.90 V (0.1 M KOH) and great performance in Zn–air batteries. Theoretical analysis showed that the synergistic interaction between P-coordination and Fe_2P nanoclusters lowered the adsorption energy and over-potential of *O hydrogenation, optimized OH adsorption, and facilitated the reaction. Furthermore, the introduction of Fe_2P induced electron redistribution, breaking the localized electronic structure of the Fe sites, thereby accelerating electron transfer and improving reaction kinetics (Fig. 15j and k). Therefore, employing a multiple asymmetric coupling strategy offers convenience and various dimensions for effectively modulating the phase, component, structure, morphology, and defects of catalysts. This approach provides advantages in developing high-performance and stable electrode materials.

4. Enhancement mechanism of performance in the asymmetric coupling

4.1 Charge transfer

Charge transfer involves the redistribution and directed charge transport between a "donor" and an "acceptor". A prevalent strategy in electrocatalysis is optimizing components and structure, facilitating electron transfer to promote catalytic activity and stability. Electrocatalysts characterized by compound structures

incorporating heterojunctions may exhibit behavior associated with charge transfer, thus boosting catalytic activity.[193] Constructing heterojunctions is an efficient method for modifying the electron structure to modulate catalytic activity, employing the inherent diversity in electron structures among individual components within the composite catalyst.[194] A compositionally asymmetric W_2N/WC heterogeneous catalyst was prepared through simultaneous nitridation and carbonization processes (Fig. 16a).[195] The resulting W_2N/WC catalyst demonstrated highly efficient and durable catalytic ability for the ORR, OER, and HER. Notably, the ORR half-wave potential reached 0.810 V, with OER overpotential at a mere 0.320 V, and HER overpotential at only 0.149 V. When employed as the air electrode in Zn–air batteries, the W_2N/WC catalyst enabled the battery to achieve a high-power density of 172 mW cm^{-2}. DFT calculations elucidated that the well-regulated W_2N/WC heterointerface facilitated the charge transfer and separation (Fig. 16b and c), enhancing ORR, OER, and HER activities.

In recent times, extensive research has focused on the asymmetric coupling of heterogeneous components. These instances exploited variations in physicochemical properties, including electronegativity and WF, to prompt interface charge redistribution, effectively influencing electrochemical performance. Relevant examples include Er_2O_3-Co, Mo_5N_6-MoS_2, Co/Co_xM_y (M = P, N), Ni/CeO_2, and other similar cases.[113,117,198,199] Utilizing the coupling of homogeneous metal SAs and clusters provides an avenue for achieving interface charge transfer. For example, a multi-step synthesis strategy involving coating, thermal decomposition, and etching was designed to prepare Fe cluster-modified Fe–N–C atomic centers characterized by a distinctive size-asymmetric feature (Fig. 16d).[172] The interaction between Fe–N–C and the Fe clusters induced charge redistribution, with electrons from the Fe center transferring to the adjacent carbon substrate. This increased the positive charge density on the Fe center, weakening the adsorption strength of *OH (Fig. 16e and f). As a result, the desorption energy barrier of the *OH intermediate on the Fe active sites was lowered, accelerating ORR kinetics. Additionally, the presence of both atomic Fe–N–C and metallic Fe clusters caused elongation of the Fe–N bond, altering the coordination environment of Fe–N–C. This structural adjustment facilitated electron transfer (Fig. 16g), promoting the 4-electron transfer pathway and enhancing overall catalytic efficiency.

Recent investigations have broadened the scope of interaction dynamics between SAs and clusters, including homo-nuclear and heteronuclear systems. By employing a multi-asymmetric strategy, Co atomic clusters were strategically incorporated to finely tune the electronic structure of Fe–N_4, enhancing ORR activity (Fig. 16h and i).[196] These findings revealed that, in the Co_4/Fe_1@NC and Fe_4/Fe_1@NC systems, the O–O bond stretching was more pronounced than in the FeN_4 system, facilitating O_2 dissociation at the FeN_4 active sites. This improvement was largely driven by electron transfer induced by the coupling of Co_4 clusters with FeN_4 sites, which redistributed charge and altered the electronic structure of the FeN_4 sites, ultimately enhancing their catalytic activity.
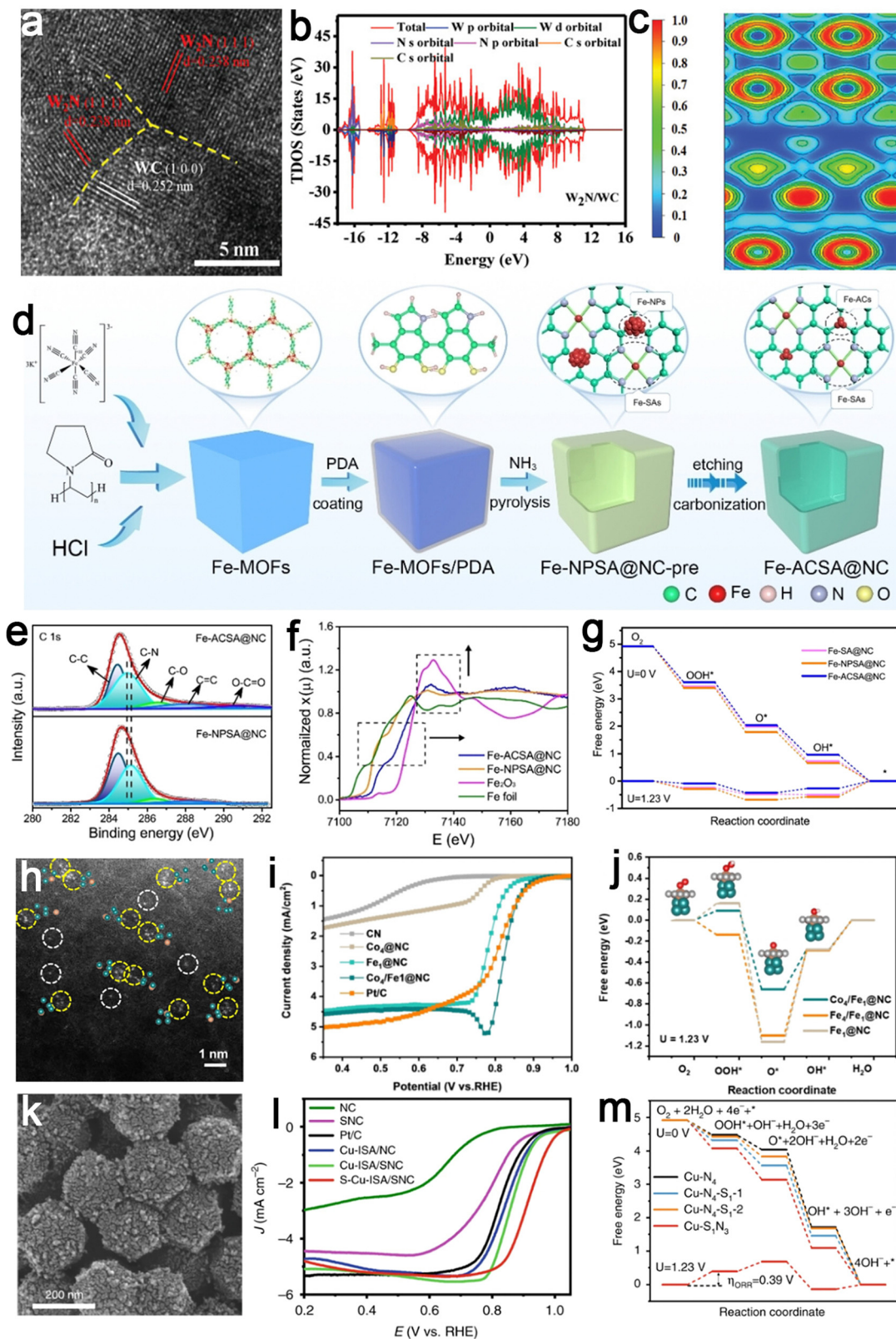
5128 | Chem. Soc. Rev., 2025, **54**, 5108–5145

This journal is © The Royal Society of Chemistry 2025

Fig. 16 Four typical examples of asymmetric coupling catalysts regulated by charge transfer. W$_2$N/WC catalyst: (a) HRTEM image; (b) density of states and (c) electronic local function of the (010) surface of the W$_2$N (111)/WC (100) heterostructure. Reproduced with permission from ref. 195. Copyright 2019, John Wiley and Sons. Fe-ACSA@NC catalyst: (d) synthesis procedure, (e) X-ray photoelectron spectroscopy (XPS) of C 1s, (f) normalized Fe K-edge XANES, and (g) free energy diagrams of the ORR. Reproduced with permission from ref. 172. Copyright 2022, John Wiley and Sons. Co$_4$/Fe$_1$@NC catalyst: (h) HAADF-STEM image with active sites marked, (i) ORR polarization curves, and (j) Gibbs free energy diagrams. Reproduced with permission from ref. 196. Copyright 2023, John Wiley and Sons. S−Cu−ISA/SNC catalyst: (k) SEM image showing the hierarchical morphology, (l) polarization curves for the ORR, and (m) free-energy diagrams for different Cu-centered moieties. Reproduced with permission from ref. 197. Copyright 2020, Springer Nature.

This journal is © The Royal Society of Chemistry 2025

Chem. Soc. Rev., 2025, 54, 5108–5145 | 5129

Specifically, the downward shift of the d-band center of the Fe 3d orbitals in Co_4/Fe_1@NC compared to Fe_1@NC reduced the binding strength of *O, promoting easier desorption and accelerating the ORR process. Additionally, the conversion from O* to OH* was identified as the rate-determining step, where the Co_4/Fe_1@NC system exhibited a smaller free energy change than Fe_4/Fe_1@NC and Fe_1@NC, indicating that Co_4/Fe_1@NC effectively weakened O adsorption, optimizing the ORR pathway (Fig. 16j). Interestingly, a Cu_{SA} ORR catalyst comprised of asymmetric $Cu-S_1N_3$ coordination moieties anchored within a hierarchically porous carbon framework was fabricated through atomic interface engineering.[197] In this configuration, copper is directly coordinated with sulfur and nitrogen atoms, designated as S–Cu-ISA/SNC (Fig. 16k). Due to the rational construction of active sites, the S–Cu-ISA/SNC sample exhibited notable ORR performance in alkaline media (Fig. 16l). Both experimental and theoretical analyses revealed that the introduction of sulfur altered the electronic structure of Cu atoms in the $Cu-S_1N_3$ site, particularly increasing electron occupancy in the $d_{x^2-y^2}$ orbitals. After O* adsorption, the $Cu-S_1N_3$ site exhibited stronger π-bonding contributions, which enhanced the weak binding of ORR intermediates, thus improving the catalytic performance of the Cu center (Fig. 16m). This localized structural regulation strategy shows potential for catalyzing advanced O-containing reactions and other electrochemical processes.

4.2 Strain engineering

Strain effects are induced by altering atom-atom bond lengths or inducing lattice mismatches, resulting in diverse electronic structures and modified adsorption capabilities towards reactants, intermediates, and products.[200–202] This tunability facilitates the ability of the strain-rich electrocatalysts to catalyze the HER, ORR, and OER processes.[203–208] For instance, a heterostructure involving NiFe layered double hydroxides (LDH) and $Co_{1-x}S$ in a sandwich-like configuration was fabricated (Fig. 17a–d). This design showed synergistic catalytic effects from compositionally asymmetric coupling, leading to efficient OER performance.[209] The surface lattice mismatch within NiFe LDH induced substantial strain interfaces in the electrodeposited $Co_{1-x}S$, rearranging local electron structures. This restructuring enhanced charge transfer efficiency and the chemisorption of intermediates containing oxygen (Fig. 17e). In another investigation, a facile hydrothermal method was introduced for synthesizing asymmetric heterostructure nanomaterials involving $Co(OH)_2$ and $Ni(OH)_2$, effectively activating the basal plane of $Co(OH)_2$.[210] The heterogeneous interfaces introduced lattice strains, leading to a downward shift in the d-band center of the Co site within the $Co(OH)_2$ structure. This facilitated the efficient desorption of oxygen during the OER process, accelerating reaction kinetics and improving catalytic activity.

Recently, a host–guest chemical approach was also employed to anchor FePc onto carbon nanotubes incorporating polyoxometalate, successfully fabricating an asymmetrical heterostructure designed for the ORR electrocatalyst ($FePc-\{PW_{12}\}$@nanotube).[211] The result unveiled that polyoxometalate induced localized tensile strain in single-walled nanotubes, strengthening their interaction with FePc (Fig. 17f–h). Thus, the strain and curvature effects stemming from the $\{PW_{12}\}$@nanotube substrate adeptly regulated the geometric

configuration of the $Fe-N_4$ center and the dynamics of local electrons, ultimately enhancing the ORR catalytic performance (Fig. 17i and j). As expected, this heterostructure exhibited exceptional durability, methanol tolerance, and ORR activity in an alkaline environment. Thus, these findings contribute to a comprehensive understanding of the strain-adsorption-activity relationships and offer novel insights into the rational design of multifunctional catalysts tailored for various energy conversion applications.

4.3 Spin-state regulation

The importance of spin states or magnetic moments in catalysis is increasingly evident, especially given the prevalence of active sites on surfaces, edges, or defects where unsaturated bonding can induce local spins and magnetic moments.[212] Transition metals with local magnetic moments can enhance electrocatalytic performances. These phenomena have been observed across various reactions, including the HER, CO_2 reduction, N_2 reduction, and other catalytic processes. However, the most extensively studied reactions involve O_2, specifically the OER and ORR.[213] Transition metal oxides and hydroxides like $Fe_xNi_{1-x}OOH$, FeOOH, and NiOOH are prominent examples that improve their efficacy in the OER process.[214–216] Additionally, intermediates in catalytic reactions may be associated with spin states.[217] For instance, the O_2 molecule exhibits a ground paramagnetic triplet state, while oxygenated compounds and intermediates often assume a singlet state during the OER process.[218] Given the spin selection rule, spin-involved electron transfer plays a crucial role in reaction kinetics, particularly in the presence of the O_2 molecule.[219] Manipulating spin arrangement and magnetic moments is beneficial for reducing energy barriers or overcoming spin suppression, known as spin catalysis, which has been widely recognized in various reactions. Notably, spin-related catalysis has garnered increased attention for influencing adsorption, reactant and intermediate formation, rate-determining steps, electron transfer, and catalytic activity. Hence, catalyst design should prioritize guiding spin-selective regulation to enhance catalytic performance.

For example, a spin state regulation strategy was proposed by introducing axial Fe–O–Ti ligands to enhance the ORR activity of coordinatively asymmetric Fe centers (Fig. 18a and b).[220] Experimental and theoretical calculations indicated that Fe–O–Ti ligands induced a transition of the Fe center from a low-spin to a medium-spin state. This transition facilitated the appropriate filling of the e_g orbitals of the Fe center, optimizing the O_2 adsorption energy, which promoted the activation of oxygen molecules and enhanced the ORR activity (Fig. 18c–e). An asymmetric structure of Fe–Mn/NC bimetal SACs was also recently investigated.[221] The proximity of atomically dispersed Mn–N sites effectively activated Fe^{III} centers within the FeN_4 moiety, leading to single-electron filling ($t_{2g}^4e_g^1$) and promoting electron transfer into the antibonding orbitals of oxygen (Fig. 18f–i). Both magnetization measurements and theoretical calculations revealed that these adjacent Mn–N species induced spin-state transitions and modulated the electronic structure of Fe^{III}, resulting in ORR activity and stability under both alkaline and acidic conditions. Furthermore, when O_2 was adsorbed by

5130 | *Chem. Soc. Rev.*, 2025, **54**, 5108–5145

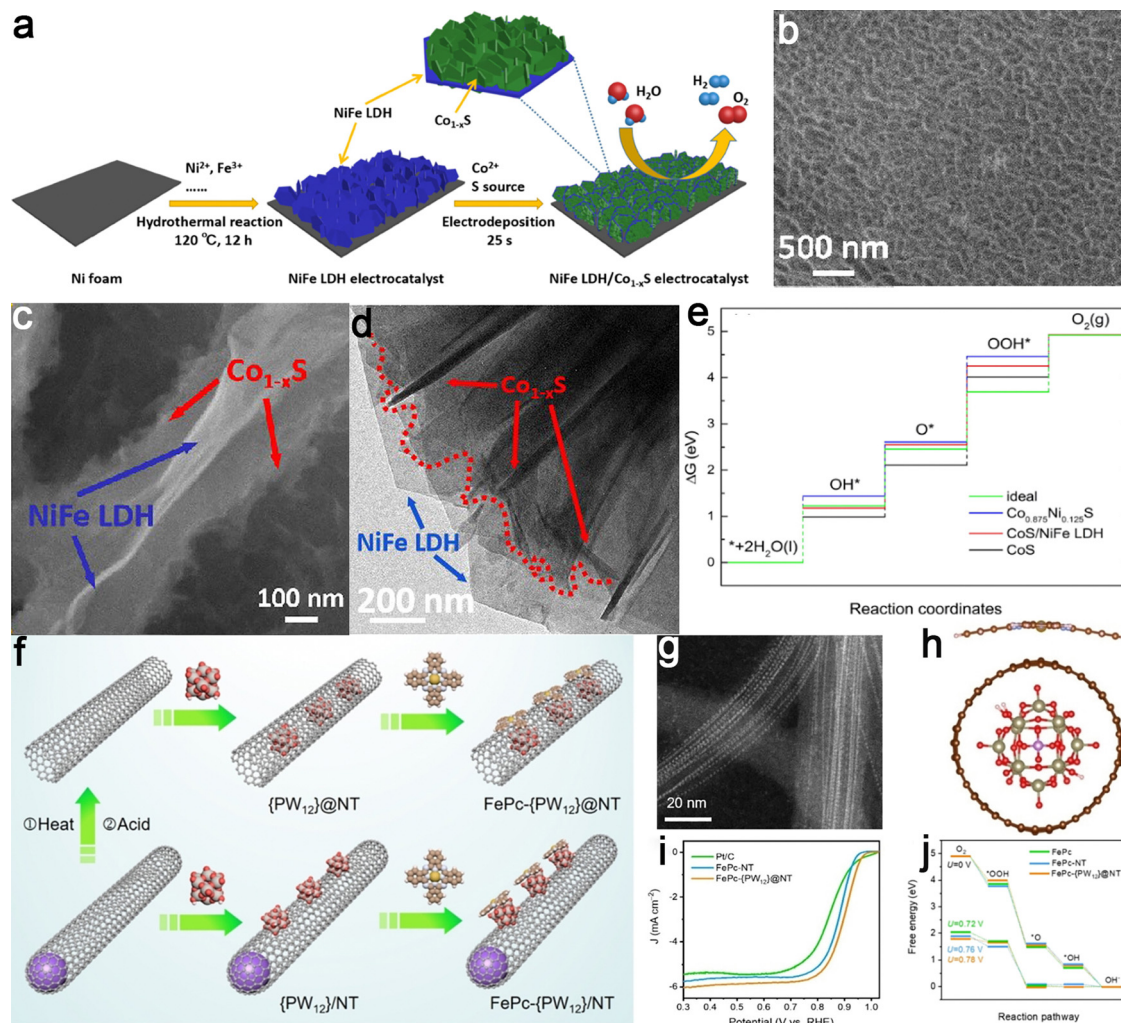This journal is © The Royal Society of Chemistry 2025

Fig. 17 Examples of asymmetric coupling catalysts regulated by strain engineering. NiFe LDH/Co$_{1-x}$S catalyst: (a) schematic representation of the synthesis procedure, (b and c) SEM images depicting the morphology, (d) TEM image showing the interface between NiFe LDH and Co$_{1-x}$S, and (e) free energy diagrams comparing the catalytic pathways for different active sites. Reproduced with permission from ref. 209. Copyright 2020, Elsevier. FePc–{PW$_{12}$}@nanotube catalyst: (f) schematic illustration of the preparation steps, (g) HAADF-STEM image revealing structural details, and (h) the structure of the nanohybrids; (i) ORR polarization curves of various catalysts and (j) free energy diagrams of ORR pathways. Reproduced with permission from ref. 211. Copyright 2023, John Wiley and Sons.

Fe/Mn atom pairs, the optimized bond lengths and binding energies reduced the dissociation energy barrier. This configuration facilitated the capture of oxygen-containing intermediates and rapidly cleaved M–OH bonds, ensuring the regeneration of *O and *OH. As a result, it accelerated ORR kinetics by suppressing the formation of peroxides.

In another work, the incorporation of single Cu atoms onto Fe–N–C aerogels in asymmetrically assembled binuclear sites resulted in reduced magnetic moments and enhanced ORR activity of the Fe center within a broad pH range of 0 to 14.[222] Specifically, Fe atoms located at the nanopore edges contributed more electron density compared to those on the basal plane, thereby increasing their catalytic activity. Additionally, in the Cu$_1$/Fe$_1$-2 system, the electronic states of the Cu atoms were close to the Fermi level, providing more active electrons and promoting the reduction reaction. Through redistribution of electron density, the d$_{z^2}$ orbital electron density of Fe increased, reducing its magnetic moment and further optimizing the ORR

reaction pathway, particularly by weakening the adsorption strength of *O and lowering the reaction energy barrier. It was also observed that the spin state of single atomic tungsten induced spin delocalization in the heterogeneous W-NiS$_{0.5}$Se$_{0.5}$ structure, resulting in the spin-state delocalization of Ni.[223] This effect increased the electron density in Ni d-orbitals, effectively facilitating the Heyrovsky step and promoting the formation of *OOH intermediates during the OER process, thereby enhancing the overall catalytic performance of NiS$_{0.5}$Se$_{0.5}$. Specifically, at the Ni active sites, *OH was initially generated, followed by its conversion into *OOH, which was subsequently released as O$_2$ through a proton-coupled electron transfer process. The incorporation of single-atomic W accelerated this reaction sequence, markedly improving OER kinetics.

4.4 Tandem catalytic effect

Electrocatalytic reactions often include a series of reaction steps and intermediates. However, the linear scaling relationships that
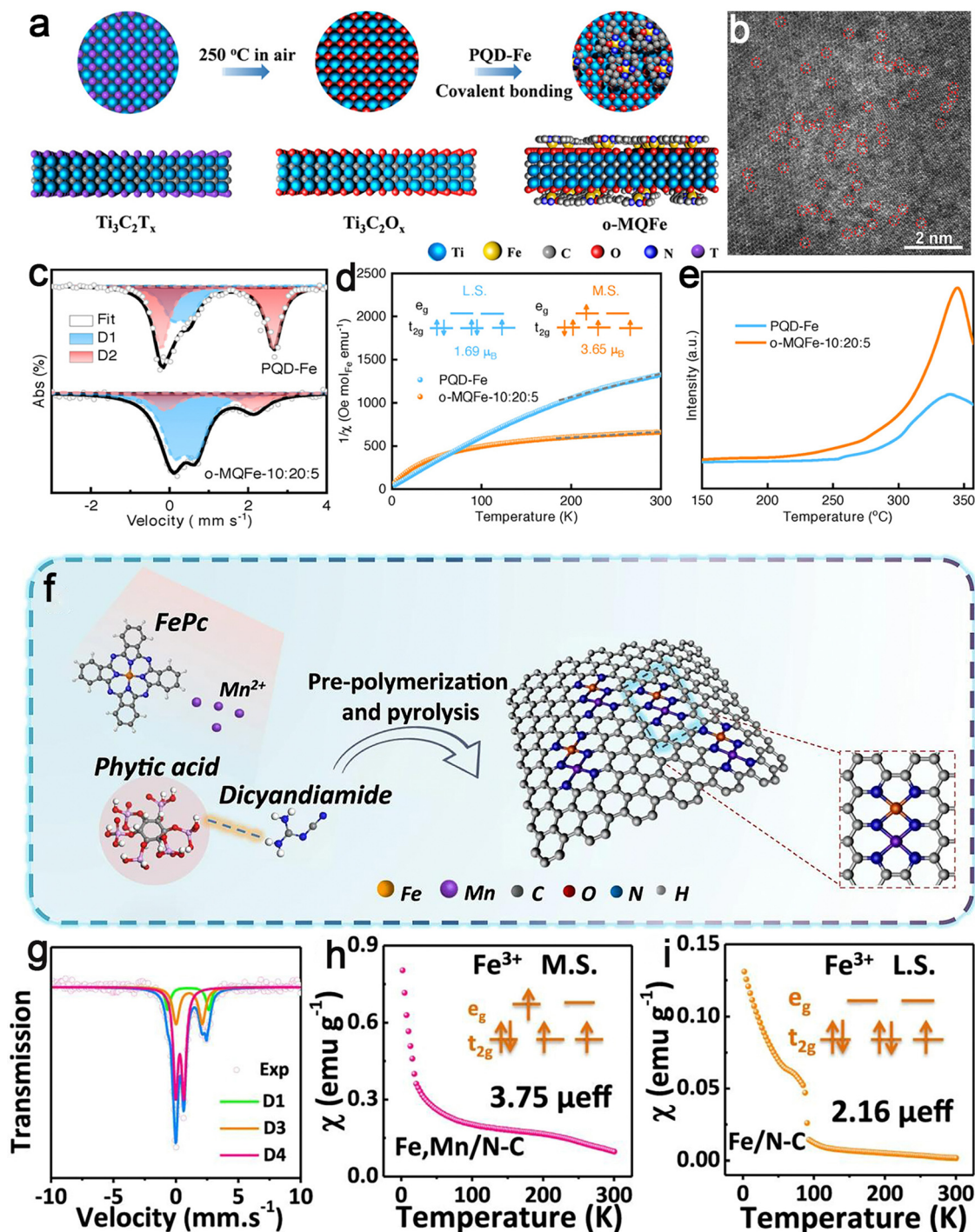
This journal is © The Royal Society of Chemistry 2025

Chem. Soc. Rev., 2025, 54, 5108–5145 | 5131

Fig. 18 Examples of asymmetric coupling catalysts regulated by spin-state. O-MQFe catalyst: (a) schematic of the synthesis process and (b) HRTEM image showing active sites; (c) ^{57}Fe Mössbauer spectroscopy highlighting spin states, (d) $1/\chi_m$ plots revealing spin configurations, and (e) O_2-temperature-programmed desorption curves. Reproduced with permission from ref. 220. Copyright 2022, John Wiley and Sons. Fe–Mn/NC catalyst: (f) synthesis procedure, (g) room-temperature ^{57}Fe Mössbauer spectrum showing distinct components; (h) magnetic susceptibility of Fe–Mn/NC indicating high-spin Fe^{3+} states with $\mu_{eff} = 3.75\mu_B$; and (i) low-spin states in Fe/N–C with $\mu_{eff} = 2.16\mu_B$. Reproduced with permission from ref. 221. Copyright 2021, Springer Nature.

govern adsorption energy between intermediates present a difficulty in independently regulating adsorption energy for specific steps, particularly for single-type sites, thus hindering the achievement of optimal catalytic effects.[224] Conversely, introducing

asymmetrically coupled multi-active sites is expected to facilitate the independent optimization of the conversion of specific reaction intermediates. This structural arrangement reduces the overall reaction process through a synergistic catalytic effect. Tandem

5132 | Chem. Soc. Rev., 2025, **54**, 5108–5145

This journal is © The Royal Society of Chemistry 2025

catalysis involves a continuous process in which reaction intermediates undergo conversion at one active site, followed by diffusion to another nearby active site, initiating subsequent reactions and collaboratively completing the entire catalytic process.[60] Therefore, the tandem catalytic effect has the potential to expedite the whole reaction by sequentially cascading multiple reaction steps across various active sites. The elastic structure of asymmetrically coupled catalysts facilitates the development of tandem catalysis tailored for complex electrocatalytic reactions.[225]

For example, an efficient electrocatalyst with asymmetrically coupled dual active sites containing Fe–NiOOH and NiC$_4$ single atoms (Ni-SAs/Fe–NiOOH) was prepared (Fig. 19a–c).[226] Experimental results and DFT calculations indicated that the collaborative action of NiC$_4$-SAs and Fe–NiOOH dual active sites endowed the Ni-SAs/Fe–NiOOH catalyst with outstanding OER activity (Fig. 19d–f). Further investigations revealed that the initial formation of *OH and *O occurs on Fe–NiOOH, followed by the migration of *O to Ni–C$_4$ SAs, leading to the subsequent formation of *OOH and O$_2$. In the tandem catalytic

mechanism, the potential-determining step from *OH to *O on Fe–NiOOH (Fe) required a potential of 0.110 V. In contrast, the potential-determining step from *O to *OOH on Ni–C$_4$ SAs necessitated a potential of 0.150 V. Consequently, the tandem catalysis between the two active sites efficiently optimized the potential-determining steps, substantially lowering the electrocatalytic overpotential for the OER process. This study provides fundamental insights into the rational design of OER catalysts and underscores the advantages of asymmetrically coupled active sites in enhancing catalytic performance. Following these findings, an innovative catalyst named Fe, Cu/N–C, featuring the asymmetric coupling of atomically dispersed Fe and Cu, was reported recently (Fig. 19g–i).[227] Using the advantages of electron spin-state regulation and tandem catalysis mechanisms, the ORR activity of the resulting catalyst was improved. Theoretical calculations and detailed analysis revealed that the transformation of O$_2$ molecules into *OOH and *O intermediates primarily occurred at the Fe center within the Fe, Cu/N–C catalyst due to the more favorable reaction barriers at the Fe
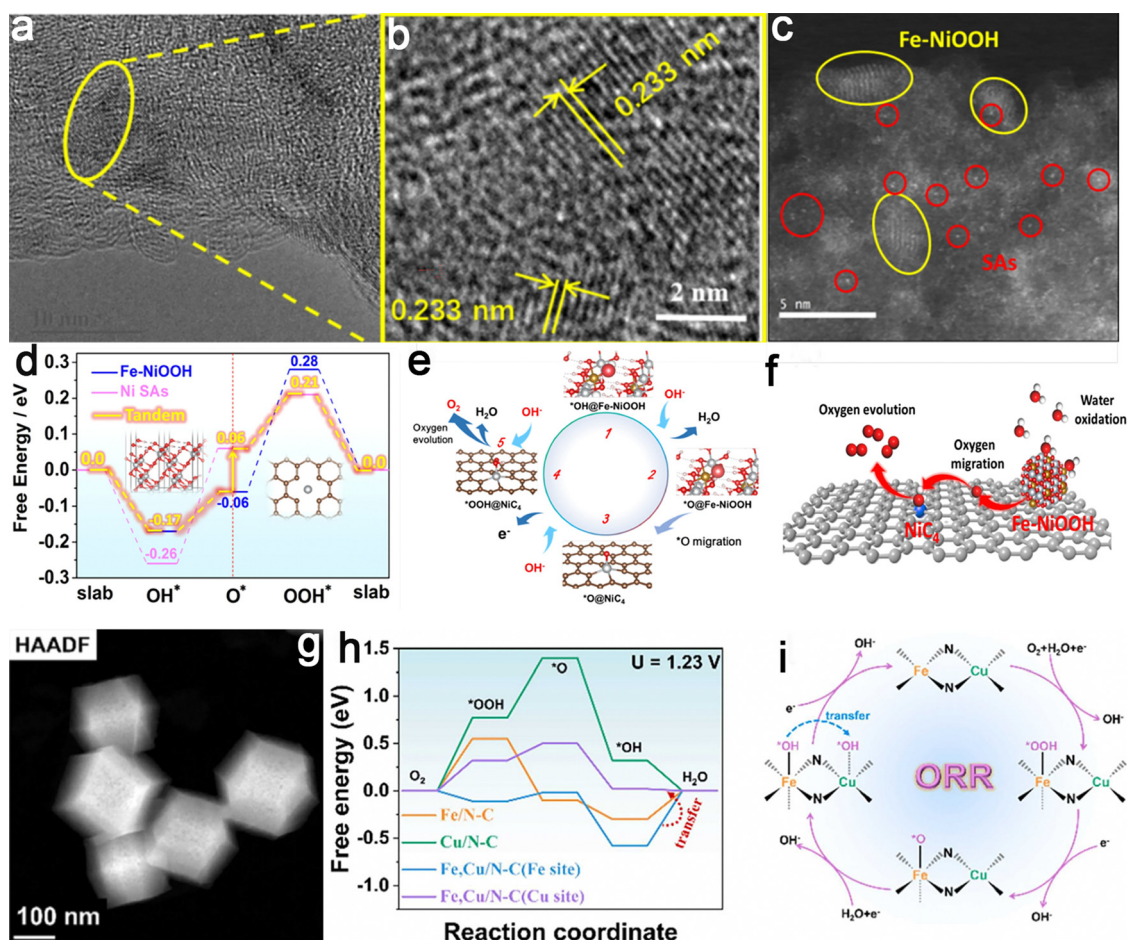

Fig. 19 Examples of asymmetric coupling catalysts regulated by the tandem catalytic effect. Ni–SAs/Fe–NiOOH catalyst: (a and b) HRTEM and (c) HAADF-STEM images showing the structural features and active sites; (d) reaction-free energies illustrating the catalytic pathway for Ni–C$_4$ SAs and Fe–NiOOH; (e) tandem catalysis mechanism depicting the interaction of Ni SAs and Fe–NiOOH during the OER; and (f) schematic diagram of the OER highlighting oxygen migration as a key step. Reproduced with permission from ref. 226. Copyright 2021, Elsevier. Fe, Cu/N–C catalyst: (g) HAADF-STEM image displaying the catalyst morphology; (h) ORR free energy diagrams for Fe and Cu active sites; and (i) schematic illustrating the tandem reaction mechanism for ORR on Fe, Cu/N–C. Reproduced with permission from ref. 227. Copyright 2023, Elsevier.

This journal is © The Royal Society of Chemistry 2025

Chem. Soc. Rev., 2025, **54**, 5108–5145 | **5133**

sites in the initial two steps compared to those at the Cu sites. Next, owing to the reduced barrier of the Cu site, *OH species generated in the third step systematically migrated from the Fe domain to the Cu region, following an expected tandem catalysis pathway. The stepwise procedure rapidly hastened the breakdown of the metal–OH linkage. As a result, the simultaneous presence of dual active sites within Fe, Cu/ N–C overcame the limitations of the negative scaling relation-ship in O_2 reduction. This contribution paves an intriguing path for overcoming the scale-related constraints of multi-stage reactions and unveils an avenue for developing advanced catalysts.

4.5 Vacancy defect regulation

Incorporating diverse defects spanning multiple dimensions has been employed to create highly active sites driven by the unordered atomic arrangement, distinct electron distribution, and energy fluctuations.[228] These voids can be classified into three types based on the charge polarity of initially existing ions: anionic, cationic, and mixed voids.[229] Due to the greater atomic mass and stronger chemical bonding of cations, form-ing cationic voids requires highly aggressive physical bombard-ment or chemical etching treatment, posing challenges in obtaining high-purity mono-typic voids.[230] Conversely, con-structing a series of anionic voids is more feasible and pre-valent due to the generally lighter atomic mass and looser coordination structure of anions. Among these, voids involving O, C, and S are the most adopted group of anionic voids.[231]

As a typical practice, a CoP@CoOOH/CP electrocatalyst was synthesized in situ on carbon paper (CP) through a hydrother-mal process followed by phosphorization and oxidation (Fig. 20a).[232] The CoOOH shell, rich in oxygen vacancies, could actively modulate surface–oxygen interactions, thereby expos-ing more active sites and reducing the energy barrier for the rate-determining step. This structural optimization enhanced OER activity and accelerated O_2 evolution (Fig. 20b–d). The introduction of oxygen vacancies facilitated an increase in the concentration of Co^{3+} species with lower coordination num-bers, further boosting the catalytic activity for the OER. As an illustrative example, a defect engineering strategy was devel-oped to introduce carbon vacancies near Fe–N$_4$ (Fe–N$_4$V$_C$), disrupting the localized electronic structural symmetry of Fe–N$_4$ (Fig. 20e).[233] This enhanced the intrinsic activity of Fe–N$_4$ and reduced the reaction energy barrier (Fig. 20f–g). Similarly, a universal sub-nanoreactor strategy was designed to synthesize a yolk–shell nanostructure characterized by a distinctive asym-metric coupling of MoS_2 support and metal SA sites (Fig. 20h).[234] Co SA was coordinated with C and Mo atoms in this catalytic system, establishing a dual-anchored coordination microenvironment in the C–Co–MoS_2 composite (Fig. 20i–k). These findings (Fig. 20l) indicated that the optimized C–Co–MoS_2 exhibited the lowest overpotential (η_{10} = 0.017 V) for the HER. DFT calculations demonstrated that metal SAs could stabilize the dual carrier system with the effective electron lock at sulfur vacancies and induce tunable electron transfer at the C–M–Mo interface. The presence of sulfur vacancies and intercalated carbon, serving as dual carriers, facilitated the formation of electron lock and directed electron transfer chan-nel, promoting the stabilization and activation of metal SAs. Therefore, this research strategy provides a new perspective for designing efficient electrocatalysts.

4.6 Oxophilicity regulation

Previous investigations have underscored the pivotal role played by the adsorption strength of reactants and intermedi-ates in the catalyst surface in determining catalytic activity. The recent focus on regulating oxygen affinity has proven advanta-geous in optimizing the adsorption configuration of intermedi-ates and accelerating the kinetics of chemical reactions.[235] As an illustration, an efficient three-dimensional nanostructured comprising Cr-doped Ni nanohelixes was fabricated. Notably, incorporating oxygen-affinitive chromium disrupted the struc-tural symmetry, optimizing the H and OH binding energies on nickel nanohelixes.[236] This alteration accelerated the processes of water dissociation and adsorption, consequently enhancing the overall kinetics of the HER (Fig. 21a and b). By introducing the element Sn, which is characterized by lower oxygen affinity and weaker hydrogen adsorption capability compared to Ni, an asymmetric Ni$_3$Sn$_2$–NiSnO$_x$ nanocomposite was prepared (Fig. 21c).[237] The optimized Ni$_3$Sn$_2$–NiSnO$_x$ composite exhib-ited overpotentials of 0.014 and 0.165 V at 10 and 1000 mA cm^{-2} in 1 M KOH, respectively, along with long-term stability. Computational analyses indicated that the intermetallic com-pound Ni$_3$Sn$_2$ component exhibited appropriate hydrogen binding energy and low OH adsorption capacity, while the NiSnO$_x$ component facilitated the water dissociation and OH transfer processes (Fig. 21d and e). The interaction between these components resulted in effective dissociation adsorption of water, facile OH detachment, and hydrogen bond formation, enhancing the HER kinetics. In another work, asymmetrically coupled Co SAs and Co nanoparticles into N-doped carbon nanotubes were developed (Co@NCNT/Co-SA@NCMT, Fig. 21f–h).[238] Experimental and theoretical calculations indi-cated that Co SAs could catalyze oxygen reduction to H_2O_2, while the oxygen-affine Co nanoparticles exhibited enhanced efficiency in further reducing it to H_2O (Fig. 21i–k). Thus, regulating oxygen affinity emerges as a feasible approach to boost activity and stability, paving the way for developing advanced hydrogen/oxygen electrocatalysts.

5. Conclusions and perspectives

5.1 Conclusions

The urgent demand for green, low-carbon, and highly efficient energy conversion technologies highlights the necessity for low-cost, high-efficiency energy conversion materials. This review systematically categorizes and summarizes the component and structural characteristics of ATEs. Additionally, it provides a detailed analysis of their electrocatalytic activity regulation mechanisms in the ORR, OER, and HER, including charge transfer, strain engineering, spin-state regulation, tandem

5134 | Chem. Soc. Rev., 2025, 54, 5108–5145
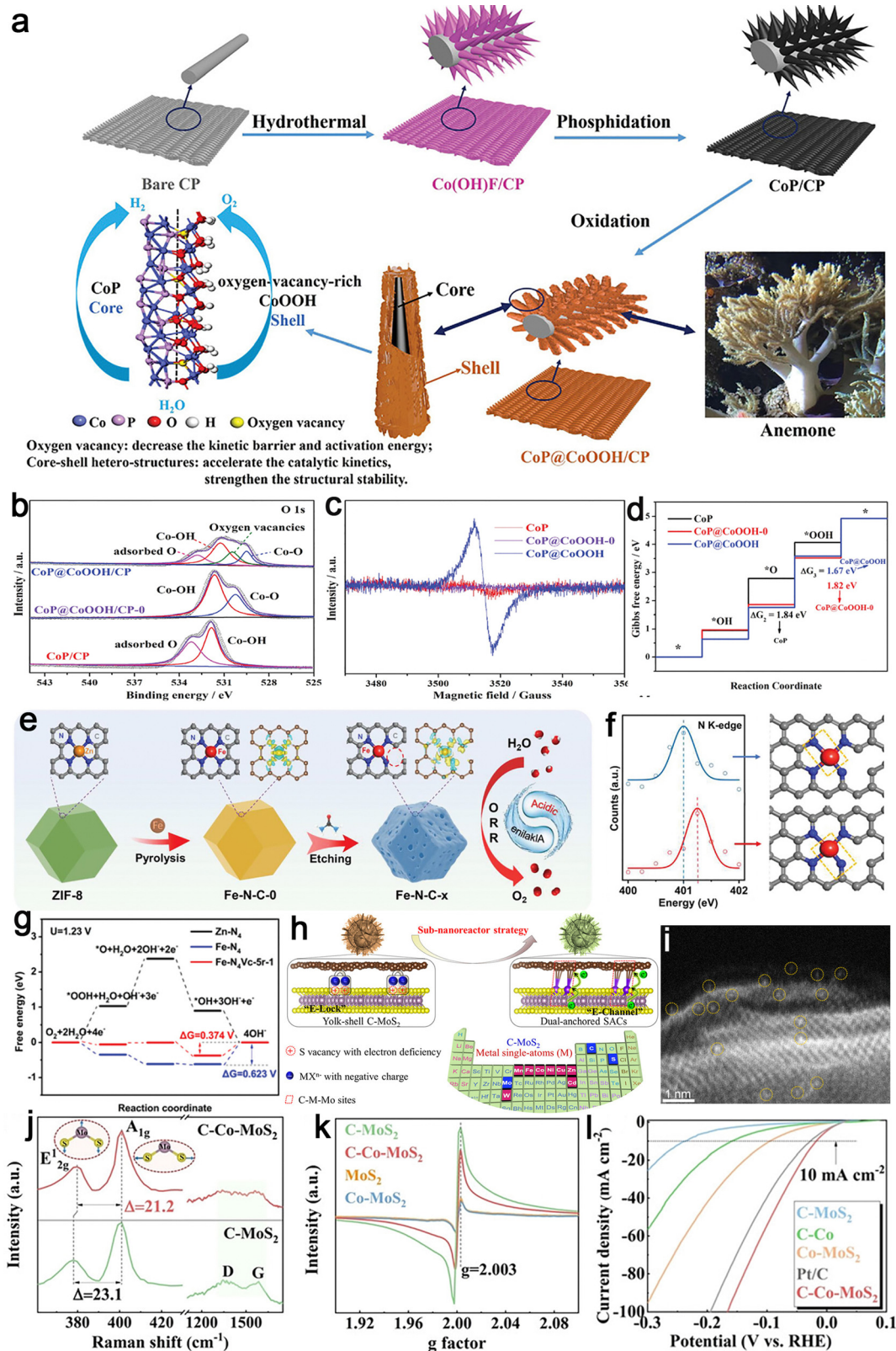
This journal is © The Royal Society of Chemistry 2025

Fig. 20 Examples of asymmetric coupling catalysts regulated by vacancy defects. CoP@CoOOH/CP catalyst: (a) schematic of the synthesis strategy involving core−shell design with oxygen vacancies, (b) O 1s XPS spectra showing oxygen-related surface states, and (c) electron paramagnetic resonance (EPR) spectra highlighting electronic structure changes; (d) mechanism diagram of OER catalysis facilitated by oxygen vacancies. Reproduced with permission from ref. 232. Copyright 2022, John Wiley and Sons. Fe−N_4V_C catalyst: (e) schematic of the synthesis route for generating vacancy-enriched Fe−N−C structures and (f) the N peak analysis of Fe−N−C-2 in EELS and its corresponding FeN bond; (g) ORR free energy diagrams. Reproduced with permission from ref. 233. Copyright 2023, John Wiley and Sons. C−Co−MoS_2 catalyst: (h) illustration for the sub-nanoreactor synthesis strategy; (i) TEM image, (j) Raman profiles, (k) EPR data, and (l) HER polarization curves of various catalysts. Reproduced with permission from ref. 234. Copyright 2023, John Wiley and Sons.
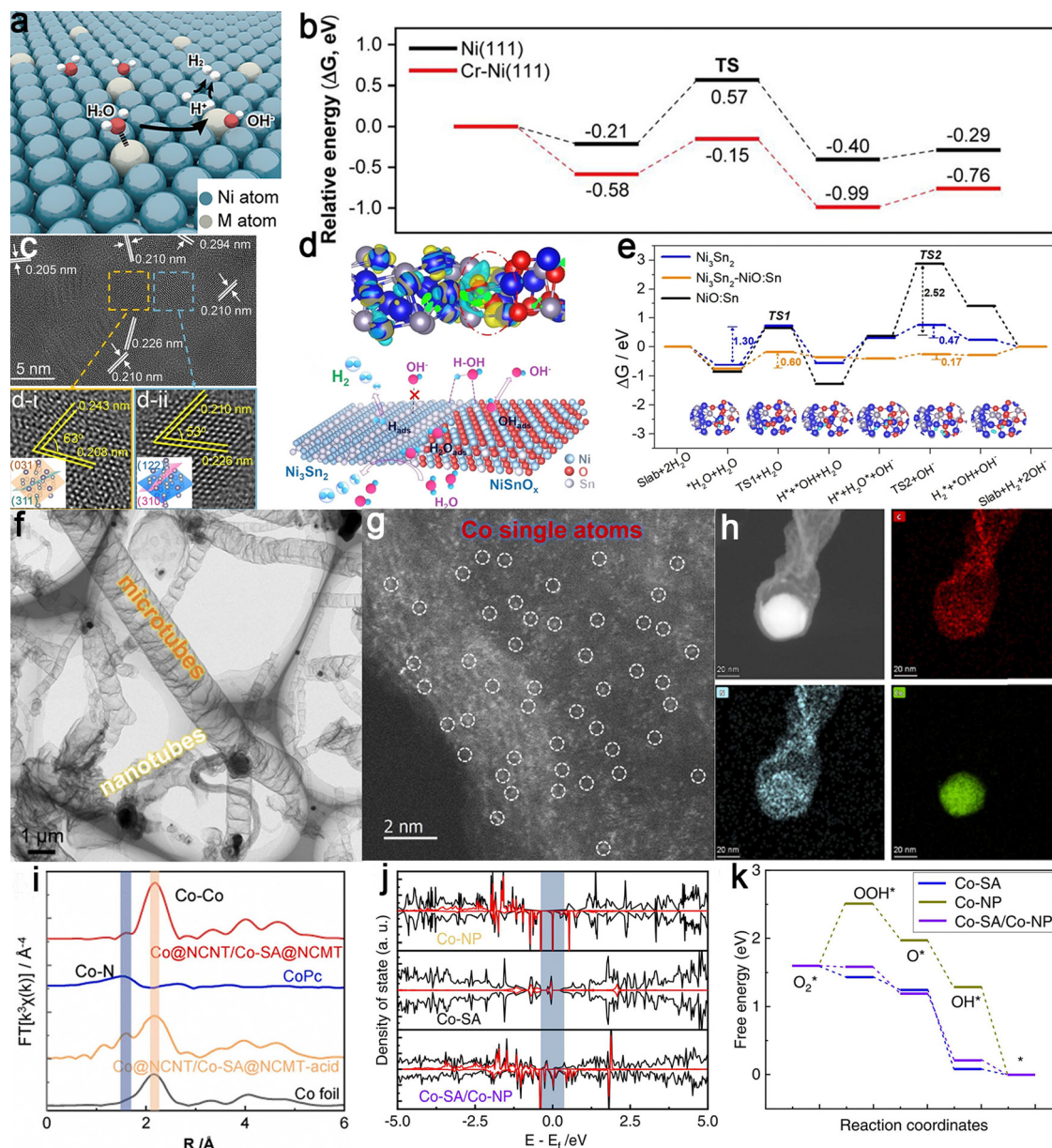
Fig. 21 Examples of asymmetric coupling catalysts regulated by oxophilicity. Cr-doped Ni nanohelix catalyst: (a) Schematic illustration showing reaction paths in alkaline HER; (b) theoretical calculation of the HER energy profile on Ni (111) and Cr–Ni (111). Reproduced with permission from ref. 236. Copyright 2021, American Chemical Society. Ni_3Sn_2–$NiSnO_x$ nanocomposite catalyst: (c) HRTEM images highlighting structural features, (d) charge density difference visualizing electron interactions, and (e) energy profiles for alkaline HER showing the role of oxophilic sites. Reproduced with permission from ref. 237. Copyright 2023, John Wiley and Sons. Co@NCNT/Co-SA@NCMT catalyst: (f) TEM image illustrating the hierarchical structure, (g) HAADF-STEM image showing Co single atoms; (h) energy dispersive X-ray spectroscopy (EDS) mapping demonstrating elemental distributions; (i) EXAFS spectra revealing Co coordination environments; (j) density of state showing electronic interactions; and (k) free energy diagrams of the OER for different catalysts. Reproduced with permission from ref. 238. Copyright 2022, Elsevier.

catalytic effects, vacancy defect modulation, and oxophilicity regulation. Design principles, unique advantages, and drawbacks are depicted to deepen the understanding of related modulation methods (Fig. 22). Although current asymmetric coupling designs have exhibited considerable advantages and reached considerable milestones, this review acknowledges the remaining challenges. Addressing these challenges requires the integration of advanced synthesis methods, operando probes,

and machine learning-driven approaches to accelerate the development of next-generation electrocatalysts.

5.2 Challenges and perspectives

5.2.1 Developing a precise synthesis method. ATEs have gained widespread attention for their ability to boost catalytic performance. The component design, achieved through selecting various elements or compounds, allows for the construction
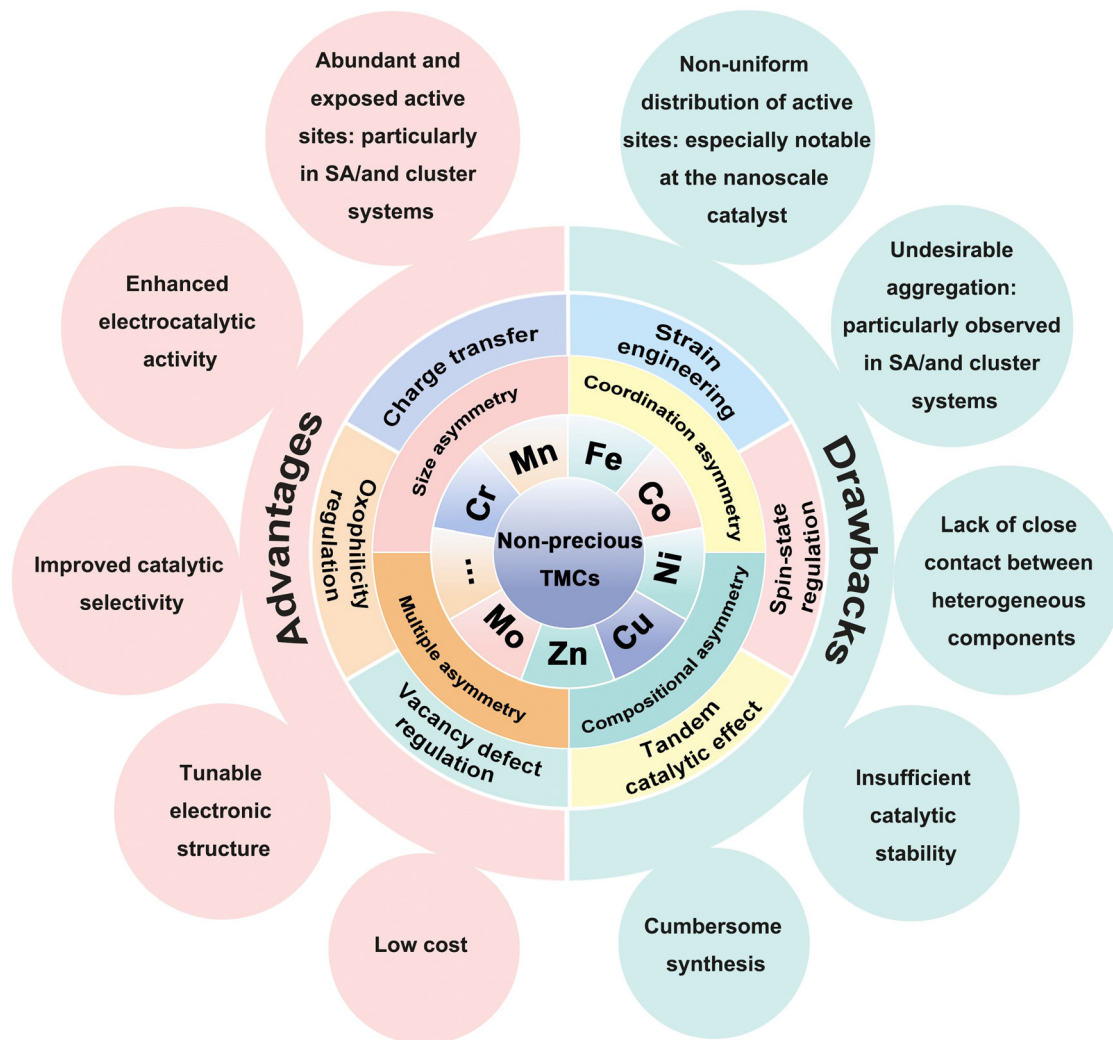
5136 | Chem. Soc. Rev., 2025, 54, 5108–5145

This journal is © The Royal Society of Chemistry 2025

Fig. 22 The advantages and drawbacks of asymmetrically tailored non-precious TMCs for hydrogen and oxygen electrocatalysis. This schematic summarizes the benefits and limitations of using asymmetrically engineered TMCs. Key advantages include enhanced electrocatalytic activity, improved selectivity, tunable electronic structure, abundant active sites, and low cost. However, challenges persist, such as non-uniform active site distribution, undesirable aggregation, lack of close contact between heterogeneous components, insufficient stability, and cumbersome synthesis processes. These insights highlight both the opportunities and hurdles in advancing TMC-based electrocatalysis.

of heterogeneous catalytic units. The size-based asymmetric design focuses on differences in the nanostructure size of the active site within the catalyst, influencing reaction rates and selectivity. Additionally, asymmetric coordination design optimizes catalytic performance by adjusting the surface coordination structure. The interaction of these multilevel asymmetries offers innovative directions for efficient and controllable catalytic reactions. However, achieving univariate control over these factors in practical applications remains challenging (Fig. 23).

(i) When investigating coordination asymmetry using M–N$_4$ and M–N$_3$P$_1$ models, achieving consistency in the number of metal center atoms between the two material models poses a challenge in experimental synthesis. Beyond that, ensuring that each metal atom is precisely coordinated with only one heteroatom presents a considerable obstacle.[239,240]

(ii) Exploring the mechanism of size asymmetry based on M$_{AC}$–M$_{SA}$, precise control of the same metal center density

across different samples is challenging.[171] Moreover, ensuring that each atom is exclusively coupled with adjacent clusters, thereby achieving a 100% formation of size-asymmetric active sites within the material structure, remains a hurdle.

(iii) In exploring multiple asymmetric strategies, the complex catalyst structures pose challenges in elucidating specific catalytic mechanisms. The accurate assessment of the distinct contributions of various effects to the activity and stability of the catalysts becomes difficult. The improved catalytic activity is often attributed to the synergistic catalysis effects, leaving the actual catalytic mechanism unclear. These challenges reflect technological limitations in achieving univariate control over components, size, and coordination, thus requiring the development of more sophisticated experimental techniques and novel design strategies to better understand and regulate the inherent catalytic mechanism in ATEs. Overcoming these obstacles will broaden the research landscape for
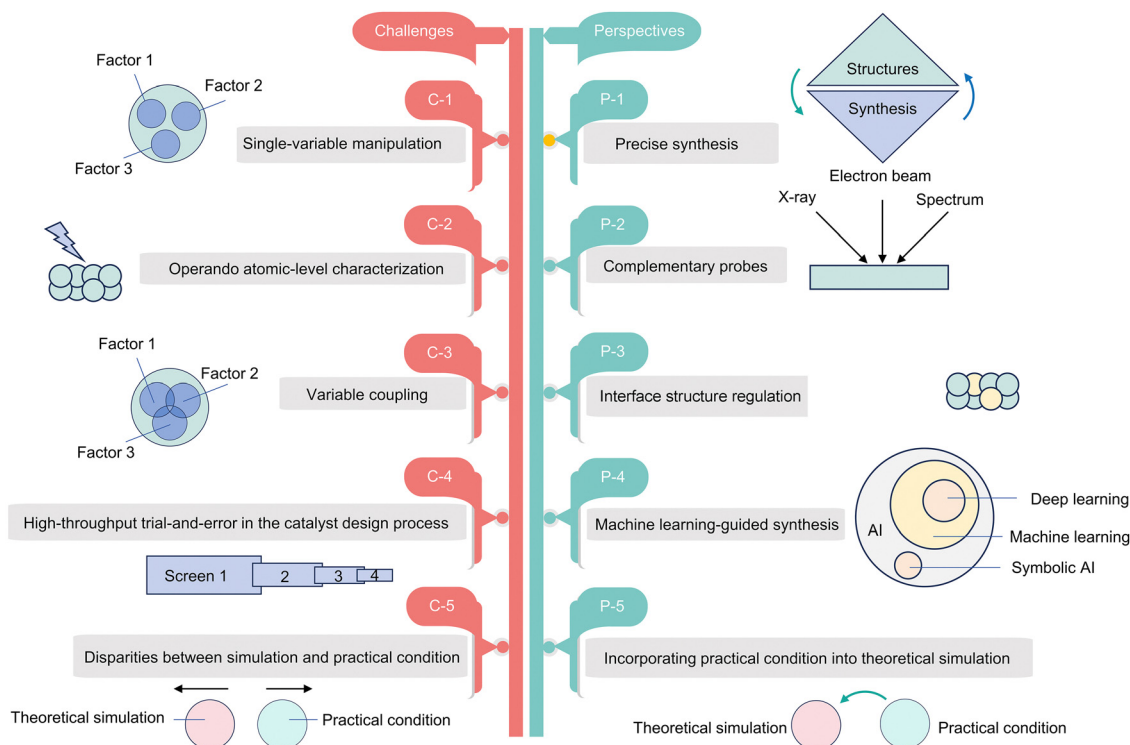
This journal is © The Royal Society of Chemistry 2025

Chem. Soc. Rev., 2025, **54**, 5108–5145 | **5137**

Fig. 23 Challenges and future strategies in the development of ATEs. This illustration outlines the key challenges (C-1 to C-5) and corresponding perspectives (P-1 to P-5) for advancing ATEs. Challenges include the complexity of single-variable manipulation (C-1), the need for operando atomic-level characterization (C-2), variability in coupling effects (C-3), reliance on high-throughput trial-and-error methods (C-4), and the gap between theoretical simulations and practical conditions (C-5). Suggested strategies involve precise synthesis (P-1), integrating complementary probes (P-2), regulating interface structures (P-3), leveraging machine learning-guided synthesis (P-4), and incorporating practical conditions into theoretical simulations (P-5). These strategies aim to drive innovation in catalyst design, efficiency, and sustainability.

the future development of asymmetric catalysis, propelling the field toward more excellent controllability and efficiency.

5.2.2 Advanced structural probing. In structure characterization, contemporary measurement technologies encounter challenges in providing direct and high-resolution experimental evidence (Fig. 23).

(i) Incorporating heteroatoms into the axial positions of metal centers within the M–N$_4$ structure illustrates the potential to achieve axially asymmetric catalytic configurations.[241] However, accurately verifying whether ligands bridge each axial position of the metal center presents a hurdle in characterizing electrocatalyst structures, necessitating the advancement of sophisticated and high-resolution instruments.

(ii) Exploring the correlations between strain, defects, oxygen affinity, and performance encounters challenges due to the absence of quantitative assessments. To overcome this, it is crucial to explore more precise research methods to enhance our comprehension of the practical impact of these factors on catalytic activity.

(iii) The investigation of charge-directed transfer phenomena underscores the necessity for advanced imaging techniques to visualize charge distribution. The conventional characterization methods include X-ray photoelectron spectroscopy, ultraviolet photoelectron spectroscopy, and theoretical modeling.[242] Similarly, Mössbauer spectroscopy, magnetic susceptibility analysis,

and theoretical calculations are predominant in elucidating spin regulation mechanisms.[243] However, the absence of solid experimental evidence makes the proposed catalytic mechanisms less convincing.

(iv) Observing the dynamic changes in asymmetric structures during the catalytic process necessitates advanced *in situ* characterization techniques. This involves overcoming both the inherent challenges of conventional asymmetric structure characterization and the additional complexities posed by *in situ* experimental systems, including the introduction of gases, voltage variations, and catalyst structure evolution. Therefore, we suggest intensified cutting-edge research in this domain, especially on advancing instrument technology.[244]

5.2.3 Focusing on interface structure regulation. ATEs, characterized by construction through the efficient coupling of diverse constituent units, exhibit distinctive structural asymmetry. Within this domain, a particular emphasis should be placed on interfacial compositions and structures, especially regarding close connections at the interface. These connections are pivotal in facilitating rapid charge transfer, directly affecting electrocatalytic activity (Fig. 23). Employing suitable building blocks with diverse elements to create cohesive and tight interfaces is recommended to overcome this challenge. Additionally, surface modification or functionalization emerges as another critical strategy. Interface connections are strengthened by introducing

5138 | *Chem. Soc. Rev.*, 2025, **54**, 5108–5145

This journal is © The Royal Society of Chemistry 2025

functional groups at the interface, thereby contributing to more intimate interactions within the heterogeneous structure.[245] This strategic approach elevates the overall stability of catalysts and ensures more strict connections at the interface, paving the way for the enhancement of catalytic activity. However, achieving the goal of developing efficient catalytic interfaces still requires further attention, despite the potential of these methods.

5.2.4 Machine learning-guided synthesis. Despite the potential of ATEs in H_2/O_2 electrocatalysis, much of the current research relies on high-throughput trial-and-error synthesis (Fig. 23). These methods often involve intuitive adjustments by researchers to tune experimental parameters, resulting in inefficiencies and challenges in achieving high-efficiency catalyst preparation. Moreover, reported synthetic methods are typically limited to generating small quantities of catalysts under controlled laboratory conditions, thus requiring scalable production to meet practical demands. The restricted variety of reported ATEs suggests exploring novel synthetic strategies to develop new ATEs and expand their catalytic genomic library. As a strategic solution, machine learning (ML) acquires knowledge from data, facilitating rapid predictions of target properties. Addressing these challenges involves utilizing ML before structural design to provide more practical guidance for catalyst preparation. However, narrowing the gap between theoretical models and actual structures is imperative, as it contributes to the precise and thorough comprehension of the enhancing mechanisms for catalytic performance.[246]

5.2.5 Incorporating practical conditions into theoretical simulations. Current DFT calculations research often simplifies catalyst structures excessively, potentially leading to deviations from real catalytic systems due to the limited computational scale of first-principles calculations and the use of simplified models. Crucial factors affecting catalyst activity, such as applied electric fields, electrolytes, and the dynamic evolution of active sites on the surface, are frequently overlooked in simulations (Fig. 23).[247,248] Integrating environmental factors inherent in actual electrocatalytic processes before conducting DFT calculations or molecular dynamics (MD) simulations is crucial to address this limitation.[246] Optimized DFT calculations or MD simulations are necessary to accurately capture the influencing factors during electrocatalysis. This approach enhances computational reliability, accurately portraying electrocatalyst properties and behaviors under real experimental conditions. Therefore, considering environmental factors during DFT or MD calculations is vital for understanding catalytic mechanisms. This perspective emphasizes the importance of thoroughly exploring environmental influences in electrocatalytic research, offering valuable insights for future theoretical calculations and catalyst synthesis.

Author contributions

The manuscript was written with contributions from all authors, who have all approved the final version.

Data availability

No primary research results, software, or code have been included and no new data were generated or analyzed as part of this review.

Conflicts of interest

The authors declare no conflict of interest.

Acknowledgements

References

1 S. Chu and A. Majumdar, *Nature*, 2012, **488**, 294–303.

2 Z. G. Yang, J. L. Zhang, M. C. W. Kintner-Meyer, X. C. Lu, D. Choi, J. P. Lemmon and J. Liu, *Chem. Rev.*, 2011, **111**, 3577–3613.

3 W. J. Li, S. Ghosh, N. Liu and B. Poudel, *Joule*, 2024, **8**, 1274–1311.

4 S. Li, C. H. Zhou, J. S. Hu, A. J. Duan, C. M. Xu and X. L. Wang, *J. Catal.*, 2023, **426**, 153–161.

5 K. Liu, H. M. Li, M. H. Xie, P. F. Wang, Z. Y. Jin, Y. T. Liu, M. Zhou, P. P. Li and G. H. Yu, *J. Am. Chem. Soc.*, 2024, **146**, 7779–7790.

6 H. Y. Shi, L. Zhang, X. H. Huang, Q. Q. Kong, A. Abdukayum, Y. T. Zhou, G. Y. Cheng, S. S. Gao and G. Z. Hu, *Small*, 2025, 2409129.

7 Z. F. Ke, L. Zhang, Q. Liu, Q. L. Zhu, C. L. Liu and G. Z. Hu, *Int. J. Hydrogen Energy*, 2024, **49**, 862–874.

8 X. Y. Zhang, S. Y. Liang, F. Li and Y. P. Bai, *Chem. Eng. J.*, 2025, **503**, 158603.

9 J. T. Ren, L. Chen, H. Y. Wang, W. W. Tian and Z. Y. Yuan, *Energy Environ. Sci.*, 2024, **17**, 49–113.

10 K. M. Zhao, S. Q. Liu, Y. Y. Li, X. L. Wei, G. Y. Ye, W. W. Zhu, Y. K. Su, J. Wang, H. T. Liu, Z. He, Z. Y. Zhou and S. G. Sun, *Adv. Energy Mater.*, 2022, **12**, 2103588.

11 D. Bao, Q. Zhang, F. L. Meng, H. X. Zhong, M. M. Shi, Y. Zhang, J. M. Yan, Q. Jiang and X. B. Zhang, *Adv. Mater.*, 2016, **29**, 1604799.

This journal is © The Royal Society of Chemistry 2025

Chem. Soc. Rev., 2025, **54**, 5108–5145 | **5139**

12 P. L. Deng, F. Yang, Z. T. Wang, S. H. Chen, Y. Z. Zhou, S. Zaman and B. Y. Xia, *Angew. Chem., Int. Ed.*, 2020, **59**, 10807–10813.

13 H. R. Zhang, H. J. Wang, X. Q. Cao, M. S. Chen, Y. L. Liu, Y. T. Zhou, M. Huang, L. Xia, Y. Wang, T. S. Li, D. D. Zheng, Y. S. Luo, S. J. Sun, X. Zhao and X. P. Sun, *Adv. Mater.*, 2024, **36**, 2312746.

14 Z. Y. Li, Z. Li, H. Y. Yao, Y. Wei and J. S. Hu, *J. Colloid Interface Sci.*, 2024, **653**, 857–866.

15 Y. Liu, L. Zhang, Q. L. Xu, S. J. Zhang, Y. T. Zhou and G. Z. Hu, *Adv. Funct. Mater.*, 2025, **35**, 2413134.

16 Y. Z. D. Tong, X. H. Huang, N. Liu, R. K. Zhao and G. Z. Hu, *Desalination*, 2025, **600**, 118535.

17 Z. Y. Li, M. S. Chen, L. Zhang, R. Xing, J. S. Hu, X. H. Huang, C. H. Zhou, Y. T. Zhou, T. Wågberg and G. Z. Hu, *J. Mater. Chem. A*, 2023, **11**, 2155–2167.

18 Z. R. Wang, X. H. Huang, Y. Z. D. Tong, T. Wang, M. Xu, R. Li and G. Z. Hu, *Chem. Eng. J.*, 2025, **504**, 158899.

19 Y. T. Liu, W. X. Qiu, P. F. Wang, R. Li, K. Liu, K. M. Omer, Z. Y. Jin and P. P. Li, *Appl. Catal., B*, 2024, **340**, 123228.

20 J. S. Hu, Q. L. Xu, X. Y. Wang, X. H. Huang, C. H. Zhou, Y. Ye, L. Zhang and H. Pang, *Carbon Energy*, 2023, **5**, e315.

21 Q. L. Xu, L. Zhang, L. Li, S. J. Zhang, Y. T. Zhou and G. Z. Hu, *Adv. Funct. Mater.*, 2025, **35**, 2414379.

22 Y. Ye, L. Zhang, Q. L. Zhu, Z. A. Du, T. Wågberg and G. Z. Hu, *J. Colloid Interface Sci.*, 2023, **650**, 1350–1360.

23 J. W. Wu, Y. Z. D. Tong, X. H. Huang, D. Y. Qin, R. K. Zhao, R. Li and G. Z. Hu, *Desalination*, 2025, **600**, 118479.

24 Y. Z. Li, T. T. Xu, Q. Huang, L. T. Zhu, Y. Y. Yan, P. Peng and F. F. Li, *ACS Catal.*, 2023, **13**, 7597–7605.

25 S. Y. Lin, X. Li, D. Y. Yuan, Y. T. Liu, Z. Y. Jin and P. P. Li, *Small*, 2024, **20**, 2406235.

26 K. S. Sun, L. Zhang, S. J. Zhang and X. W. Li, *J. Alloys Compd.*, 2025, **1011**, 178419.

27 Q. R. Liang, W. Q. Li, L. Xie, Y. J. He, B. L. Qiu, H. Zeng, S. Zhou, J. Zeng, T. Y. Liu, M. Yan, K. Liang, O. Terasaki, L. Jiang and B. Kong, *Nano Lett.*, 2022, **22**, 2889–2897.

28 D. B. Liu, X. Y. Li, S. M. Chen, H. Yan, C. D. Wang, C. Q. Wu, Y. A. Haleem, S. Duan, J. L. Lu, B. H. Ge, P. M. Ajayan, Y. Luo, J. Jiang and L. Song, *Nat. Energy*, 2019, **4**, 512–518.

29 R. L. Zhang, Y. Z. Li, X. Zhou, A. Yu, Q. Huang, T. T. Xu, L. T. Zhu, P. Peng, S. Y. Song, L. Echegoyen and F. F. Li, *Nat. Commun.*, 2023, **14**, 2460.

30 J. Hong, M. S. Chen, L. Zhang, L. Qin, J. S. Hu, X. H. Huang, C. H. Zhou, Y. T. Zhou, T. Wågberg and G. Z. Hu, *Chem. Eng. J.*, 2023, **455**, 140401.

31 Q. L. Xu, J. S. Hu, C. H. Zhou, L. Zhang, Q. Q. Kong, S. S. Gao and G. Z. Hu, *Chem. Eng. J.*, 2024, **499**, 156425.

32 P. P. Li, L. Liao, Z. W. Fang, G. H. Su, Z. Y. Jin and G. H. Yu, *Proc. Natl. Acad. Sci. U. S. A.*, 2023, **120**, e2305489120.

33 Q. Q. Cheng, S. B. Han, K. Mao, C. Chen, L. J. Yang, Z. Q. Zou, M. Gu, Z. Hu and H. Yang, *Nano Energy*, 2018, **52**, 485–493.

34 M. B. Stevens, L. J. Enman, A. S. Batchellor, M. R. Cosby, A. E. Vise, C. D. M. Trang and S. W. Boettcher, *Chem. Mater.*, 2016, **29**, 120–140.

35 Q. L. Xu, J. S. Hu, H. Y. Yao, J. Lei, C. H. Zhou, L. Zhang and H. Pang, *ACS Appl. Mater. Interfaces*, 2024, **16**, 42352–42362.

36 Z. C. Nie, M. S. Chen, L. Zhang, Q. Feng, J. S. Hu, X. H. Huang, C. H. Zhou, Y. T. Zhou, T. Wågberg and G. Z. Hu, *Chem. Eng. J.*, 2023, **463**, 142411.

37 X. H. Lv, Z. X. Xiao, H. Y. Wang, X. L. Wang, L. L. Shan, F. L. Wang, C. Y. Wei, X. J. Tang and Y. L. Chen, *J. Energy Chem.*, 2021, **54**, 626–638.

38 H. J. Niu, Y. P. Chen, R. M. Sun, A. J. Wang, L. P. Mei, L. Zhang and J. J. Feng, *J. Power Sources*, 2020, **480**, 229107.

39 J. Zhang, J. W. Chen, Y. Luo, Y. H. Chen, C. Y. Zhang, Y. J. Luo, Y. L. Xue, H. G. Liu, G. Wang and R. L. Wang, *J. Energy Chem.*, 2021, **60**, 503–511.

40 H. H. Xie, B. Du, X. X. Huang, D. H. Zeng, H. Meng, H. J. Lin, W. Li, T. Asefa and Y. Y. Meng, *Small*, 2023, **19**, 2303214.

41 L. B. Zong, K. C. Fan, P. Li, F. H. Lu, B. Li and L. Wang, *Adv. Energy Mater.*, 2023, **13**, 2203611.

42 Y. Ye, L. Zhang, Z. C. Nie, N. P. Li, S. X. Zhou, H. S. Wang, T. Wågberg and G. Z. Hu, *Chem. Eng. J.*, 2022, **446**, 137210.

43 Z. Y. Li, L. Zhang, Q. L. Zhu, Z. F. Ke and G. Z. Hu, *J. Colloid Interface Sci.*, 2024, **653**, 1577–1587.

44 F. H. Lu, K. C. Fan, L. X. Cui, B. Li, Y. Yang, L. B. Zong and L. Wang, *Appl. Catal., B*, 2022, **313**, 121464.

45 K. Srinivas, Z. Chen, F. Ma, A. R. Chen, Z. H. Zhang, Y. Wu, M. Q. Zhu and Y. F. Chen, *Appl. Catal., B*, 2023, **335**, 122887.

46 Y. C. Wang, Q. C. Wang, J. Wu, X. Zhao, Y. Xiong, F. H. Luo and Y. P. Lei, *Nano Energy*, 2022, **103**, 107815.

47 W. J. Xu, H. Tang, H. F. Gu, H. Y. Xi, P. F. Wu, B. L. Liang, Q. Q. Liu and W. X. Chen, *J. Mater. Chem. A*, 2022, **10**, 14732–14746.

48 L. J. Zhang, N. Jin, Y. B. Yang, X. Y. Miao, H. Wang, J. Luo and L. L. Han, *Nano-Micro Lett.*, 2023, **15**, 228.

49 Y. Y. Wu, C. C. Ye, L. Yu, Y. F. Liu, J. F. Huang, J. B. Bi, L. Xue, J. W. Sun, J. Yang, W. Q. Zhang, X. Wang, P. Xiong and J. W. Zhu, *Energy Storage Mater.*, 2022, **45**, 805–813.

50 W. Ye, S. M. Chen, Y. Lin, L. Yang, S. J. Chen, X. S. Zheng, Z. M. Qi, C. M. Wang, R. Long, M. Chen, J. F. Zhu, P. Gao, L. Song, J. Jiang and Y. J. Xiong, *Chem*, 2019, **5**, 2865–2878.

51 Y. Y. Guo, P. F. Yuan, J. N. Zhang, Y. F. Hu, I. S. Amiinu, X. Wang, J. G. Zhou, H. C. Xia, Z. B. Song, Q. Xu and S. C. Mu, *ACS Nano*, 2018, **12**, 1894–1901.

52 L. L. Zhang, J. Rong, Y. X. Lin, Y. Q. Yang, H. Z. Zhu, X. H. Yu, X. D. Kang, C. L. Chen, H. M. Cheng and G. Liu, *Adv. Funct. Mater.*, 2023, **33**, 2307947.

53 F. Mo, Q. X. Zhou, W. D. Xue, W. T. Liu, S. Z. Xu, Z. L. Hou, J. L. Wang and Q. Wang, *Adv. Energy Mater.*, 2023, **13**, 2301711.

54 X. P. Han, X. F. Ling, Y. Wang, T. Y. Ma, C. Zhong, W. B. Hu and Y. D. Deng, *Angew. Chem., Int. Ed.*, 2019, **58**, 5359–5364.

55 T. P. Zhou, H. Shan, H. Yu, C. A. Zhong, J. K. Ge, N. Zhang, W. S. Chu, W. S. Yan, Q. Xu, H. A. Wu, C. Z. Wu and Y. Xie, *Adv. Mater.*, 2020, **32**, 2003251.

56 X. Y. Yang, W. Q. Song, T. Zhang, Z. C. Huang, J. F. Zhang, J. Ding and W. B. Hu, *Adv. Energy Mater.*, 2023, **13**, 2301737.

57 J. W. Hu, D. Y. Wu, C. Zhu, C. Hao, C. C. Xin, J. W. Zhang, J. Y. Guo, N. N. Li, G. F. Zhang and Y. T. Shi, *Nano Energy*, 2020, **72**, 104670.

5140 | *Chem. Soc. Rev.*, 2025, **54**, 5108–5145

This journal is © The Royal Society of Chemistry 2025

58 J. W. Wang, C. G. Hu, L. G. Wang, Y. Yuan, K. Zhu, Q. Zhang, L. Yang, J. Lu and Z. Y. Bai, *Adv. Funct. Mater.*, 2023, **33**, 2304277.

59 X. G. Fu, G. P. Jiang, G. B. Wen, R. Gao, S. Li, M. Li, J. B. Zhu, Y. Zheng, Z. Q. Li, Y. F. Hu, L. Yang, Z. Y. Bai, A. P. Yu and Z. W. Chen, *Appl. Catal., B*, 2021, **293**, 120176.

60 Y. G. Wu, X. N. Tang, K. Yuan and Y. W. Chen, *Energy Environ. Sci.*, 2023, **16**, 5663–5687.

61 J. B. Liu, J. W. Liao, K. Huang, J. C. Dong, G. C. He, Z. C. Gong and H. L. Fei, *Adv. Mater.*, 2023, **35**, 2211398.

62 C. L. Xu, C. Z. Guo, J. P. Liu, B. H. Hu, J. Y. Dai, M. Wang, R. Jin, Z. L. Luo, H. L. Li and C. G. Chen, *Energy Storage Mater.*, 2022, **51**, 149–158.

63 Y. Pan, X. L. Ma, M. M. Wang, X. Yang, S. J. Liu, H. C. Chen, Z. W. Zhuang, Y. H. Zhang, W. C. Cheong, C. Zhang, X. Cao, R. G. Shen, Q. Xu, W. Zhu, Y. Q. Liu, X. D. Wang, X. J. Zhang, W. S. Yan, J. Li, H. M. Chen, C. Chen and Y. D. Li, *Adv. Mater.*, 2022, **34**, 2203621.

64 Y. Y. Qiao, P. F. Yuan, Y. F. Hu, J. N. Zhang, S. C. Mu, J. H. Zhou, H. Li, H. C. Xia, J. He and Q. Xu, *Adv. Mater.*, 2018, **30**, 1804504.

65 R. G. Cao, R. Thapa, H. Kim, X. D. Xu, M. Gyu Kim, Q. Li, N. Park, M. L. Liu and J. Cho, *Nat. Commun.*, 2013, **4**, 2076.

66 M. R. Gao, J. X. Liang, Y. R. Zheng, Y. F. Xu, J. Jiang, Q. Gao, J. Li and S. H. Yu, *Nat. Commun.*, 2015, **6**, 5982.

67 H. Y. Jin, J. Wang, D. F. Su, Z. Z. Wei, Z. F. Pang and Y. Wang, *J. Am. Chem. Soc.*, 2015, **137**, 2688–2694.

68 J. Wang, Z. Q. Huang, W. Liu, C. R. Chang, H. L. Tang, Z. J. Li, W. X. Chen, C. J. Jia, T. Yao, S. Q. Wei, Y. Wu and Y. D. Li, *J. Am. Chem. Soc.*, 2017, **139**, 17281–17284.

69 P. Q. Yin, T. Yao, Y. Wu, L. R. Zheng, Y. Lin, W. Liu, H. X. Ju, J. F. Zhu, X. Hong, Z. X. Deng, G. Zhou, S. Q. Wei and Y. D. Li, *Angew. Chem., Int. Ed.*, 2016, **55**, 10800–10805.

70 P. Q. Yin, T. Yao, Y. Wu, L. R. Zheng, Y. Lin, W. Liu, H. X. Ju, J. F. Zhu, X. Hong, Z. X. Deng, G. Zhou, S. Q. Wei and Y. D. Li, *Adv. Mater.*, 2018, **30**, 1801732.

71 D. F. Qi, Y. F. Liu, M. Hu, X. Y. Peng, Y. Qiu, S. S. Zhang, W. Liu, H. Y. Li, G. Z. Hu, L. C. Zhuo, Y. J. Qin, J. He, G. C. Qi, J. Q. Sun, J. Luo and X. J. Liu, *Small*, 2020, **16**, 2004855.

72 M. J. Liu, J. Lee, T. C. Yang, F. Y. Zheng, J. Zhao, C. M. Yang and L. Y. S. Lee, *Small Methods*, 2021, **5**, 2001165.

73 F. S. Yu, J. Y. Zhan, D. T. Chen, J. Y. Guo, S. B. Zhang and L. H. Zhang, *Adv. Funct. Mater.*, 2023, **33**, 2214425.

74 Z. Wang, Z. Lu, Q. T. Ye, Z. B. Yang, R. J. Xu, K. X. Kong, Y. F. Zhang, T. Yan, Y. P. Liu, Z. J. Pan, Y. Z. Huang and X. H. Lu, *Adv. Funct. Mater.*, 2024, **34**, 2315150.

75 C. J. Lei, Y. Wang, Y. Hou, P. Liu, J. Yang, T. Zhang, X. D. Zhuang, M. W. Chen, B. Yang, L. C. Lei, C. Yuan, M. Qiu and X. L. Feng, *Energy Environ. Sci.*, 2019, **12**, 149–156.

76 M. Jiang, F. Wang, F. Yang, H. He, J. Yang, W. Zhang, J. Y. Luo, J. Zhang and C. P. Fu, *Nano Energy*, 2022, **93**, 106793.

77 P. Kumari, N. Bahadur, L. X. Kong, L. A. O'Dell, A. Merenda and L. F. Dumée, *Adv. Mater.*, 2022, **3**, 2309–2323.

78 J. Brownless, J. W. Zhang and A. M. Song, *Carbon*, 2020, **168**, 201–208.

79 Z. Zhang and J. T. Yates, *Chem. Rev.*, 2012, **112**, 5520–5551.

80 R. T. Tung, *Appl. Phys. Rev.*, 2014, **1**, 011304.

81 Z. C. Zhang, G. G. Liu, X. Y. Cui, B. Chen, Y. H. Zhu, Y. Gong, F. Saleem, S. B. Xi, Y. H. Du, A. Borgna, Z. C. Lai, Q. H. Zhang, B. Li, Y. Zong, Y. Han, L. Gu and H. Zhang, *Adv. Mater.*, 2018, **30**, 1801741.

82 H. M. Li, S. P. Li, R. J. Guan, Z. Y. Jin, D. Xiao, Y. Guo and P. P. Li, *ACS Catal.*, 2024, **14**, 12042–12050.

83 X. Y. Zhang, F. Li, Z. Z. Li and Y. P. Bai, *J. Mater. Chem. A*, 2025, **13**, 5304–5314.

84 L. Zhang, B. Wang, J. S. Hu, X. H. Huang, W. Y. Ma, N. P. Li, T. Wågberg and G. Z. Hu, *J. Colloid Interface Sci.*, 2022, **625**, 521–531.

85 X. Y. Wang, X. Q. Xu, Y. Nie, R. H. Wang and J. L. Zou, *Adv. Sci.*, 2023, **10**, 2301961.

86 B. W. Wang, J. X. Zou, X. C. Shen, Y. C. Yang, G. Z. Hu, W. Li, Z. M. Peng, D. Banham, A. G. Dong and D. Y. Zhao, *Nano Energy*, 2019, **63**, 103851.

87 Z. J. Li, S. Q. Ji, C. Wang, H. X. Liu, L. P. Leng, L. Du, J. C. Gao, M. Qiao, J. H. Horton and Y. Wang, *Adv. Mater.*, 2023, **35**, 2300905.

88 M. Liu, N. Li, S. F. Cao, X. M. Wang, X. Q. Lu, L. J. Kong, Y. H. Xu and X. H. Bu, *Adv. Mater.*, 2022, **34**, 2107421.

89 Z. H. Pei, X. F. Lu, H. B. Zhang, Y. X. Li, D. Y. Luan and X. W. Lou, *Angew. Chem., Int. Ed.*, 2022, **61**, e202207537.

90 C. H. He, Q. Q. Liu, H. M. Wang, C. F. Xia, F. M. Li, W. Guo and B. Y. Xia, *Small*, 2023, **19**, 2207474.

91 J. G. Hou, Y. Q. Sun, Y. Z. Wu, S. Y. Cao and L. C. Sun, *Adv. Funct. Mater.*, 2018, **28**, 1704447.

92 L. Zhang, Y. X. Zhu, Z. C. Nie, Z. Y. Li, Y. Ye, L. H. Li, J. Hong, Z. H. Bi, Y. T. Zhou and G. Z. Hu, *ACS Nano*, 2021, **15**, 13399–13414.

93 S. Q. Fu, Y. R. Ma, X. C. Yang, X. Yao, Z. Jiao, L. L. Cheng and P. D. Zhao, *Appl. Catal., B*, 2023, **333**, 122813.

94 S. Ni, H. N. Qu, Z. H. Xu, X. Y. Zhu, H. F. Xing, L. Wang, J. M. Yu, H. Z. Liu, C. M. Chen and L. R. Yang, *Appl. Catal., B*, 2021, **299**, 120638.

95 Z. C. Zhuang, L. X. Xia, J. Z. Huang, P. Zhu, Y. Li, C. L. Ye, M. G. Xia, R. H. Yu, Z. Q. Lang, J. X. Zhu, L. R. Zheng, Y. Wang, T. Y. Zhai, Y. Zhao, S. Q. Wei, J. Li, D. S. Wang and Y. D. Li, *Angew. Chem., Int. Ed.*, 2022, **62**, e202212335.

96 M. Z. Gu, L. Jiang, S. R. Zhao, H. Wang, M. Lin, X. Y. Deng, X. M. Huang, A. Gao, X. D. Liu, P. Sun and X. J. Zhang, *ACS Nano*, 2022, **16**, 15425–15439.

97 J. Y. Chen, H. Li, C. Fan, Q. W. Meng, Y. W. Tang, X. Y. Qiu, G. T. Fu and T. Y. Ma, *Adv. Mater.*, 2020, **32**, 2003134.

98 K. Khan, X. X. Yan, Q. M. Yu, S. H. Bae, J. J. White, J. X. Liu, T. C. Liu, C. J. Sun, J. Kim, H. M. Cheng, Y. Wang, B. L. Liu, K. Amine, X. Q. Pan and Z. T. Luo, *Nano Energy*, 2021, **90**, 106488.

99 H. X. Li, Y. L. Wen, M. Jiang, Y. Yao, H. H. Zhou, Z. Y. Huang, J. W. Li, S. Q. Jiao, Y. F. Kuang and S. L. Luo, *Adv. Funct. Mater.*, 2021, **31**, 2102420.

This journal is © The Royal Society of Chemistry 2025

Chem. Soc. Rev., 2025, **54**, 5108–5145 | 5141

100 M. Li, H. Y. Zhu, Q. Yuan, T. Y. Li, M. M. Wang, P. Zhang, Y. L. Zhao, D. L. Qin, W. Y. Guo, B. Liu, X. Yang, Y. Q. Liu and Y. Pan, *Adv. Funct. Mater.*, 2023, **33**, 2210867.

101 X. X. Yan, D. Liu, P. F. Guo, Y. F. He, X. Q. Wang, Z. L. Li, H. G. Pan, D. L. Sun, F. Fang and R. B. Wu, *Adv. Mater.*, 2023, **35**, 2210975.

102 Y. Wang, J. Wu, S. H. Tang, J. R. Yang, C. L. Ye, J. Chen, Y. G. Lei and D. S. Wang, *Angew. Chem., Int. Ed.*, 2023, **62**, e202219191.

103 F. T. Kong, M. Wang, Y. F. Huang, G. Meng, M. X. Chen, H. Tian, Y. F. Chen, C. Chen, Z. W. Chang, X. Z. Cui and J. L. Shi, *Energy Storage Mater.*, 2023, **54**, 533–542.

104 S. P. Zhang, G. Wang, B. B. Wang, J. M. Wang, J. T. Bai and H. Wang, *Adv. Funct. Mater.*, 2020, **30**, 2001592.

105 D. Y. Chung, S. B. Park, H. Lee, H. Kim, Y. H. Chung, J. M. Yoo, D. Ahn, S. H. Yu, K. S. Lee, M. Ahmadi, H. X. Ju, H. D. Abruña, S. J. Yoo, B. S. Mun and Y. E. Sung, *ACS Energy Lett.*, 2020, **5**, 2827–2834.

106 D. C. Duan, J. L. Huo, J. X. Chen, B. Chi, Z. S. Chen, S. H. Sun, Y. Zhao, H. Zhao, Z. M. Cui and S. J. Liao, *Small*, 2024, **20**, 2310491.

107 M. M. Tong, F. F. Sun, Y. Xie, Y. Wang, Y. Q. Yang, C. G. Tian, L. Wang and H. G. Fu, *Angew. Chem., Int. Ed.*, 2021, **60**, 14005–14012.

108 L. Cheng, X. Y. Yue, L. X. Wang, D. N. Zhang, P. Zhang, J. J. Fan and Q. J. Xiang, *Adv. Mater.*, 2021, **33**, 2105135.

109 Y. H. Xie, X. Chen, K. A. Sun, J. Q. Zhang, W. H. Lai, H. Liu and G. X. Wang, *Angew. Chem., Int. Ed.*, 2023, **62**, e202301833.

110 D. Liang, C. Lian, Q. C. Xu, M. M. Liu, H. L. Liu, H. Jiang and C. Z. Li, *Appl. Catal., B*, 2020, **268**, 118417.

111 P. F. Zhang, Y. D. Liu, T. T. Liang, E. H. Ang, X. Zhang, F. Ma and Z. F. Dai, *Appl. Catal., B*, 2021, **284**, 119738.

112 Z. X. Xu, S. Jin, M. H. Seo and X. L. Wang, *Appl. Catal., B*, 2021, **292**, 120168.

113 T. F. Li, J. W. Yin, D. M. Sun, M. Y. Zhang, H. Pang, L. Xu, Y. W. Zhang, J. Yang, Y. W. Tang and J. M. Xue, *Small*, 2022, **18**, 2106592.

114 L. Q. Deng, K. Zhang, D. Shi, S. F. Liu, D. Q. Xu, Y. L. Shao, J. X. Shen, Y. Z. Wu and X. P. Hao, *Appl. Catal., B*, 2021, **299**, 120660.

115 S. L. Jiao, X. W. Fu and H. W. Huang, *Adv. Funct. Mater.*, 2022, **32**, 2107651.

116 M. M. Wang, M. K. Zhang, W. W. Song, W. T. Zhong, X. Y. Wang, J. Wang, T. M. Sun and Y. F. Tang, *Chem. Commun.*, 2021, **57**, 785–788.

117 C. R. Pi, X. X. Li, X. M. Zhang, H. Song, Y. Zheng, B. Gao, A. Kızılaslan, P. K. Chu and K. F. Huo, *Small*, 2022, **18**, 2201137.

118 C. J. Gu, G. Y. Zhou, J. Yang, H. Pang, M. Y. Zhang, Q. Zhao, X. F. Gu, S. Tian, J. B. Zhang, L. Xu and Y. W. Tang, *Chem. Eng. J.*, 2022, **443**, 136321.

119 G. B. Chen, Y. An, S. W. Liu, F. F. Sun, H. Y. Qi, H. F. Wu, Y. H. He, P. Liu, R. Shi, J. Zhang, A. Kuc, U. Kaiser, T. Zhang, T. Heine, G. Wu and X. L. Feng, *Energy Environ. Sci.*, 2022, **15**, 2619–2628.

120 Y. Zhang, C. X. Li, J. Li, X. N. Liu, G. J. Li, B. Li and L. Wang, *J. Mater. Chem. A*, 2023, **11**, 11326–11333.

121 T. Zhang, X. Han, H. Liu, M. Biset-Peiró, J. Li, X. Zhang, P. Y. Tang, B. Yang, L. R. Zheng, J. R. Morante and J. Arbiol, *Adv. Funct. Mater.*, 2022, **32**, 2111446.

122 W. J. Zang, T. Sun, T. Yang, S. B. Xi, M. Waqar, Z. K. Kou, Z. Y. Lyu, Y. P. Feng, J. Wang and S. J. Pennycook, *Adv. Mater.*, 2021, **33**, 2003846.

123 W. L. Zhou, H. Su, Y. L. Li, M. H. Liu, H. Zhang, X. X. Zhang, X. Sun, Y. Z. Xu, Q. H. Liu and S. Q. Wei, *ACS Energy Lett.*, 2021, **6**, 3359–3366.

124 J. Yang, W. G. Liu, M. Q. Xu, X. Y. Liu, H. F. Qi, L. L. Zhang, X. F. Yang, S. S. Niu, D. Zhou, Y. F. Liu, Y. Su, J. F. Li, Z. Q. Tian, W. Zhou, A. Q. Wang and T. Zhang, *J. Am. Chem. Soc.*, 2021, **143**, 14530–14539.

125 J. W. Wan, Z. H. Zhao, H. S. Shang, B. Peng, W. X. Chen, J. J. Pei, L. R. Zheng, J. C. Dong, R. Cao, R. Sarangi, Z. L. Jiang, D. N. Zhou, Z. B. Zhuang, J. T. Zhang, D. S. Wang and Y. D. Li, *J. Am. Chem. Soc.*, 2022, **142**, 8431–8439.

126 Y. L. Zhao, H. C. Chen, X. L. Ma, J. Y. Li, Q. Yuan, P. Zhang, M. M. Wang, J. X. Li, M. Li, S. F. Wang, H. Guo, R. B. Hu, K. H. Tu, W. Zhu, X. N. Li, X. Yang and Y. Pan, *Adv. Mater.*, 2024, **36**, 2308243.

127 F. Q. Wang, R. Zhang, Y. Y. Zhang, Y. Li, J. Zhang, W. H. Yuan, H. Liu, F. Wang and H. L. Xin, *Adv. Funct. Mater.*, 2023, **33**, 2213863.

128 L. S. Peng, J. Yang, Y. Q. Yang, F. R. Qian, Q. Wang, D. X. Sun-Waterhouse, L. Shang, T. R. Zhang and G. I. N. Waterhouse, *Adv. Mater.*, 2022, **34**, 2202544.

129 L. B. Li, S. H. Huang, R. Cao, K. Yuan, C. B. Lu, B. Y. Huang, X. N. Tang, T. Hu, X. D. Zhuang and Y. W. Chen, *Small*, 2022, **18**, 2105387.

130 Y. Liu, S. S. Zhang, C. Jiao, H. M. Chen, G. Wang, W. J. Wu, Z. W. Zhuo and J. J. Mao, *Adv. Sci.*, 2022, **10**, 2206107.

131 S. C. Ding, J. A. Barr, Q. R. Shi, Y. C. Zeng, P. Tieu, Z. Y. Lyu, L. Z. Fang, T. Li, X. Q. Pan, S. P. Beckman, D. Du, H. F. Lin, J. C. Li, G. Wu and Y. H. Lin, *ACS Nano*, 2022, **16**, 15165–15174.

132 S. K. Zhang, Q. X. Zhou, L. Y. Fang, R. Wang, T. Y. Lu, Q. Zhao, X. F. Gu, S. Tian, L. Xu, H. Pang, J. Yang, Y. W. Tang and S. H. Sun, *Appl. Catal., B*, 2023, **328**, 122489.

133 M. R. Wang, W. J. Yang, X. Z. Li, Y. S. Xu, L. R. Zheng, C. L. Su and B. Liu, *ACS Energy Lett.*, 2021, **6**, 379–386.

134 H. J. Shen, E. Gracia-Espino, J. Y. Ma, H. D. Tang, X. Mamat, T. Wagberg, G. Z. Hu and S. J. Guo, *Nano Energy*, 2017, **35**, 9–16.

135 K. Yuan, D. Lützenkirchen-Hecht, L. B. Li, L. Shuai, Y. Z. Li, R. Cao, M. Qiu, X. D. Zhuang, M. K. H. Leung, Y. W. Chen and U. Scherf, *J. Am. Chem. Soc.*, 2020, **142**, 2404–2412.

136 Y. M. Zhao, P. C. Zhang, C. Xu, X. Y. Zhou, L. M. Liao, P. J. Wei, E. Liu, H. Q. Chen, Q. G. He and J. G. Liu, *ACS Appl. Mater. Interfaces*, 2020, **12**, 17334–17342.

137 X. K. Wang, X. K. Zhou, C. Li, H. X. Yao, C. H. Zhang, J. Zhou, R. Xu, L. Chu, H. L. Wang, M. Gu, H. Q. Jiang and M. H. Huang, *Adv. Mater.*, 2022, **34**, 2204021.

138 B. L. Yang, X. L. Li, Q. Cheng, X. D. Jia, Y. J. Liu and Z. H. Xiang, *Nano Energy*, 2022, **101**, 107565.

5142 | *Chem. Soc. Rev.*, 2025, **54**, 5108–5145

This journal is © The Royal Society of Chemistry 2025

139 Y. J. Chen, R. Gao, S. F. Ji, H. J. Li, K. Tang, P. Jiang, H. B. Hu, Z. D. Zhang, H. G. Hao, Q. Y. Qu, X. Liang, W. X. Chen, J. C. Dong, D. S. Wang and Y. D. Li, *Angew. Chem., Int. Ed.*, 2020, **60**, 3212–3221.

140 J. B. Liu, D. S. Wang, K. Huang, J. C. Dong, J. W. Liao, S. Dai, X. Tang, M. M. Yan, H. S. Gong, J. J. Liu, Z. C. Gong, R. Liu, C. Y. Cui, G. L. Ye, X. L. Zou and H. L. Fei, *ACS Nano*, 2021, **15**, 18125–18134.

141 Y. J. Deng, J. M. Luo, B. Chi, H. B. Tang, J. Li, X. C. Qiao, Y. J. Shen, Y. J. Yang, C. M. Jia, P. Rao, S. J. Liao and X. L. Tian, *Adv. Energy Mater.*, 2021, **11**, 2101222.

142 R. X. Qin, K. L. Liu, Q. Y. Wu and N. F. Zheng, *Chem. Rev.*, 2020, **120**, 11810–11899.

143 B. T. Hu, A. J. Huang, X. J. Zhang, Z. Chen, R. Y. Tu, W. Zhu, Z. B. Zhuang, C. Chen, Q. Peng and Y. D. Li, *Nano Res.*, 2021, **14**, 3482–3488.

144 L. L. Zhang, N. Zhang, H. S. Shang, Z. Y. Sun, Z. H. Wei, J. T. Wang, Y. T. Lei, X. C. Wang, D. Wang, Y. F. Zhao, Z. T. Sun, F. Zhang, X. Xiang, B. Zhang and W. X. Chen, *Nat. Commun.*, 2024, **15**, 9440.

145 J. L. Zhang, Y. H. Mou, W. R. Suo, S. J. Yang, J. Shen, H. Xu, Z. Q. Zeng, R. Zhang, Z. Z. Liang, Y. Wang, H. Q. Zheng, J. H. Cao and R. Cao, *Adv. Funct. Mater.*, 2025, **35**, 2417621.

146 Z. Y. Jin, R. J. Guan, X. Li, D. Y. Yuan and P. P. Li, *Chin. Chem. Lett.*, 2025, DOI: 10.1016/i.cclet.2024.110506.

147 J. X. Han, H. Tan, K. Guo, H. Y. Lv, X. Y. Peng, W. Zhang, H. P. Lin, U. P. Apfel and R. Cao, *Angew. Chem., Int. Ed.*, 2024, **63**, e202409793.

148 Y. J. Liu, G. J. Zhou, Z. Y. Zhang, H. T. Lei, Z. Yao, J. F. Li, J. Lin and R. Cao, *Chem. Sci.*, 2020, **11**, 87–96.

149 X. L. Li, H. T. Lei, L. S. Xie, N. Wang, W. Zhang and R. Cao, *Acc. Chem. Res.*, 2022, **55**, 878–892.

150 M. Yi, H. M. Li, M. H. Xie, P. P. Li, Z. Y. Jin and G. H. Yu, *Sci. China: Chem.*, 2024, **67**, DOI: 10.1007/s11426-024-2286-7.

151 Y. J. Wu, X. Y. Wang, B. B. Tian, W. Shuang, Z. Y. Bai and L. Yang, *Inorg. Chem. Front.*, 2023, **10**, 4209–4220.

152 Y. H. Han, Y. G. Wang, R. R. Xu, W. X. Chen, L. R. Zheng, A. J. Han, Y. Q. Zhu, J. Zhang, H. B. Zhang, J. Luo, C. Chen, Q. Peng, D. S. Wang and Y. D. Li, *Energy Environ. Sci.*, 2018, **11**, 2348–2352.

153 B. X. Zhang, J. L. Zhang, J. B. Shi, D. X. Tan, L. F. Liu, F. Y. Zhang, C. Lu, Z. Z. Su, X. N. Tan, X. Y. Cheng, B. X. Han, L. R. Zheng and J. Zhang, *Nat. Commun.*, 2019, **10**, 2980.

154 M. Huang, B. W. Deng, X. L. Zhao, Z. Y. Zhang, F. Li, K. L. Li, Z. H. Cui, L. X. Kong, J. M. Lu, F. Dong, L. L. Zhang and P. Chen, *ACS Nano*, 2022, **16**, 2110–2119.

155 S. X. Yang, Y. H. Yu, X. J. Gao, Z. P. Zhang and F. Wang, *Chem. Soc. Rev.*, 2021, **50**, 12985–13011.

156 X. Y. Li, X. S. Wu, Y. Zhao, Y. X. Lin, J. H. Zhao, C. Q. Wu, H. J. Liu, L. Shan, L. Yang, L. Song and J. Jiang, *Adv. Mater.*, 2023, **35**, 2302467.

157 X. L. Li, P. Li, J. D. Yang, L. S. Xie, N. Wang, H. T. Lei, C. C. Zhang, W. Zhang, Y. M. Lee, W. Q. Zhang, S. Fukuzumi, W. Nam and R. Cao, *J. Energy Chem.*, 2023, **76**, 617–621.

158 L. C. Liu and A. Corma, *Chem. Rev.*, 2018, **118**, 4981–5079.

159 Y. Feng, K. X. Song, W. Zhang, X. Y. Zhou, S. J. Yoo, J. G. Kim, S. F. Qiao, Y. G. Qi, X. Zou, Z. J. Chen, T. T. Qin, N. L. Yue, Z. Z. Wang, D. B. Li and W. T. Zheng, *J. Energy Chem.*, 2022, **70**, 211–218.

160 X. Wan, Q. T. Liu, J. Y. Liu, S. Y. Liu, X. Y. Liu, L. R. Zheng, J. X. Shang, R. H. Yu and J. L. Shui, *Nat. Commun.*, 2020, **13**, 2963.

161 Z. Wang, C. Zhu, H. Tan, J. Liu, L. L. Xu, Y. Q. Zhang, Y. P. Liu, X. X. Zou, Z. Liu and X. H. Lu, *Adv. Funct. Mater.*, 2021, **31**, 2104735.

162 J. Yu, J. Li, C. Y. Xu, Q. Liu, J. Y. Liu, R. R. Chen, J. H. Zhu, R. M. Li and J. Wang, *Carbon*, 2021, **185**, 96–104.

163 J. Quílez-Bermejo, S. García-Dalí, A. Daouli, A. Zitolo, R. L. S. Canevesi, M. Emo, M. T. Izquierdo, M. Badawi, A. Celzard and V. Fierro, *Adv. Funct. Mater.*, 2023, **33**, 2300405.

164 K. X. Ding, J. G. Hu, J. Luo, L. M. Zhao, W. Jin, Y. P. Liu, Z. H. Wu, G. Q. Zou, H. S. Hou and X. B. Ji, *Adv. Funct. Mater.*, 2022, **32**, 2207331.

165 Q. Yu, J. S. Lv, J. T. Li, R. H. Yu, J. S. Wu, S. B. Xi, X. Y. Li, N. Xu, L. Zhou and L. Q. Mai, *Energy Environ. Mater.*, 2022, **6**, e12389.

166 J. Zhang, Y. Xie, Q. K. Jiang, S. Guo, J. H. Huang, L. L. Xu, Y. Wang and G. Li, *J. Mater. Chem. A*, 2022, **10**, 16920–16927.

167 J. M. Guo, W. Q. Li, Y. C. Xu, Y. Q. Mao, Z. W. Mei, H. H. Li, Y. He, X. Y. San, K. Xu and X. G. Liang, *Small Methods*, 2023, **7**, 2201371.

168 J. J. Chen, S. Gu, R. Hao, Z. Y. Wang, M. Q. Li, Z. Q. Li, K. Liu, K. M. Liao, Z. Q. Wang, H. Huang, Y. Z. Li, K. L. Zhang and Z. G. Lu, *Rare Met.*, 2022, **41**, 2055–2062.

169 J. C. Li, Y. Meng, L. L. Zhang, G. Z. Li, Z. C. Shi, P. X. Hou, C. Liu, H. M. Cheng and M. H. Shao, *Adv. Funct. Mater.*, 2021, **31**, 2103360.

170 I. S. Amiinu, X. B. Liu, Z. H. Pu, W. Q. Li, Q. D. Li, J. Zhang, H. L. Tang, H. N. Zhang and S. C. Mu, *Adv. Funct. Mater.*, 2018, **28**, 1704638.

171 M. T. Zhang, H. Li, J. X. Chen, F. X. Ma, L. Zhen, Z. H. Wen and C. Y. Xu, *Adv. Funct. Mater.*, 2023, **33**, 2209726.

172 H. J. Huang, D. S. Yu, F. Hu, S. C. Huang, J. N. Song, H. Y. Chen, L. L. Li and S. J. Peng, *Angew. Chem., Int. Ed.*, 2022, **61**, e202116068.

173 Y. Y. Li, Z. H. Li, K. K. Shi, L. K. Luo, H. M. Jiang, Y. He, Y. L. Zhao, J. Y. He, L. Lin, Z. M. Sun and G. B. Sun, *Small*, 2024, **20**, 2309727.

174 W. J. Zhai, S. H. Huang, C. B. Lu, X. N. Tang, L. B. Li, B. Y. Huang, T. Hu, K. Yuan, X. D. Zhuang and Y. W. Chen, *Small*, 2022, **18**, 2107225.

175 S. Chandrasekaran, R. Hu, L. Yao, L. J. Sui, Y. P. Liu, A. Abdelkader, Y. L. Li, X. Z. Ren and L. B. Deng, *Nano-Micro Lett.*, 2023, **15**, 48.

176 Z. Y. Chen, X. Su, J. Ding, N. Yang, W. B. Zuo, Q. Y. He, Z. M. Wei, Q. Zhang, J. Huang and Y. M. Zhai, *Appl. Catal., B*, 2022, **308**, 121206.

177 H. B. Meng, B. Wu, D. T. Zhang, X. H. Zhu, S. Z. Luo, Y. You, K. Chen, J. C. Long, J. X. Zhu, L. P. Liu, S. B. Xi,

This journal is © The Royal Society of Chemistry 2025

Chem. Soc. Rev., 2025, **54**, 5108–5145 | 5143

T. Petit, D. S. Wang, X. M. Zhang, Z. J. Xu and L. Q. Mai, *Energy Environ. Sci.*, 2024, **17**, 704–716.

178 W. H. Luo, Y. Wang, L. X. Luo, S. Gong, M. N. Wei, Y. X. Li, X. P. Gan, Y. Y. Zhao, Z. H. Zhu and Z. Li, *ACS Catal.*, 2022, **12**, 1167–1179.

179 Y. R. Liu, S. Yuan, C. T. Sun, C. L. Wang, X. J. Liu, Z. H. Lv, R. Liu, Y. Z. Meng, W. X. Yang, X. Feng and B. Wang, *Adv. Energy Mater.*, 2023, **13**, 2302719.

180 Y. Q. Chen, J. N. Mao, H. Zhou, L. L. Xing, S. S. Qiao, J. L. Yuan, B. B. Mei, Z. X. Wei, S. L. Zhao, Y. H. Tang and C. B. Liu, *Adv. Funct. Mater.*, 2024, **34**, 2311664.

181 Q. Z. An, X. Zhang, C. Y. Yang, H. Su, W. L. Zhou, M. H. Liu, X. X. Zhang, X. Sun, S. W. Bo, F. F. Yu, J. J. Jiang, K. Zheng and Q. H. Liu, *Small*, 2023, **19**, 2304303.

182 H. Liu, L. Z. Jiang, Y. Y. Sun, J. Khan, B. Feng, J. M. Xiao, H. D. Zhang, H. J. Xie, L. N. Li, S. Y. Wang and L. Han, *Adv. Energy Mater.*, 2023, **13**, 2301223.

183 T. H. Nguyen, P. K. L. Tran, D. T. Tran, T. N. Pham, N. H. Kim and J. H. Lee, *Chem. Eng. J.*, 2022, **440**, 135781.

184 M. J. Wu, X. H. Yang, X. Cui, N. Chen, L. Du, M. Cherif, F. K. Chiang, Y. Wen, A. Hassanpour, F. Vidal, S. Omanovic, Y. K. Yang, S. H. Sun and G. X. Zhang, *Nano-Micro Lett.*, 2023, **15**, 232.

185 Q. R. Zhang, P. Kumar, X. F. Zhu, R. Daiyan, N. M. Bedford, K. H. Wu, Z. J. Han, T. R. Zhang, R. Amal and X. Y. Lu, *Adv. Energy Mater.*, 2021, **11**, 2100303.

186 Y. Zhang, X. Yu Gao, Z. Wen, C. C. Yang and Q. Jiang, *Chem. Eng. J.*, 2022, **446**, 137441.

187 Z. Wang, X. Y. Jin, R. J. Xu, Z. B. Yang, S. D. Ma, T. Yan, C. Zhu, J. Fang, Y. P. Liu, S. J. Hwang, Z. J. Pan and H. J. Fan, *ACS Nano*, 2023, **17**, 8622–8633.

188 H. Lv, P. Tong, H. Li, B. Sun, Y. Li, P. Qiao, H. Tian and H. Xia, *Chem. Eng. J.*, 2023, **478**, 147375.

189 H. Liu, L. Z. Jiang, J. Khan, X. X. Wang, J. M. Xiao, H. D. Zhang, H. J. Xie, L. N. Li, S. Y. Wang and L. Han, *Angew. Chem., Int. Ed.*, 2022, **62**, e202214988.

190 J. R. Bai, Y. B. Lian, Y. Y. Deng, M. Xiang, P. Xu, Q. F. Zhou, Y. W. Tang and Y. Q. Su, *Nano Res.*, 2024, **17**, 2291–2297.

191 F. F. Zhang, Y. L. Zhu, Y. J. Zhong, J. Zou, Y. Chen, L. H. Zu, Z. Y. Wang, J. J. Hinsch, Y. Wang, L. Zhang, Z. P. Shao and H. T. Wang, *J. Energy Chem.*, 2023, **85**, 154–163.

192 Y. Y. Ma, Y. Yu, J. H. Wang, J. Lipton, H. N. Tan, L. R. Zheng, T. Yang, Z. L. Liu, X. J. Loh, S. J. Pennycook, L. Shen, Z. K. Kou, A. D. Taylor and J. Wang, *Adv. Sci.*, 2022, **9**, 2105192.

193 L. Tao, Y. Q. Wang, Y. Q. Zou, N. N. Zhang, Y. Q. Zhang, Y. J. Wu, Y. Y. Wang, R. Chen and S. Y. Wang, *Adv. Energy Mater.*, 2019, **10**, 1901227.

194 P. Zhu, X. Xiong, D. S. Wang and Y. D. Li, *Adv. Energy Mater.*, 2023, **13**, 2300884.

195 J. X. Diao, Y. Qiu, S. Q. Liu, W. T. Wang, K. Chen, H. L. Li, W. Y. Yuan, Y. T. Qu and X. H. Guo, *Adv. Mater.*, 2019, **32**, 1905679.

196 A. L. Han, W. M. Sun, X. Wan, D. D. Cai, X. J. Wang, F. Li, J. L. Shui and D. S. Wang, *Angew. Chem., Int. Ed.*, 2023, **62**, e202303185.

197 H. S. Shang, X. Y. Zhou, J. C. Dong, A. Li, X. Zhao, Q. H. Liu, Y. Lin, J. J. Pei, Z. Li, Z. L. Jiang, D. N. Zhou, L. R. Zheng, Y. Wang, J. Zhou, Z. K. Yang, R. Cao, R. Sarangi, T. T. Sun, X. Yang, X. S. Zheng, W. S. Yan, Z. B. Zhuang, J. Li, W. X. Chen, D. S. Wang, J. T. Zhang and Y. D. Li, *Nat. Commun.*, 2020, **11**, 3049.

198 X. Wang, M. Li, P. Wang, D. M. Sun, L. F. Ding, H. Li, Y. W. Tang and G. T. Fu, *Small Methods*, 2023, **7**, 2300100.

199 J. Y. Chen, C. Fan, X. Y. Hu, C. Wang, Z. H. Huang, G. T. Fu, J. M. Lee and Y. W. Tang, *Small*, 2019, **15**, 1901518.

200 Z. C. Nie, L. Zhang, Q. L. Zhu, Z. F. Ke, Y. T. Zhou, T. Wågberg and G. Z. Hu, *J. Energy Chem.*, 2024, **88**, 202–212.

201 H. M. Liu, M. M. Jin, D. Zhan, J. M. Wang, X. Y. Cai, Y. T. Qiu and L. F. Lai, *Appl. Catal., B*, 2020, **272**, 118951.

202 Y. Lin, X. M. Chen, Y. X. Tuo, Y. Pan and J. Zhang, *J. Energy Chem.*, 2022, **70**, 27–35.

203 X. B. Yang, Y. Y. Wang, X. L. Tong and N. J. Yang, *Adv. Energy Mater.*, 2022, **12**, 2102261.

204 B. You, M. T. Tang, C. Tsai, F. Abild-Pedersen, X. L. Zheng and H. Li, *Adv. Mater.*, 2019, **31**, 1807001.

205 Z. H. Xia and S. J. Guo, *Chem. Soc. Rev.*, 2019, **48**, 3265–3278.

206 J. Yang, Z. Y. Wang, C. X. Huang, Y. Zhang, Q. H. Zhang, C. Chen, J. Y. Du, X. Zhou, Y. Zhang, H. Zhou, L. X. Wang, X. S. Zheng, L. Gu, L. M. Yang and Y. Wu, *Angew. Chem., Int. Ed.*, 2021, **60**, 22722–22728.

207 R. Chattot, T. Asset, P. Bordet, J. Drnec, L. Dubau and F. Maillard, *ACS Catal.*, 2016, **7**, 398–408.

208 Z. J. Li, H. Jang, D. N. Qin, X. L. Jiang, X. Q. Ji, M. G. Kim, L. J. Zhang, X. E. Liu and J. Cho, *J. Mater. Chem. A*, 2021, **9**, 4036–4043.

209 L. F. Gu, C. F. Li, J. W. Zhao, L. J. Xie, J. Q. Wu, Q. Ren and G. R. Li, *J. Mater. Chem. A*, 2021, **9**, 13279–13287.

210 F. Du, X. T. Ling, Z. Y. Wang, S. G. Guo, Y. T. Zhang, H. C. He, G. L. Li, C. H. Jiang, Y. Zhou and Z. G. Zou, *J. Catal.*, 2022, **389**, 132–139.

211 S. Zhu, L. T. Ding, X. H. Zhang, K. Wang, X. Wang, F. Yang and G. Y. Han, *Angew. Chem., Int. Ed.*, 2023, **62**, e202309545.

212 D. P. Xue, P. F. Yuan, S. Jiang, Y. F. Wei, Y. Zhou, C. L. Dong, W. F. Yan, S. C. Mu and J. N. Zhang, *Nano Energy*, 2023, **105**, 108020.

213 Y. Y. Jiang, K. Yang, M. G. Li, D. H. Xu and Z. H. Ma, *Mater. Chem. Front.*, 2024, **8**, 528–552.

214 H. S. Ahn and A. J. Bard, *J. Am. Chem. Soc.*, 2015, **138**, 313–318.

215 B. J. Trześniewski, O. Diaz-Morales, D. A. Vermaas, A. Longo, W. Bras, M. T. M. Koper and W. A. Smith, *J. Am. Chem. Soc.*, 2015, **137**, 15112–15121.

216 J. Y. C. Chen, L. Dang, H. Liang, W. Bi, J. B. Gerken, S. Jin, E. E. Alp and S. S. Stahl, *J. Am. Chem. Soc.*, 2015, **137**, 15090–15093.

217 Z. Fang, W. T. Zhao, T. Shen, D. P. Qiu, Y. C. Lv, X. M. Hou and Y. L. Hou, *Precis. Chem.*, 2023, **1**, 395–417.

218 J. O. Bockris and T. Otagawa, *J. Electrochem. Soc.*, 2019, **131**, 290–302.

5144 | *Chem. Soc. Rev.*, 2025, **54**, 5108–5145

This journal is © The Royal Society of Chemistry 2025

219 R. Larsson and L. Y. Johansson, *J. Power Sources*, 1990, **32**, 253–260.

220 Y. R. Liu, X. J. Liu, Z. H. Lv, R. Liu, L. H. Li, J. M. Wang, W. X. Yang, X. Jiang, X. Feng and B. Wang, *Angew. Chem., Int. Ed.*, 2022, **61**, e202117617.

221 G. G. Yang, J. W. Zhu, P. F. Yuan, Y. F. Hu, G. Qu, B. A. Lu, X. Y. Xue, H. B. Yin, W. Z. Cheng, J. Q. Cheng, W. J. Xu, J. Li, J. S. Hu, S. C. Mu and J. N. Zhang, *Nat. Commun.*, 2021, **12**, 1734.

222 T. He, Y. Chen, Q. M. Liu, B. Z. Lu, X. W. Song, H. T. Liu, M. Liu, Y. N. Liu, Y. Zhang, X. P. Ouyang and S. W. Chen, *Angew. Chem., Int. Ed.*, 2022, **61**, e202201007.

223 Y. Wang, X. P. Li, M. M. Zhang, J. F. Zhang, Z. L. Chen, X. R. Zheng, Z. L. Tian, N. Q. Zhao, X. P. Han, K. Zaghib, Y. S. Wang, Y. D. Deng and W. B. Hu, *Adv. Mater.*, 2022, **34**, 2107053.

224 C. X. Zhao, B. Q. Li, J. N. Liu and Q. Zhang, *Angew. Chem., Int. Ed.*, 2020, **60**, 4448–4463.

225 X. Zhao, F. L. Wang, X. P. Kong, R. Q. Fang and Y. W. Li, *J. Am. Chem. Soc.*, 2021, **143**, 16068–16077.

226 H. B. Liu, X. C. Xu, H. X. Xu, S. T. Wang, Z. Q. Niu, Q. H. Jia, L. Yang, R. Cao, L. R. Zheng and D. P. Cao, *Appl. Catal., B*, 2021, **297**, 120451.

227 L. L. Wang, Q. An, X. L. Sheng, Z. Y. Mei, Q. Jing, X. Y. Zhao, Q. J. Xu, L. Y. Duan, X. X. Zou and H. Guo, *Appl. Catal., B*, 2024, **343**, 123509.

228 Z. L. Fang, B. Bueken, D. E. De Vos and R. A. Fischer, *Angew. Chem., Int. Ed.*, 2015, **54**, 7234–7254.

229 J. H. Hong, C. H. Jin, J. Yuan and Z. Zhang, *Adv. Mater.*, 2017, **29**, 1606434.

230 D. F. Yan, Y. X. Li, J. Huo, R. Chen, L. M. Dai and S. Y. Wang, *Adv. Mater.*, 2017, **29**, 1606459.

231 M. Zheng and J. Wang, *Chem. Res. Chin. Univ.*, 2022, **38**, 1275–1281.

232 B. Zhang, J. W. Shan, W. L. Wang, P. Tsiakaras and Y. Y. Li, *Small*, 2022, **18**, 2106012.

233 H. L. Tu, H. X. Zhang, Y. H. Song, P. Z. Liu, Y. Hou, B. S. Xu, T. Liao, J. J. Guo and Z. Q. Sun, *Adv. Sci.*, 2023, **10**, 2305194.

234 F. L. Gong, Y. H. Liu, Y. Zhao, W. Liu, G. Zeng, G. Q. Wang, Y. H. Zhang, L. H. Gong and J. Liu, *Angew. Chem., Int. Ed.*, 2023, **62**, e202308091.

235 M. C. Luo and S. J. Guo, *Nat. Rev. Mater.*, 2017, **2**, 17059.

236 J. Kim, H. Jung, S. M. Jung, J. Hwang, D. Y. Kim, N. Lee, K. S. Kim, H. Kwon, Y. T. Kim, J. W. Han and J. K. Kim, *J. Am. Chem. Soc.*, 2020, **143**, 1399–1408.

237 X. M. Wang, G. F. Long, B. Liu, Z. L. Li, W. S. Gao, P. F. Zhang, H. Zhang, X. Zhou, R. Z. Duan, W. Hu and C. Li, *Angew. Chem., Int. Ed.*, 2023, **62**, e202301562.

238 J. X. Sun, P. Leng, Y. H. Xie, X. X. Yu, K. G. Qu, L. G. Feng, H. F. Bao, F. Luo and Z. H. Yang, *Appl. Catal., B*, 2022, **319**, 121905.

239 Y. J. Chen, H. Cui, Q. Jiang, X. Bai, P. Y. Shan, Z. P. Jia, S. Lu, P. Song, R. Feng, Q. Kang, Z. Y. Liang and H. K. Yuan, *ACS Appl. Nano Mater.*, 2023, **6**, 7694–7703.

240 N. Wang, R. G. Mei, L. Q. Chen, T. Yang, Z. W. Chen, X. D. Lin and Q. X. Liu, *Small*, 2024, **20**, 2400327.

241 X. Y. Li, X. S. Wu, Y. Zhao, Y. X. Lin, J. H. Zhao, C. Q. Wu, H. J. Liu, L. Shan, L. Yang, L. Song and J. Jiang, *Adv. Mater.*, 2023, **35**, 2302467.

242 Y. T. He, J. B. Yang, Y. Wang, Y. F. Jia, H. T. Li, Y. N. Liu, L. T. Liu and Q. Tan, *ACS Appl. Mater. Interfaces*, 2024, **16**, 12398–12406.

243 S. Yadav, V. Yadav, M. A. Siegler, P. Moënne-Loccoz, G. N. L. Jameson and D. P. Goldberg, *J. Am. Chem. Soc.*, 2024, **146**, 7915–7921.

244 E. Pastor, Z. Lian, L. Xia, D. Ecija, J. R. Galán-Mascarós, S. Barja, S. Giménez, J. Arbiol, N. López and F. P. García de Arquer, *Nat. Rev. Chem.*, 2024, **8**, 159–178.

245 D. H. Li, Y. Jia, G. J. Chang, J. Chen, H. W. Liu, J. C. Wang, Y. F. Hu, Y. Z. Xia, D. J. Yang and X. D. Yao, *Chem*, 2018, **4**, 2345–2356.

246 Z. Lian, F. Dattila and N. López, *Nat. Catal.*, 2024, **7**, 401–411.

247 X. R. Zheng, Y. H. Cao, H. Z. Wang, J. F. Zhang, M. H. Zhao, Z. Huang, Y. Wang, L. Zhang, Y. D. Deng, W. B. Hu and X. P. Han, *Angew. Chem., Int. Ed.*, 2023, **62**, e202302689.

248 L. Xia, B. F. Gomes, W. Jiang, D. Escalera-López, Y. Wang, Y. Hu, A. Y. Faid, K. Wang, T. Chen, K. Zhao, X. Zhang, Y. Zhou, R. Ram, B. Polesso, A. Guha, J. Su, C. M. S. Lobo, M. Haumann, R. Spatschek, S. Sunde, L. Gan, M. Huang, X. Zhou, C. Roth, W. Lehnert, S. Cherevko, L. Gan, F. P. García de Arquer and M. Shviro, *Nat. Mater.*, 2025, DOI: **10.1038/s41563-025-02128-7**.

This journal is © The Royal Society of Chemistry 2025

Chem. Soc. Rev., 2025, **54**, 5108–5145 | 5145